

BROCK UNIVERSITY LIBRARY



3 9157 00903112 4

**Phonon Spectra and Thermodynamic Properties of
Rare Gas Solids Based on Empirical and
Semi-empirical (ab initio) Two-body Potentials: A
Comparative Study**

by

Gary Fekete

B.Sc., Brock University, 2004

A THESIS SUBMITTED IN PARTIAL FULFILMENT OF
THE REQUIREMENTS FOR THE DEGREE OF

MASTER OF SCIENCE

in

The Faculty of Mathematics and Sciences

Department of Physics



BROCK UNIVERSITY

October 31, 2007

2007 © Gary Fekete

In presenting this thesis in partial fulfilment of the requirements for an advanced degree at the Brock University, I agree that the Library shall make it freely available for reference and study. I further agree that permission for extensive copying of this thesis for scholarly purposes may be granted by the head of my department or by his or her representatives. It is understood that copying or publication of this thesis for financial gain shall not be allowed without my written permission.

(Signature) _____

Department of Physics

Brock University
St.Catharines, Canada

Date _____

Abstract

We study the phonon dispersion, cohesive and thermal properties of rare gas solids Ne, Ar, Kr, and Xe, using a variety of potentials obtained from different approaches; such as, fitting to crystal properties, purely *ab initio* calculations for molecules and dimers or *ab initio* calculations for solid crystalline phase, a combination of *ab initio* calculations and fitting to either gas phase data or solid state properties. We explore whether potentials derived with a certain approach have any obvious benefit over the others in reproducing the solid state properties.

In particular, we study phonon dispersion, isothermal and adiabatic bulk moduli, thermal expansion, and elastic (shear) constants as a function of temperature. Anharmonic effects on thermal expansion, specific heat, and bulk moduli have been studied using λ^2 perturbation theory in the high temperature limit using the nearest-neighbor central force (nncf) model as developed by Shukla and MacDonald [4].

In our study, we find that potentials based on fitting to the crystal properties have some advantage, particularly for Kr and Xe, in terms of reproducing the thermodynamic properties over an extended range of temperatures, but agreement with the phonon frequencies with the measured values is not guaranteed. For the lighter element Ne, the LJ potential which is based on fitting to the gas phase data produces best results for the thermodynamic properties; however, the Eggenberger potential for Ne, where the potential is based on combining *ab initio* quantum chemical calculations and molecular dynamics simulations, produces results that have better agreement with the measured dispersion, and elastic (shear) values. For

Ar, the Morse-type potential, which is based on Møller-Plesset perturbation theory to fourth order (MP4) *ab initio* calculations, yields the best results for the thermodynamic properties, elastic (shear) constants, and the phonon dispersion curves.

CONTENTS

1. INTRODUCTION

2. THEORY

3. RESULTS AND DISCUSSION

4. CONCLUSIONS

5. ACKNOWLEDGMENTS

6. REFERENCES

1. J. H. Van Veen, *Phys. Rev. B*, **31**, 1155 (1985).
2. J. H. Van Veen, *Phys. Rev. B*, **32**, 1155 (1985).
3. J. H. Van Veen, *Phys. Rev. B*, **33**, 1155 (1985).
4. J. H. Van Veen, *Phys. Rev. B*, **34**, 1155 (1985).
5. J. H. Van Veen, *Phys. Rev. B*, **35**, 1155 (1985).
6. J. H. Van Veen, *Phys. Rev. B*, **36**, 1155 (1985).
7. J. H. Van Veen, *Phys. Rev. B*, **37**, 1155 (1985).
8. J. H. Van Veen, *Phys. Rev. B*, **38**, 1155 (1985).
9. J. H. Van Veen, *Phys. Rev. B*, **39**, 1155 (1985).
10. J. H. Van Veen, *Phys. Rev. B*, **40**, 1155 (1985).

7. APPENDIX A: PHONON DISPERSION

8. APPENDIX B: THERMODYNAMIC PROPERTIES

9. APPENDIX C: ELASTIC CONSTANTS

1. J. H. Van Veen, *Phys. Rev. B*, **41**, 1155 (1985).
2. J. H. Van Veen, *Phys. Rev. B*, **42**, 1155 (1985).

Contents

Abstract	ii
Contents	iv
List of Tables	vi
List of Figures	viii
Acknowledgements	xiv
1 Introduction	1
1.1 Calculation of the Potential Energy	3
1.1.1 Types of Intermolecular Forces	3
1.2 Bonding in Rare Gas Solids	6
1.3 Ne, Ar, Kr, and Xe Pair Potentials	7
1.3.1 The Ne Potentials	7
1.3.2 The Ar Potentials	10
1.3.3 The Kr Potentials	14
1.3.4 The Xe Potentials	16
2 Lattice Vibrations	18
2.0.5 Theory of Lattice Vibrations	18
2.0.6 Phonon Frequencies via the Tensor Force Model	22

2.0.7	Results for the Phonon Dispersion Curves	24
3	Thermodynamical Properties	32
3.1	Isothermal and Adiabatic Bulk Moduli, and Specific Heats	32
3.1.1	Results for the Thermal Expansion of the Isothermal and Adiabatic Bulk Moduli, and Specific Heats	34
3.2	Elastic Constants via the Long Wavelength Limit	54
3.2.1	Results for the Elastic Constants via the Long Wavelength Limit . . .	54
4	Anharmonic Corrections to the Thermal Expansion	67
4.1	Anharmonic Theory	67
4.1.1	Results for the Anharmonic Corrections to the Thermal Expansion of the Isothermal and Adiabatic Bulk Moduli, and Specific Heats	71
4.1.2	Results for the Elastic Constants via the Long Wavelength Limit with Anharmonic Corrections	82
5	Discussions and Conclusions	88
5.1	Discussions of the Phonon Dispersion Calculations	88
5.2	Discussions of the Thermodynamic Properties of Ne, Ar, Kr, and Xe	92
5.3	Elastic Constants Calculation Discussions via the Long Wavelength Limit . .	96
	Bibliography	114

List of Tables

1.1	The parameters for the Aziz potential energy function of Ne in atomic units (au) [14, 15].	9
2.1	List of neighbours for face-centred cubic crystals.	24
4.1	Coefficients of the least-squares fit for the calculations of the BZ sums used in the study of anharmonic effects [4].	71
5.1	Calculated percent errors for Ne, Ar, Kr, and Xe dispersion calculations at the zone boundaries in the [100], and [111] principal symmetry directions. . .	91
5.2	Calculated elastic constant c_{11} in the quasiharmonic (QH) approximation for Ne, and Ar. The labels are defined in the text.	98
5.3	Calculated elastic constant c_{12} in the QH approximation for Ne, and Ar. The labels are defined in the text.	99
5.4	Calculated elastic constant c_{44} in the QH approximation for Ne, and Ar. The labels are defined in the text.	100
5.5	Calculated elastic constant c_{11} in the QH approximation for Kr. The labels are defined in the text.	101
5.6	Calculated elastic constant c_{12} in the QH approximation for Kr. The labels are defined in the text.	102

5.7	Calculated elastic constant c_{44} in the QH approximation for Kr. The labels are defined in the text.	103
5.8	Calculated elastic constant c_{11} in the QH approximation for Xe. The labels are defined in the text.	104
5.9	Calculated elastic constant c_{12} in the QH approximation for Xe. The labels are defined in the text.	105
5.10	Calculated elastic constant c_{44} in the QH approximation for Xe. The labels are defined in the text.	106
5.11	Calculated elastic constant c_{11} with the λ^2 anharmonic corrections for Kr. The labels are defined in the text.	107
5.12	Calculated elastic constant c_{12} with the λ^2 anharmonic corrections for Kr. The labels are defined in the text.	108
5.13	Calculated elastic constant c_{44} with the λ^2 anharmonic corrections for Kr. The labels are defined in the text.	109
5.14	Calculated elastic constant c_{11} with the λ^2 anharmonic corrections for Xe. The labels are defined in the text.	110
5.15	Calculated elastic constant c_{12} with the λ^2 anharmonic corrections for Xe. The labels are defined in the text.	111
5.16	Calculated elastic constant c_{44} with the λ^2 anharmonic corrections for Xe. The labels are defined in the text.	112

List of Figures

1.1	Normalized plot for the comparison of the pair-potentials for Ne.	9
1.2	Normalized plot for the comparison of the pair-potentials for Ar.	13
1.3	Normalized plot for the comparison of the pair-potentials for Kr.	15
1.4	Normalized plot for the comparison of the pair-potentials for Xe.	17
2.1	Phonon-dispersion relations in [100], [110], and [111] principal symmetry directions in Ne at 10 K. •, experimental measurements from [28]. The calculations are from the quasiharmonic theory using the Eggenberger potential sixth-shell calculations.	25
2.2	Phonon-dispersion relations in [100], [110], and [111] principal symmetry directions for ^{36}Ar at 10 K. •, experimental measurements from [27]. The calculations are from the quasiharmonic theory using the Exp-6 potential sixth-shell calculations (black lines), Aziz potential sixth-shell calculations (red lines), Morse-type potential sixth-shell calculations (blues lines), LJ potential sixth-shell calculations (green lines).	26

2.3	Phonon-dispersion relations in [100], [110], and [111] principal symmetry directions for Kr at 10 K. •, experimental measurements from [29]. The calculations are from the quasiharmonic theory using the Morse potential first-shell calculations (black lines), Aziz potential sixth-shell calculations (red lines), LJ potential first-shell calculations (blues lines), Rydberg potential first-shell calculations (green lines).	27
2.4	Phonon dispersion curves for Xe using the Exp-6 potential sixth-shell calculations. The solid lines are the theoretical calculations from quasiharmonic theory. •, experimental measurements from [30].	28
2.5	Phonon dispersion curves for Xe using the Rydberg potential first-shell calculations. The solid lines are the theoretical calculations from quasiharmonic theory. •, experimental measurements from [30].	29
2.6	Phonon dispersion curves for Xe using the Morse potential first-shell calculations. The solid lines are the theoretical calculations from quasiharmonic theory. •, experimental measurements from [30].	30
2.7	Phonon dispersion curves for Xe using the LJ potential first-shell calculations. The solid lines are the theoretical calculations from quasiharmonic theory. •, experimental measurements from [30].	31
3.1	Lattice constant (a_T) at zero pressure for Ne. +, experimental points [31]; the labels for each line are defined in the text.	34
3.2	Lattice constant (a_T) at zero pressure for Ar. +, experimental points [31]; the labels for each line are defined in the text.	35
3.3	Lattice constant (a_T) at zero pressure for Kr. +, experimental points [31]; the labels for each line are defined in the text.	36

3.4	Lattice constant (a_T) at zero pressure for Xe. +, experimental points [31]; the labels for each line are defined in the text.	37
3.5	Isothermal bulk modulus (B_T) for Ne. +, experimental points [31]; the labels for each line are defined in the text.	38
3.6	Isothermal bulk modulus (B_T) for Ar. +, experimental points [31]; the labels for each line are defined in the text.	39
3.7	Isothermal bulk modulus (B_T) for Kr. +, experimental points [31]; the labels for each line are defined in the text.	40
3.8	Isothermal bulk modulus (B_T) for Xe. +, experimental points [31]; the labels for each line are defined in the text.	41
3.9	Adiabatic bulk modulus (B_s) for Ne. +, experimental points [31]; the labels for each line are defined in the text.	42
3.10	Adiabatic bulk modulus (B_s) for Ar. +, experimental points [31]; the labels for each line are defined in the text.	43
3.11	Adiabatic bulk modulus (B_s) for Kr. +, experimental points [31]; the labels for each line are defined in the text.	44
3.12	Adiabatic bulk modulus (B_s) for Xe. +, experimental points [31]; the labels for each line are defined in the text.	45
3.13	Specific heat at constant volume (C_V) for Ne. +, experimental points [31]; the labels for each line are defined in the text.	46
3.14	Specific heat at constant volume (C_V) for Ar. +, experimental points [32]; the labels for each line are defined in the text.	47
3.15	Specific heat at constant volume (C_V) for Kr. +, experimental points [33]; the labels for each line are defined in the text.	48

3.16	Specific heat at constant volume (C_V) for Xe. +, experimental points [34]. The labels for each line are not shown because of the proximity of each curve with respect to the others are very close.	49
3.17	Specific heat at constant pressure (C_P) for Ne. +, experimental points [31]; the labels for each line are defined in the text.	50
3.18	Specific heat at constant pressure (C_P) for Ar. +, experimental points [31]; the labels for each line are defined in the text.	51
3.19	Specific heat at constant pressure (C_P) for Kr. +, experimental points [31]; the labels for each line are defined in the text.	52
3.20	Specific heat at constant pressure (C_P) for Xe. +, experimental points [31]; the labels for each line are defined in the text.	53
3.21	Elastic constant c_{11} via the long wavelength limit for Ne. \square are the experi- mental points from [31]. The labels for each line are defined in the text. . . .	55
3.22	Elastic constant c_{12} via the long wavelength limit for Ne. \square are the experi- mental points from [31]. The labels for each line are defined in the text. . . .	56
3.23	Elastic constant c_{44} via the long wavelength limit for Ne. \square are the experi- mental points from [31]. The labels for each line are defined in the text. . . .	57
3.24	Elastic constant c_{11} via the long wavelength limit for Ar. \square are the experi- mental points from [31]. The labels for each line are defined in the text. . . .	58
3.25	Elastic constant c_{12} via the long wavelength limit for Ar. \square are the experi- mental points from [31]. The labels for each line are defined in the text. . . .	59
3.26	Elastic constant c_{44} via the long wavelength limit for Ar. \square are the experi- mental points from [31]. The labels for each line are defined in the text. . . .	60
3.27	Elastic constant c_{11} via the long wavelength limit for Kr. \square are the experi- mental points from [31]. The labels for each line are defined in the text. . . .	61

3.28	Elastic constant c_{12} via the long wavelength limit for Kr. \square are the experimental points from [31]. The labels for each line are defined in the text. . . .	62
3.29	Elastic constant c_{44} via the long wavelength limit for Kr. \square are the experimental points from [31]. The labels for each line are defined in the text. . . .	63
3.30	Elastic constant c_{11} via the long wavelength limit for Xe. \square are the experimental points from [31]. The labels for each line are defined in the text. . . .	64
3.31	Elastic constant c_{12} via the long wavelength limit for Xe. \square are the experimental points from [31]. The labels for each line are defined in the text. . . .	65
3.32	Elastic constant c_{44} via the long wavelength limit for Xe. \square are the experimental points from [31]. The labels for each line are defined in the text. . . .	66
4.1	Lattice constant (a_T) at zero pressure for Kr. +, experimental points [31]; the labels for each line are defined in the text.	72
4.2	Lattice constant (a_T) at zero pressure for Xe. +, experimental points [31]; the labels for each line are defined in the text.	73
4.3	Isothermal bulk modulus (B_T) for Kr. +, experimental points [31]; the labels for each line are defined in the text.	74
4.4	Isothermal bulk modulus (B_T) for Xe. +, experimental points [31]; the labels for each line are defined in the text.	75
4.5	Adiabatic bulk modulus (B_s) for Kr. +, experimental points [31]; the labels for each line are defined in the text.	76
4.6	Adiabatic bulk modulus (B_s) for Xe. +, experimental points [31]; the labels for each line are defined in the text.	77
4.7	Specific heat at constant volume (C_V) for Kr. +, experimental points [33]; the labels for each line are defined in the text.	78

4.8	Specific heat at constant volume (C_V) for Xe. +, experimental points [34]; the labels for each line are defined in the text.	79
4.9	Specific heat at constant pressure (C_P) for Kr. +, experimental points [31]; the labels for each line are defined in the text.	80
4.10	Specific heat at constant pressure (C_P) for Xe. +, experimental points [31]; the labels for each line are defined in the text.	81
4.11	Elastic constant c_{11} via the long wavelength limit for Kr. \square are the experi- mental points from [31]. The labels for each line are defined in the text. . . .	82
4.12	Elastic constant c_{12} via the long wavelength limit for Kr. \square are the experi- mental points from [31]. The labels for each line are defined in the text. . . .	83
4.13	Elastic constant c_{44} via the long wavelength limit for Kr. \square are the experi- mental points from [31]. The labels for each line are defined in the text. . . .	84
4.14	Elastic constant c_{11} via the long wavelength limit for Xe. \square are the experi- mental points from [31]. The labels for each line are defined in the text. . . .	85
4.15	Elastic constant c_{12} via the long wavelength limit for Xe. \square are the experi- mental points from [31]. The labels for each line are defined in the text. . . .	86
4.16	Elastic constant c_{44} via the long wavelength limit for Xe. \square are the experi- mental points from [31]. The labels for each line are defined in the text. . . .	87

Acknowledgements

I would like to thank my supervisor, Dr. Bose for creating this project, for his guidance, patience, and accepting me as a graduate student. I would also like to thank Dr. Shukla for his help, and expert guidance. I'd like to thank my parents (Bill and Connie) for their loving support, guidance, and encouragement. Finally, I'd like to thank the physics department for providing me with the knowledge I received at Brock University.

Chapter 1

Introduction

In this thesis we calculate the dynamical and thermodynamic properties of the rare gas solids Ne, Ar, Kr, and Xe. The potentials we consider, and how they are developed is discussed below. Due to the fact that the electronic shells are filled, the charge density of all inert gas atoms is spherically symmetric and these have been calculated accurately using the tools of quantum chemistry. There has been a large body of work in calculating the potential between inert gas atoms as well. These potentials can form the basic ingredient in calculating the total energy of the rare gas solids, provided one includes the contribution from three-body and possibly other many-body interactions. A large number of studies have been devoted to the study of the cohesive, thermal, and dynamical properties of rare gas solids using this approach [1]. In many cases, studies have been based on two-body potentials alone. In principle, if a two-body potential is constructed via calculations performed for the solid phase, or by fitting to the properties of the crystal, then the effects of three and higher-body interactions can be assumed to have been included implicitly to some extent. For rare gas solids it is easier to construct such two-body potentials. Unlike covalent solids with highly directional charge distribution and bonding, where the potentials often need to include angle-dependent terms or metallic systems, where the total energy is volume-dependent because of the volume-dependent kinetic, exchange and correlation energy of the conduction electrons; central two-body and volume-independent potentials have been found to satisfactorily describe the properties of rare gas solids.

In this work we study the phonon dispersion, cohesive and thermal properties of rare

gas solids using a variety of potentials, obtained from different approaches. Some of these potentials are fully or partially based on *ab initio* calculations and others are derived by fitting to the crystal properties. Among those which are based on *ab initio* calculations, some are derived from the *ab initio* total energy calculations for the solid phase, and some are based on calculations for dimers and molecules. Our goal is to explore whether potentials derived with a certain approach have any obvious benefit over the others in reproducing the solid state properties. In particular, we would like to see whether potentials obtained by fitting to the crystal properties fare better than those based on full or partial *ab initio* calculations. It is not possible to know *a priori* whether such potentials have an obvious advantage. Most often the parameters of a two-body potential are obtained by fitting to crystal properties such as the equilibrium lattice parameter, cohesive energy, and elastic constants. If one fits the elastic constants c_{11} , c_{12} and c_{44} , then the slopes of the phonon dispersion curves at the zone center should come out correctly. However, this does not insure that the phonon frequencies at high wave vectors, i.e. near the zone boundary will be reproduced well and agree with the measured values. If instead of the elastic constants, one simply fits the bulk modulus $B = (c_{11} + 2c_{12})/3$, then even the slopes of the phonon dispersion curves at zero wave vector (long waves) are not guaranteed to have the correct values. However, the frequencies at various other (off-symmetry) points of the Brillouin zone may be reproduced satisfactorily. For reproducing the thermal properties of the solid over a wide range of temperature and lattice parameter, it may be advisable to choose a potential that can reproduce the total energy versus volume relation of a solid (or the equation-of-state) over an extended range of volume.

Most of the *ab initio* or semi *ab initio* (semi-empirical) two-body potentials used in this work have not been used in previous studies of the thermodynamic properties of rare gas solids. For the sake of comparison we have included two-body potentials, obtained by fitting to crystal properties, which have been used previously in such studies [2, 3]. Such potentials

usually have the familiar Lennard-Jones, Rydberg or Morse form.

We have studied the anharmonic effects on thermal expansion and thermodynamic properties by following the work of Shukla and MacDonald [4]. The details are given in chapter 4.

1.1 Calculation of the Potential Energy

The calculation of the potential energy arising from intermolecular interaction is the most arduous and essential step in any molecular simulation [5]. Generally, the potential energy (E_{pot}) of N interacting particles can be evaluated as

$$E_{pot} = \sum_i \phi_i(r_i) + \sum_i \sum_{j>i} \phi_2(r_i, r_j) + \sum_i \sum_{j>i} \sum_{k>j>i} \phi_3(r_i, r_j, r_k) + \dots, \quad (1.1)$$

The first term represents the effect of an external field and the other terms represent particle interactions, that is, ϕ_2 is the potential between pairs of particles and ϕ_3 is the potential between particle triplets, et cetera. As discussed below, the interaction between particles is commonly evaluated from a suitable potential function.

Typically, it is assumed that only two-body interactions are important and equation 1.1 is truncated after the second term. Two-body interactions definitely make the most contribution to particle interactions; however, there is evidence that three-body interactions may be important in some cases [6, 7, 8].

1.1.1 Types of Intermolecular Forces

Intermolecular interaction is a result of both long-range and short-range effects. Short-range interactions are represented by an exponential decay in the interaction energy with respect to intermolecular separation. At small intermolecular separations, there is a considerable overlap of the molecular wave functions causing either intermolecular exchange or repulsion.

The long-range attractive part of the interaction is usually proportional to the inverse powers of the intermolecular distance. The two contributions, short-range (SR) and long-range (LR), can be evaluated separately and the total potential energy is obtained by combining the two parts:

$$\Delta E_{ab} = \Delta E_{ab}^{SR} + \Delta E_{ab}^{LR}. \quad (1.2)$$

A second approach to obtain the intermolecular potential is to treat the interacting molecules a and b as a single large molecule. The potential is obtained by calculating the energy of ab and subtracting the energies of the separated a and b molecules:

$$\Delta E_{ab} = E_{ab} - E_a - E_b. \quad (1.3)$$

These methods can be applied using quantum mechanics and by associating the molecules a and b with unperturbed wave functions ψ_a and ψ_b . The interaction Hamiltonian V_{ab} resulting from Coulombic interaction between the electrons and nuclei of a and the electrons and nuclei of b can be introduced as a perturbation. If the wave functions do not overlap, the interaction energy from first order perturbation [5] is

$$\Delta_1 E_{ab}^{LR} = \langle \Psi_a \Psi_b | V_{ab} | \Psi_a \Psi_b \rangle. \quad (1.4)$$

This is the rigid electronic interaction potential resulting from the Coulombic interaction of unperturbed electronic distributions of the isolated molecules a and b . Second order perturbation of the interaction Hamiltonian V_{ab} is required because the first order treatment fails to describe the long-range interaction between spherical systems. In order to account for dispersion interaction, the second order perturbation of the interaction Hamiltonian V_{ab} is

$$\Delta_2 E_{ab}^{LR} = - \sum_{i \neq 0} \sum_{j \neq 0} \frac{|\langle \Psi_a \Psi_b | V_{ab} | \Psi_a^i \Psi_b^j \rangle|^2}{E_a^i - E_a + E_b^j - E_b}, \quad (1.5)$$

where the superscripts represent the i -th excited state. It can be shown from equation 1.5 that the dispersion for spherical atoms is

$$\Delta E_{ab}^{disp} = \frac{C_6}{r^6} + \frac{C_8}{r^8} + \frac{C_{10}}{r^{10}} + \dots, \quad (1.6)$$

where the coefficients $C_6, C_8, C_{10} \dots$ are the dispersion coefficients that depend on the relative orientations, and r represents the distance between the nuclei of atoms a and b . Third order perturbation is required to determine the three-body interactions and in 1943 Axilrod and Teller formulated an explicit expression for the triple-dipole potential [9] and has the form

$$\phi_3(ijk) = \frac{\nu(1 + 3 \cos \theta_i \cos \theta_j \cos \theta_k)}{(r_{ij}r_{ik}r_{jk})^3}, \quad (1.7)$$

where θ represents the inside angles of the triangle, r_{ij}, r_{ik}, r_{jk} are the intermolecular separations, and ν is the non-additive coefficient. A large number of two-body potentials have been developed and historically, an empirical approach was used with the parameters of the potential being obtained from experimental data such as second virial coefficients, viscosities, molecular beam cross sections, et cetera. For example, to obtain the second virial coefficient, the Lennard-Jones potential can be used as an approximation to the true potential. The parameters σ and ϵ can then be measured experimentally in the gas phase, and thus use the results to make predictions about the solid phase [10]. The gas-phase measurements use the following relation from the virial expansion:

$$b_2 = \frac{1}{2} \int d\vec{r} [1 - e^{-\beta\phi(r)}], \quad (1.8)$$

where $\beta = 1/k_B T$, and $\phi(r)$ is the potential energy function. The coefficient b_2 enters the virial expansion for the pressure P in the form

$$\frac{PV}{k_B T} = 1 - \frac{b_2}{V} \dots \quad (1.9)$$

so measurements of the equation of state at low densities can be used to find b_2 , and hence fit to the parameters in $\phi(r)$.

1.2 Bonding in Rare Gas Solids

The inert gases form the simplest crystals, and as mentioned previously, due to the fact that the electronic shells are filled, the charge density of all inert gas atoms are spherically symmetric. In the crystal the inert gas atoms pack together as closely as possible and the crystal structures are all cubic close-packed fcc, except for He^3 and He^4 [11]. Bonding in rare gas solids arise when quantum or thermal fluctuations continually induce tiny dipole moments on each atom. The resulting electric field then polarizes the other atom producing a small dipole moment in it of order r^{-3} and the resulting interaction is then of order r^{-6} [10]. This is referred to as the Van der Waals-London Interaction. The Hamiltonian for the two-atom system is

$$H = H_1 + H_2 + V_{ab}, \quad (1.10)$$

where H_1 is the Hamiltonian for atom 1, H_2 is the Hamiltonian for atom 2 [12]. V is the quantum operator for Coulomb interaction between all pairs of charged particles, one from atom 1, and one from atom 2 and has the form

$$V_{ab} = e^2 \left[\frac{Z^2}{r} - \sum_{i=1}^Z \left(\frac{Z}{|\mathbf{r} - \mathbf{r}_i^{(1)}|} + \frac{Z}{r_i^{(2)}} \right) + \sum_{i,j=1}^Z \frac{1}{|\mathbf{r}_i^{(1)} - \mathbf{r}_j^{(2)}|} \right], \quad (1.11)$$

where Z is the number of bound electrons surrounding each nuclei. The electrons bound to the nucleus at origin $\mathbf{0}$ have coordinates denoted by $\mathbf{r}_i^{(1)}$ and the electrons bound to the nucleus at \mathbf{r} have coordinates $\mathbf{r}_i^{(2)}$, where $i = 1, \dots, Z$. Using second order perturbation theory, the interaction energy between the two atoms is given by

$$\Delta E = \langle 0 | V_{ab} | 0 \rangle + \sum_n \frac{|\langle 0 | V_{ab} | n \rangle|^2}{E_0 - E_n}, \quad (1.12)$$

where $|0\rangle$ is the ground state of the unperturbed two-atom system, and $|n\rangle$ is the excited states. It can be shown that the leading term in equation 1.12 varies as $1/r^6$ and is negative for large r . This is the Van der Waals-London Interaction.

1.3 Ne, Ar, Kr, and Xe Pair Potentials

1.3.1 The Ne Potentials

The Lennard-Jones Potential

We start with the most familiar potential; the (6-12) Lennard-Jones potential. It is usual to write the potential of the two atoms at separation distance r as

$$\phi_{LJ}(r) = 4\epsilon \left[\left(\frac{\sigma}{r} \right)^{12} - \left(\frac{\sigma}{r} \right)^6 \right], \quad (1.13)$$

where σ is the length parameter and ϵ is the potential well depth. We chose the values of $\sigma = 2.74 \text{ \AA}$ and $\epsilon = 50 \times 10^{-16} \text{ erg}$ from [11]. These parameters were obtained from fitting to the gas phase data. The attractive interaction in equation 1.13 varies as the minus sixth power. This is called the Van der Waals interaction, as discussed above, and is also known as the London interaction or the induced dipole-dipole interaction. It is the principal attractive interaction in crystals of inert gases and also in crystals of many organic molecules.

The Eggenberger *et. al.* Potential

The Eggenberger potential from [13] has the following analytical form

$$\begin{aligned} \frac{\phi_E(r)}{E_h} = & a_1 \exp(-a_2(r/a_0)^2) + a_3 \exp(-a_4(r/a_0)^2) \\ & + a_5 \exp(-a_6(r/a_0)^2) + a_7(r/a_0)^{-10} + a_8(r/a_0)^{-8} + a_9(r/a_0)^{-6}. \end{aligned} \quad (1.14)$$

$$a_1 = 1.174594, \quad a_2 = 0.355905, \quad a_3 = 1.325805 \times 10^{-1},$$

$$a_4 = 0.214065, \quad a_5 = 976.69318 \times 10^{-6}, \quad a_6 = 0.105389,$$

$$a_7 = 5.412694 \times 10^3, \quad a_8 = -3.512808 \times 10^2, \quad a_9 = -3.964331.$$

This potential is obtained by combining *ab initio* quantum chemical calculations, commonly used to obtain properties of single molecules, with molecular dynamics simulations. The

ab initio calculations of the potential incorporate electron-correlation by means of Møller-Plesset perturbation theory to fourth order with single, double, triple and quadruple excitations (MP4(SDTQ)). Using this technique, properties of the condensed phase can be calculated without using any empirical data. This technique is referred to as *global simulations*. No physical significance should be attached to the parameters above with the exception of a_0 (the Bohr radius).

The Aziz *et. al.* Potential

The Aziz potential from [14, 15] has the following analytical form

$$\begin{aligned}
 \phi_A(r) &= Ar^\gamma e^{-\alpha r} - f(r) \left(\frac{C_6}{r^6} + \frac{C_8}{r^8} + \frac{C_{10}}{r^{10}} \right), \\
 f(r) &= e^{-0.4} F(r) \text{ for } r < 1.28r_m, \\
 &= 1 \text{ for } r \geq 1.28r_m, \\
 F(r) &= e^{-(1.28r_m/r-1)^2} \text{ for } r < 1.28r_m, \\
 &= 1 \text{ for } r \geq 1.28r_m.
 \end{aligned} \tag{1.15}$$

The parameters of the potential energy function were determined by fitting the function to the second virial coefficient data of the system considered. It is applied to the transport properties of dilute Ne gas, Ne-Ne scattering cross-sections, and to calculate the spectroscopic constants of the dimer. Three sets of parameters were obtained and are given in table 1.1. C_6 , C_8 , and C_{10} are the dispersion coefficients, r is the interatomic separation, and r_m is the value of r corresponding to the van der Waals minimum in the potential. The parameters A , γ , and α are adjusted to fit the experimentally determined properties of the system considered. Figure 1.1 depict the plots of the potential energy functions with reduced parameters for comparison.

Table 1.1: The parameters for the Aziz potential energy function of Ne in atomic units (au) [14, 15].

Parameter	set - 1	set - 2	set - 3
A	156.0805	116.9961	156.5
γ	1.5	0.5	0.0
α	2.950273	2.550646	2.456
C_6	6.573	6.885307	6.35
C_8	56.0	71.76737	76.0
C_{10}	760.0	1002.447	1100.0
R_m	5.782563	5.833586	5.820358

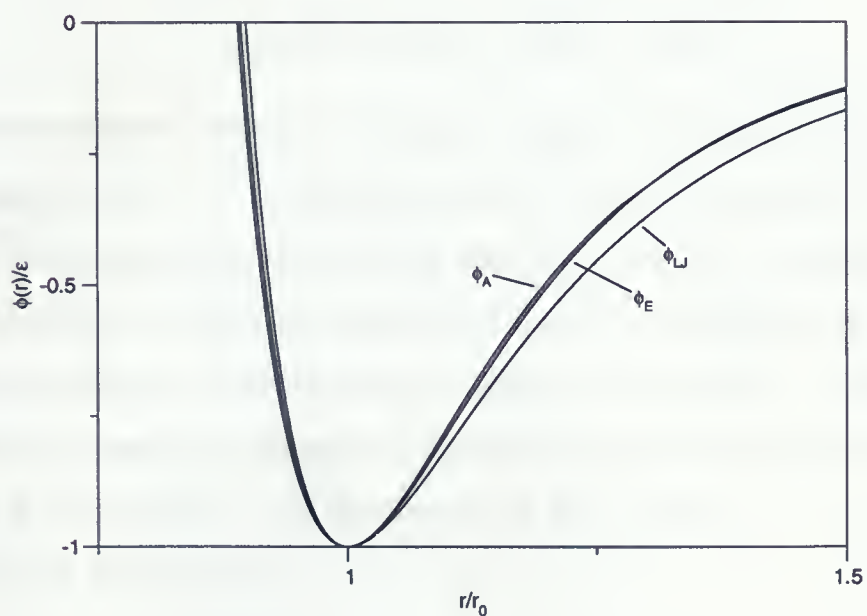


Figure 1.1: Normalized plot for the comparison of the pair-potentials for Ne.

1.3.2 The Ar Potentials

The Aziz *et. al.* Potential

The Aziz potential used in the calculation HFD-C (Hartree-Fock Dispersion version C) from [16] is expressed in a slightly different form than the Aziz potential for Ne. The potential has the following analytical form

$$\begin{aligned}
 \phi_A(r) &= \epsilon \phi^*(x), \\
 \phi_A^*(r) &= Ax^\gamma e^{-\alpha x} - \left(\frac{c_6}{x^6} + \frac{c_8}{x^8} + \frac{c_{10}}{x^{10}} \right) F(x), \\
 F(x) &= e^{-(D/x-1)^2} \text{ for } x < D, \\
 &= 1 \text{ for } x \geq D,
 \end{aligned} \tag{1.16}$$

where $D = 1.28$ and $x = r/r_m$. The parameters used in the calculations from [16] are

$$\begin{aligned}
 A &= 0.9502720(7), \quad \alpha = 16.345655, \quad c_6 = 1.0914254, \\
 c_8 &= 0.6002595, \quad c_{10} = 0.3700113, \quad \gamma = 2.0, \\
 \epsilon/k_B(K) &= 143.224, \quad r_m(\text{\AA}) = 3.759.
 \end{aligned}$$

The parameters defined above share the same meanings as those for the Ne Aziz potential with the exception of ϵ (the potential well depth at the minimum) and k_B (the Boltzman constant). This potential was developed by using a combination of an *ab initio* calculation of the self-consistent field (SCF) Hartree-Fock repulsion between closed shell systems, a semi-empirical estimate of the correlation energy, and empirically determined dispersion coefficients c_6 , c_8 , and c_{10} obtained from gas-phase data which determined the long range attraction of the potential. The contribution of the dispersion term in the potential is regulated by the damping term

$$\begin{aligned}
 F(x) &= e^{-(D/x-1)^2} \text{ for } x < D, \\
 &= 1 \text{ for } x \geq D,
 \end{aligned}$$

and is considered to be universal for all spherical systems [16].

The Morse-Type Potential

Woon [17] used Møller-Plesset perturbation theory to fourth order (MP4) *ab initio* calculation to determine the intermolecular forces between two argon atoms. The results of the *ab initio* calculations were then fitted to the Morse-type potential

$$\begin{aligned} \phi_M(r) = & \epsilon \left[Q \exp \left(- \sqrt{\frac{(Q+1)k_e}{Q\epsilon}} (r - r_e) \right) \right. \\ & \left. - (Q+1) \exp \left(- \sqrt{\frac{Qk_e}{(Q+1)\epsilon}} (r - r_e) \right) \right]. \end{aligned} \quad (1.17)$$

The parameters in equation 1.17 have the usual meanings: ϵ is the well depth, r_e is the equilibrium separation and k_e is the force constant (i.e. $d^2\phi_M(r)/dr^2$ evaluated at r_e); Q is the weighting factor often set to 1 but has been optimized by Woon [17]. The parameters used in the calculations are $\epsilon(mE_h) = 0.4700$, $r_e(a_0) = 7.1324$, $k_e(mE_h/a_0^2) = 0.7359$, and $Q = 0.6804$.

The Exponential-Six Potential

The exponential-six potential has the following form

$$\phi_{Exp-6}(r) = \epsilon \left[\frac{6}{\alpha - 6} \exp(\alpha(1 - r/r_m)) - \frac{\alpha}{\alpha - 6} \left(\frac{r_m}{r} \right)^6 \right], \quad (1.18)$$

where $\alpha = 13.0$, $\epsilon/k_B = 122K$, and $r_m = 3.85\text{\AA}$ [18]. These parameters have the usual meanings with the exception of α (the steepness of the potential energy function).

High-density fluid-perturbation theory was employed using the inverse twelfth-power potential as the reference system instead of the hard-sphere approximation to compute the properties of a fluid of particles interacting by means of the exponential-six potential [18, 19].

The Exponential-Six-Eight Potential

The exponential-six-eight potential has the following form

$$\phi_{Exp-6-8}(r) = e \exp(a(r - b)) + cr^{-6} + dr^{-8}, \quad (1.19)$$

where $a(\text{\AA}^{-1}) = -3.832$, $b(\text{\AA}) = 4.994$, $c(K\text{\AA}^6) = -5.84 \times 10^5$, $d(K\text{\AA}^8) = -1.28 \times 10^6$, and $e(K) = 1.0483$. The calculation employed the self-consistent augmented-plane-wave statistical exchange (APW-X α) method [20]. The empirical parameters for this potential were obtained by least-squares fit of lattice sums of the Born-Oppenheimer approximation

$$E(V) = \frac{1}{2N} \sum_{i=2}^N \phi_{1,i}, \quad (1.20)$$

for all V , and varying the parameters in $\phi_{i,j}$ to the lattice sums of the Barker-Bobetic pair potential, including the triple dipole interactions [20].

The Lennard-Jones Potential

The parameters in the Lennard-Jones potential (defined above) used in the calculations for Ar are $\sigma(\text{\AA}) = 3.400$, and $\epsilon(K) = 119.4$ and have the usual meanings [20]. The calculated parameters were determined by varying them in $\phi_{1,i}$ until the nonlinear-least-squares fit is closest to the APW-X α static lattice energies $E(V)$ [20]. Figure 1.2 depict the plots of the potential energy functions with reduced parameters for comparison.

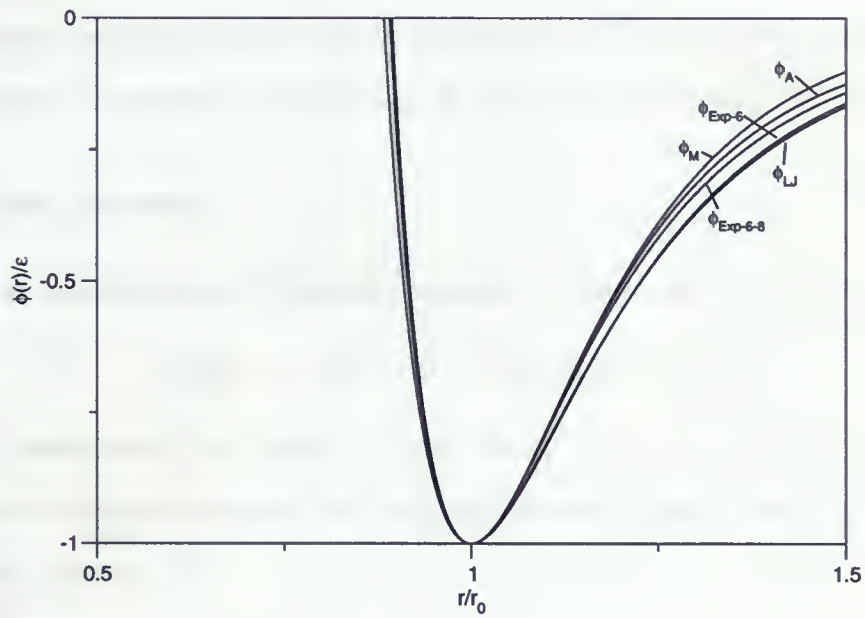


Figure 1.2: Normalized plot for the comparison of the pair-potentials for Ar.

1.3.3 The Kr Potentials

The Morse Potential

The Morse potential used in the calculations for Kr has the following form

$$\phi_M(r) = \epsilon(\exp(-2\alpha(r - r_0)) - 2\exp(-\alpha(r - r_0))). \quad (1.21)$$

The three parameters $\epsilon(10^{-14}erg) = 3.254$, $r_0(\text{\AA}) = 3.969$, and $\alpha(\text{\AA}^{-1}) = 1.556$ in the potential function have the usual meanings and are determined by fitting to the crystal properties; namely, the sublimation energy (including the harmonic zero-point energy), the equilibrium lattice constant, and the isothermal bulk modulus all at $T = 0K$ via the experimental values. The parameter α represents the steepness of the potential function [2].

The Rydberg Potential

The Rydberg potential used in the calculations for Kr has the following form

$$\phi_R(r) = -\epsilon[1 + \alpha(r - r_0)] \exp(-\alpha(r - r_0)). \quad (1.22)$$

The three parameters $\epsilon(10^{-14}erg) = 3.254$, $r_0(\text{\AA}) = 3.971$, and $\alpha(\text{\AA}^{-1}) = 2.194$ in the potential function are determined by fitting to the crystal properties using the same method as the Morse potential [2].

The Lennard-Jones Potential

The Lennard-Jones potential used in the calculations for Kr is written in a slightly different form than previously used:

$$\phi_{LJ}(r) = \epsilon \left[\left(\frac{r_0}{r} \right)^{12} - 2 \left(\frac{r_0}{r} \right)^6 \right]. \quad (1.23)$$

The two parameters are $\epsilon(10^{-14}erg) = 3.248$, and $r_0(\text{\AA}) = 3.965$ and have the usual meanings. Again, these parameters were determined by fitting to the crystal properties using the same method as the Morse, and Rydberg potentials [2].

The Aziz HFGKR Potential

The potential HFGKR by Aziz [21] used in the calculations for Kr has the same form as the Ar potential. Again, the parameters have the usual meanings and are given below.

$$A = 0.1215312(8), \quad \alpha = 16.496763, \quad c_6 = 1.1561739,$$

$$c_8 = 0.5414923, \quad c_{10} = 0.2839735, \quad \gamma = 2.4,$$

$$\epsilon/k_B(K) = 199.9, \quad r_m(\text{\AA}) = 4.012.$$

This potential was developed by using the same method for the Ar potential. Figure 1.3 depict the plots of the potential energy functions with reduced parameters for comparison.

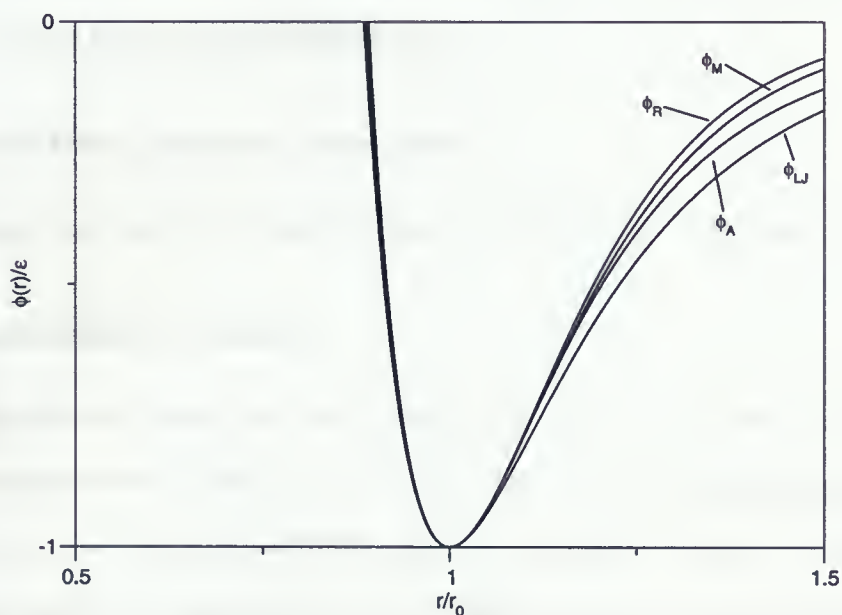


Figure 1.3: Normalized plot for the comparison of the pair-potentials for Kr.

1.3.4 The Xe Potentials

Again, the Morse, Rydberg, and Lennard-Jones potentials all share the same form as those for Kr. Furthermore, the parameters in the potential energy functions were all obtained by using the same methods above.

The Morse Potential Parameters

The three parameters used in the calculations are $\epsilon(10^{-14}erg) = 4.576$, $r_0(\text{\AA}) = 4.321$, and $\alpha(\text{\AA}^{-1}) = 1.375$ [2].

The Rydberg Potential Parameters

The three parameters used in the calculations are $\epsilon(10^{-14}erg) = 4.576$, $r_0(\text{\AA}) = 4.322$, and $\alpha(\text{\AA}^{-1}) = 1.941$ in the potential function [2].

The Lennard-Jones Potential Parameters

The two parameters used in the calculations are $\epsilon(10^{-14}erg) = 4.577$, and $r_0(\text{\AA}) = 4.318$ [2].

The Exponential-Six Potential

The Exponential-Six interatomic pair potential for Xe has the same form as Ar and the potential parameters were obtained the same way. The potential parameters used in the calculations are $\alpha = 13.0$, $\epsilon/k_B = 235K$, and $r_m = 4.47\text{\AA}$ [22]. Figure 1.4 depict the plots of the potential energy functions for Xe with reduced parameters for comparison.

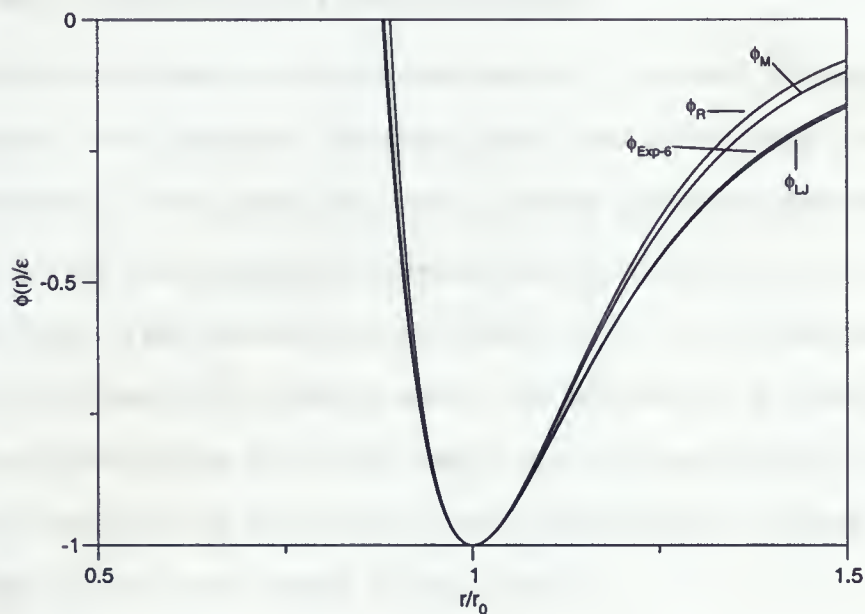


Figure 1.4: Normalized plot for the comparison of the pair-potentials for Xe.

Chapter 2

Lattice Vibrations

2.0.5 Theory of Lattice Vibrations

Atomic Force Constants and Their Properties

It is particularly convenient to begin a discussion of the elements of lattice dynamics with the assumption of an indefinitely extended crystal since the resulting perfect lattice periodicity introduced by the absence of bounding surfaces greatly simplifies the formulation of the theory [23, 24]. This assumption, however, leads to infinite values for extensive properties of the crystal. Their normalization to a finite volume by a suitable choice of boundary conditions is discussed in the following section. We are then led to consider a crystal composed of an infinite number of unit cells, each of which is a parallelepiped bounded by three non-coplanar vectors \mathbf{a}_1 , \mathbf{a}_2 , \mathbf{a}_3 . Firstly, we denote the equilibrium position vector of the l th unit cell relative to an origin located at some atom by

$$\mathbf{r}(l) = l_1\mathbf{a}_1 + l_2\mathbf{a}_2 + l_3\mathbf{a}_3, \quad (2.1)$$

where l_1 , l_2 , and l_3 are any three integers, positive, negative or zero, which we will refer to collectively as l . The vectors \mathbf{a}_1 , \mathbf{a}_2 , and \mathbf{a}_3 are called the primitive translation vectors of the lattice. If there is only one atom per unit cell, we can take equation 2.1 to define the atomic positions. These crystals are called *Bravais* or *primitive* crystals. If there are s atoms in the unit cell (where $s > 1$) the locations of the s atoms within the unit cell are given by the vectors $\mathbf{r}(\kappa)$, where κ distinguishes the different atoms in the unit cell and takes the values

$1, 2, \dots, s$. So in general, the position vector of the κ th atom in the l th unit cell is given by

$$\mathbf{r}(l\kappa) = \mathbf{r}(l) + \mathbf{r}(\kappa). \quad (2.2)$$

Crystals that contain more than one atom per unit cell are referred to as *nonprimitive* crystals. As a result of thermal fluctuations, each atom is displaced from its equilibrium position by an amount $\mathbf{u}(l\kappa)$. So the total kinetic energy of the lattice becomes

$$T = \frac{1}{2} \sum_{l,\kappa,\alpha} M_\kappa \dot{u}_\alpha^2(l\kappa) \quad (2.3)$$

where M_κ is the mass of the κ th atom, and $u_\alpha(l\kappa)$ is the α -Cartesian component of $\mathbf{u}(l\kappa)$, where $\alpha = x, y, z$. The total potential energy Φ of the crystal is assumed to be some function of the instantaneous positions of all atoms. Φ can then be expanded in a Taylor's series in powers of the atomic displacements $\mathbf{u}(l\kappa)$, and formally, we obtain that

$$\Phi = \Phi_0 + \sum_{l,\kappa,\alpha} \Phi_\alpha(l\kappa) u_\alpha(l\kappa) + \frac{1}{2} \sum_{\substack{l,\kappa,\alpha \\ l',\kappa',\beta}} \Phi_{\alpha\beta}(l\kappa; l'\kappa') u_\alpha(l\kappa) u_\beta(l'\kappa') + \dots \quad (2.4)$$

In the harmonic approximation, we neglect all higher order terms. In equation 2.4, Φ_0 is referred to as the static or equilibrium potential energy of the crystal, while clearly

$$\Phi_\alpha(l\kappa) = \left. \frac{\partial \Phi}{\partial u_\alpha(l\kappa)} \right|_0, \quad (2.5)$$

and

$$\Phi_{\alpha\beta}(l\kappa; l'\kappa') = \left. \frac{\partial^2 \Phi}{\partial u_\alpha(l\kappa) \partial u_\beta(l'\kappa')} \right|_0, \quad (2.6)$$

where the subscript zero means that the derivatives are evaluated in the equilibrium configuration. From its definition in equation 2.5, we see that the physical interpretation of the coefficient $\Phi_\alpha(l\kappa)$ is that it is the negative of the force acting in the α direction on the atom at $\mathbf{r}(l\kappa)$ in the equilibrium configuration. However, in the equilibrium configuration, the force on any particle must vanish, and so we have the result that in an equilibrium configuration

$$\Phi(l\kappa) = 0. \quad (2.7)$$

The Hamiltonian, $H = T + \Phi$, for the crystal in the harmonic approximation becomes

$$H = \Phi_0 + \frac{1}{2} \sum_{l\kappa\alpha} M_\kappa \dot{u}_\alpha^2(l\kappa) + \frac{1}{2} \sum_{\substack{l\kappa\alpha \\ l'\kappa'\beta}} \Phi_{\alpha\beta}(l\kappa; l'\kappa') u_\alpha(l\kappa) u_\beta(l'\kappa'), \quad (2.8)$$

and the equations of motion of the lattice follow immediately:

$$M_\kappa \ddot{u}_\alpha(l\kappa) = - \frac{\partial \Phi}{\partial u_\alpha(l\kappa)} = - \sum_{l'\kappa'\beta} \Phi_{\alpha\beta}(l\kappa; l'\kappa') u_\beta(l'\kappa'). \quad (2.9)$$

The coefficients $\Phi(l\kappa; l'\kappa')$, which are the second derivatives of the potential energy with respect to atomic displacements in the equilibrium configuration, are called *atomic force constants*.

$$\Phi_{\alpha\beta}(l\kappa; l'\kappa') = \Phi_{\beta\alpha}(l'\kappa'; l\kappa), \quad (2.10)$$

$$\Phi = \Phi_0 + \sum_{l\kappa\alpha} \Phi_\alpha(l\kappa) v_\alpha + \frac{1}{2} \sum_{\substack{l\kappa\alpha \\ l'\kappa'\beta}} \Phi_{\alpha\beta}(l\kappa; l'\kappa') v_\alpha v_\beta + \dots \quad (2.11)$$

$$\sum_{l\kappa} \Phi_\alpha(l\kappa) = 0 \quad (2.12)$$

$$\sum_{\substack{l\kappa \\ l'\kappa'}} \Phi_{\alpha\beta}(l\kappa; l'\kappa') = 0. \quad (2.13)$$

$$-F_\alpha(l\kappa) = \frac{\partial \Phi}{\partial u_\alpha(l\kappa)} = \Phi_\alpha(l\kappa) + \sum_{l'\kappa'\beta} \Phi_{\alpha\beta}(l\kappa; l'\kappa') u_\beta(l'\kappa') + \dots \quad (2.14)$$

$$\sum_{l'\kappa'} \Phi_{\alpha\beta}(l\kappa; l'\kappa') = 0. \quad (2.15)$$

The Dynamical Matrix

The equations of motion from equation 2.9 form an infinite set of simultaneous linear differential equations. Their solution is simplified by the periodicity of the lattice and via the restrictions on the force constants due to the periodic nature of the lattice. We can then choose as a solution to equation 2.9 a function of the form

$$u_\alpha(l\kappa) = (M_\kappa)^{-1/2} u_\alpha(\kappa) \exp[-i\omega t + i\mathbf{k} \cdot \mathbf{r}(l)]. \quad (2.16)$$

If we substitute equation 2.16 into equation 2.9 we find that

$$\omega^2 u_\alpha = \sum_{\kappa' \beta'} D_{\alpha\beta}(\kappa \kappa' | \mathbf{k}) u_\beta(\kappa'), \quad (2.17)$$

where the elements of the matrix $\mathbf{D}(\mathbf{k})$, called the Fourier transformed dynamical matrix, and are given by

$$D_{\alpha\beta}(\kappa \kappa' | \mathbf{k}) = (M_\kappa M_{\kappa'})^{-1/2} \sum_{l'} \Phi_{\alpha\beta}(l\kappa; l'\kappa') \exp[-i\mathbf{k} \cdot (\mathbf{r}(l) - \mathbf{r}(l'))]. \quad (2.18)$$

It can be shown that the potential derivatives are related to the atomic force constants via the following relations for central forces

$$\Phi_\alpha(l\kappa; l'\kappa') = \sum_{l''\kappa''} \phi_\alpha(l\kappa; l'\kappa') \quad (2.19)$$

$$\Phi_{\alpha\beta}(l\kappa; l'\kappa') = -\phi_{\alpha\beta}(l\kappa; l'\kappa'), \quad (l\kappa) \neq (l'\kappa') \quad (2.20)$$

$$\Phi_{\alpha\beta}(l\kappa; l\kappa) = \sum_{l'\kappa'} \phi_{\alpha\beta}(l\kappa; l'\kappa'), \quad (2.21)$$

where

$$\begin{aligned} \phi_\alpha(l\kappa; l'\kappa') &= \left. \frac{\partial}{\partial r_\alpha} \phi_{\kappa\kappa'}(r) \right|_{\mathbf{r}=\mathbf{r}(l\kappa; l'\kappa')} \\ &= \left. \frac{r_\alpha}{r} \phi'_{\kappa\kappa'}(r) \right|_{\mathbf{r}=\mathbf{r}(l\kappa; l'\kappa')}, \end{aligned} \quad (2.22)$$

and

$$\begin{aligned} \phi_{\alpha\beta}(l\kappa; l'\kappa') &= \left. \frac{\partial^2}{\partial r_\alpha \partial r_\beta} \phi_{\kappa\kappa'}(r) \right|_{\mathbf{r}=\mathbf{r}(l\kappa; l'\kappa')} \\ &= \left[\frac{r_\alpha r_\beta}{r^2} \left(\phi''_{\kappa\kappa'}(r) - \frac{1}{r} \phi'_{\kappa\kappa'}(r) \right) + \frac{\delta_{\alpha\beta}}{r} \phi'_{\kappa\kappa'}(r) \right] \Big|_{\mathbf{r}=\mathbf{r}(l\kappa; l'\kappa')}. \end{aligned} \quad (2.23)$$

The condition that the set of equations 2.17 have a nontrivial solution is that the determinant of the coefficients vanish

$$|D_{\alpha\beta}(\kappa \kappa' | \mathbf{k}) - \omega^2 \delta_{\alpha\beta} \delta_{\kappa\kappa'}| = 0. \quad (2.24)$$

Equation 2.24 is an equation of 3rd degree in ω^2 , and the 3 solutions for each value of \mathbf{k} will be denoted by $\omega_s(\mathbf{k})$ where $s = 1, 2, 3$. The dynamical matrix of the crystal, without proof, has the following properties

$$D_{\beta\alpha}(\kappa'\kappa|\mathbf{k}) = D_{\alpha\beta}^*(\kappa\kappa'|\mathbf{k}) \quad (2.25)$$

$$D_{\alpha\beta}(\kappa\kappa'|-\mathbf{k}) = D_{\alpha\beta}^*(\kappa\kappa'|\mathbf{k}) \quad (2.26)$$

and is Hermitian. Since it is Hermitian the $\{\omega_s^2(\mathbf{k})\}$ are real, so that $\omega_s(\mathbf{k})$ is either real or purely imaginary. A purely imaginary value for $\omega_s(\mathbf{k})$ means that the motion of the lattice would explode exponentially and this means that the lattice becomes unstable. Thus, each $\omega_s^2(\mathbf{k})$ must be positive.

2.0.6 Phonon Frequencies via the Tensor Force Model

The derivation of the diagonal and off diagonal elements of the secular equation

$$|D(\mathbf{k}) - \omega^2 I| = 0, \quad (2.27)$$

where I is the 3×3 identity matrix, \mathbf{k} is the propagation vector, and ω is the angular frequency is given below [25, 26]. In our case we consider a cubic crystal (fcc) with a lattice constant of $2a$, consisting of identical atoms each having mass M and one atom per unit cell. We consider the s th shell having n^s lattice points. Each lattice point has the coordinates h_1a, h_2a, h_3a , where h_1, h_2 and h_3 are nonnegative integers with $h_1 \geq h_2 \geq h_3$. The 3×3 force matrix ϕ_{ij}^s is symmetric and the elements are denoted by

$$\phi_{ij}^s = \begin{pmatrix} \alpha_1^s & \beta_3^s & \beta_2^s \\ \beta_3^s & \alpha_2^s & \beta_1^s \\ \beta_2^s & \beta_1^s & \alpha_3^s \end{pmatrix} \quad (2.28)$$

The angular frequencies of the 3 phonons with wave vector \mathbf{k} are equal to the square roots of the eigenvalues of the 3×3 symmetric matrix D , whose elements are given by

$$\begin{aligned}
 D_{ii} &= \frac{8}{M} \sum_s \frac{n^s}{48} \sum_j \alpha_j^s \{2 - C_{j,i}^s [C_{j+1,i+1}^s C_{j+2,i+2}^s + C_{j+2,i+1}^s C_{j+1,i+2}^s]\} \\
 D_{i,i+1} &= \frac{8}{M} \sum_s \frac{n^s}{48} \sum_j \beta_j^s C_{j,i+2}^s [S_{j+1,i}^s S_{j+2,i+1}^s + S_{j+2,i}^s S_{j+1,i+1}^s] \\
 C_{j,i} &= \cos \pi a h_j^s k_i \\
 S_{j,i} &= \sin \pi a h_j^s k_i
 \end{aligned} \tag{2.29}$$

where i assumes the values 1, 2, 3, and the subscripts of the form $i+1$ and $i+2$ whose values are greater than 3 are to be interpreted as $i-2$ and $i-1$ respectively; $j+1$ and $j+2$ should be treated accordingly. The elements of the symmetric matrix are defined by

$$\begin{aligned}
 \alpha_1^s &= C_B(s) + \frac{h_1^s}{(h^s)^2} k_1(s) \\
 \alpha_2^s &= C_B(s) + \frac{h_2^s}{(h^s)^2} k_1(s) \\
 \alpha_3^s &= C_B(s) + \frac{h_3^s}{(h^s)^2} k_1(s)
 \end{aligned} \tag{2.30}$$

$$\begin{aligned}
 \beta_1^s &= \frac{h_2^s h_3^s}{(h^s)^2} k_1(s) \\
 \beta_2^s &= \frac{h_3^s h_1^s}{(h^s)^2} k_1(s) \\
 \beta_3^s &= \frac{h_1^s h_2^s}{(h^s)^2} k_1(s)
 \end{aligned} \tag{2.31}$$

where $h^s = \sqrt{(h_1^s)^2 + (h_2^s)^2 + (h_3^s)^2}$, and

$$\begin{aligned}
 C_B(s) &= \left. \frac{1}{r} \frac{d\phi(r)}{dr} \right|_{r=r^s} \\
 k_1(s) &= \left. \frac{d^2\phi(r)}{dr^2} \right|_{r=r^s} - \left. \frac{1}{r} \frac{d\phi(r)}{dr} \right|_{r=r^s}
 \end{aligned}$$

Table 2.1 show the values of h_1 , h_2 , h_3 , and the number of neighbors n for the first 12 shells.

Table 2.1: List of neighbours for face-centred cubic crystals.

s	$h_1h_2h_3$	n
1	1 1 0	12
2	2 0 0	6
3	2 1 1	24
4	2 2 0	12
5	3 1 0	24
6	2 2 2	8
7	3 2 1	48
8	4 0 0	6
9	3 3 0	12
10	4 1 1	24
11	4 2 0	24
12	3 3 2	24

2.0.7 Results for the Phonon Dispersion Curves

Figures 2.1-2.7 depict the phonon dispersion curves for Ne, Ar, Kr, and Xe for the [100], [110], and [111] principal symmetry directions. All the calculations employ the quasiharmonic theory. We did not include the phonon dispersion results for the Aziz and LJ potential in figure 2.1 because the results were in poor agreement with the experimental values. Also, the results for the Exp-6-8 potential for ^{36}Ar were not included in figure 2.2 due to poor agreement with the experimental values. We also note that the phonon dispersion calculations were done for ^{36}Ar and not ^{38}Ar . This is because ^{38}Ar is an unfavourable material for many neutron measurements because it has a small coherent cross section ($\sigma_{coh} = 0.40b$) and an appreciable incoherent cross section ($\sigma_{incoh} = 0.25b$) [27]. To our knowledge, the data for

natural Ar are not very accurate and only available in the large-wave-vector region. We calculate the percent errors for the Ne, Ar, Kr, and Xe dispersion calculations at the zone boundaries in the $[100]$, and $[111]$ principal symmetry directions in chapter 5.

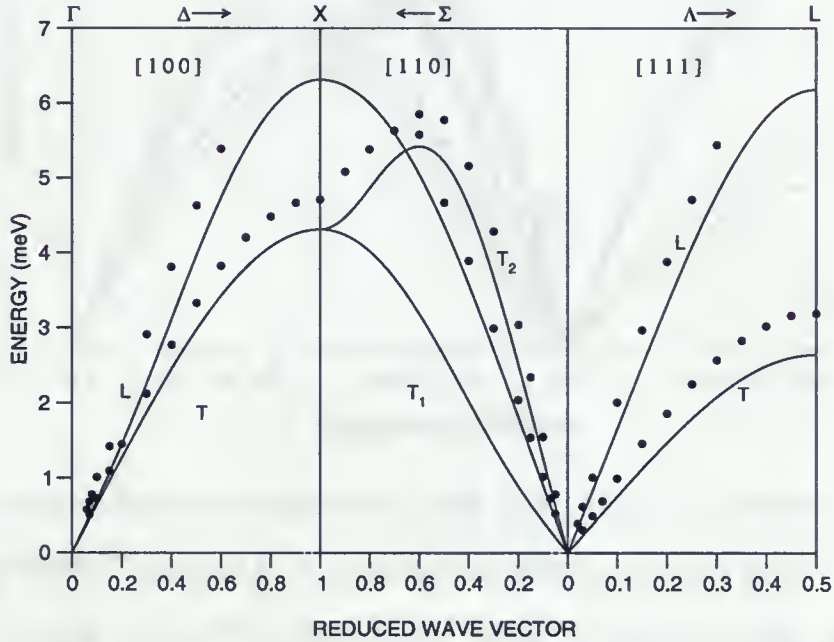


Figure 2.1: Phonon-dispersion relations in $[100]$, $[110]$, and $[111]$ principal symmetry directions in Ne at 10 K. •, experimental measurements from [28]. The calculations are from the quasiharmonic theory using the Eggenberger potential sixth-shell calculations.

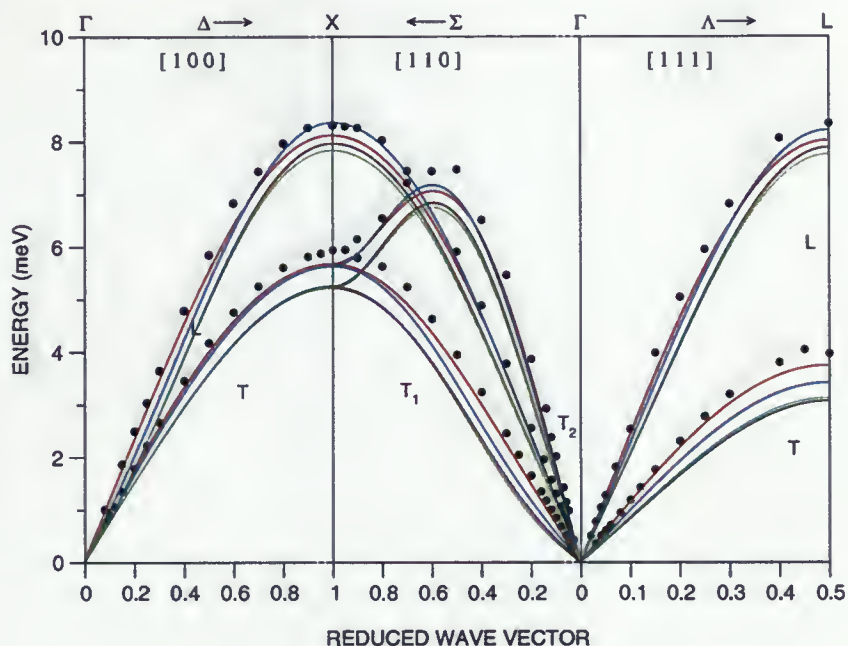


Figure 2.2: Phonon-dispersion relations in [100], [110], and [111] principal symmetry directions for ^{36}Ar at 10 K. •, experimental measurements from [27]. The calculations are from the quasiharmonic theory using the Exp-6 potential sixth-shell calculations (black lines), Aziz potential sixth-shell calculations (red lines), Morse-type potential sixth-shell calculations (blues lines), LJ potential sixth-shell calculations (green lines).

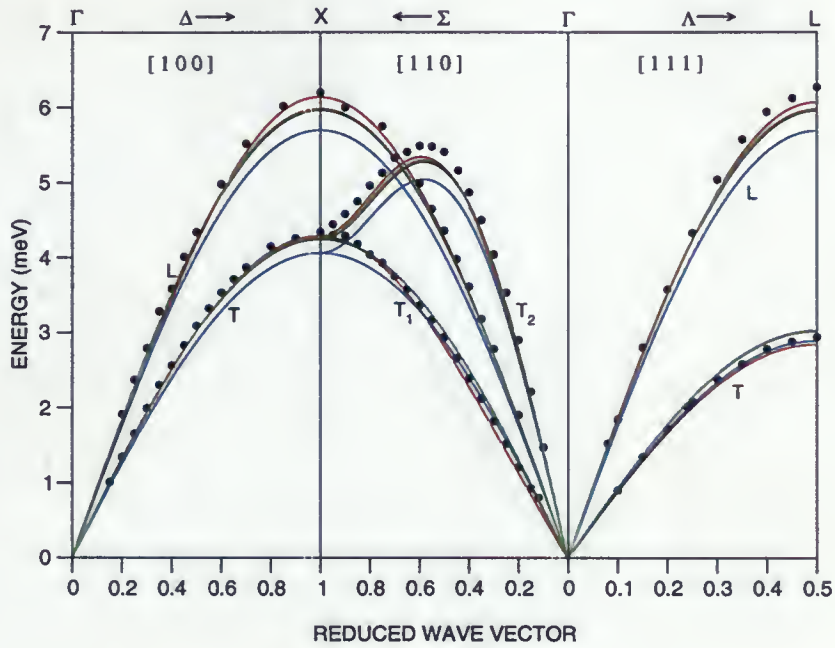


Figure 2.3: Phonon-dispersion relations in [100], [110], and [111] principal symmetry directions for Kr at 10 K. •, experimental measurements from [29]. The calculations are from the quasi-harmonic theory using the Morse potential first-shell calculations (black lines), Aziz potential sixth-shell calculations (red lines), LJ potential first-shell calculations (blue lines), Rydberg potential first-shell calculations (green lines).

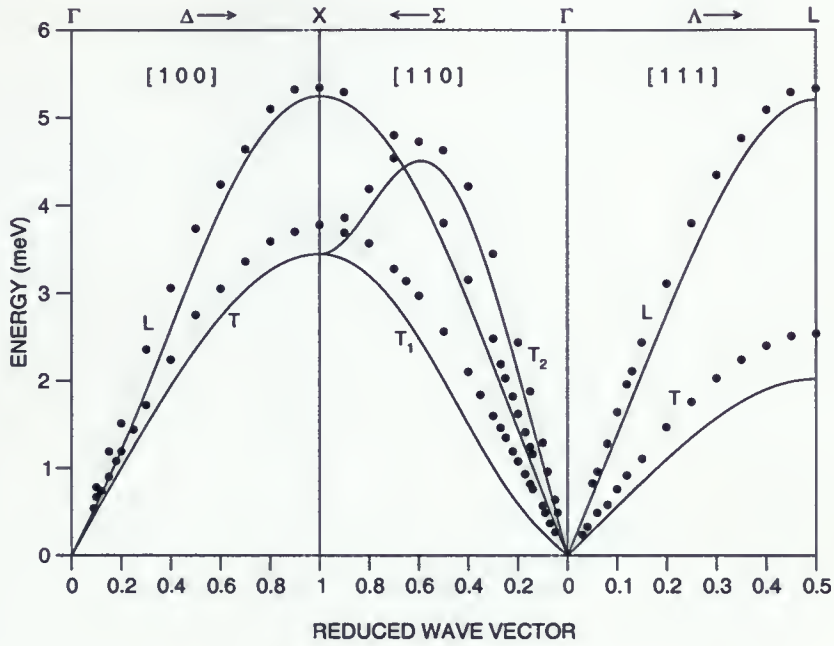


Figure 2.4: Phonon dispersion curves for Xe using the Exp-6 potential sixth-shell calculations. The solid lines are the theoretical calculations from quasiharmonic theory. ●, experimental measurements from [30].

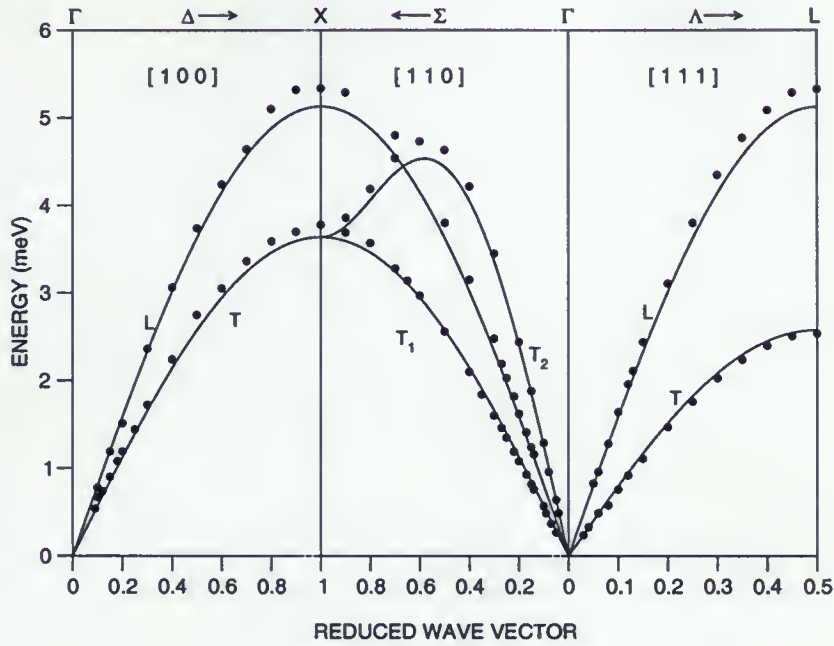


Figure 2.5: Phonon dispersion curves for Xe using the Rydberg potential first-shell calculations. The solid lines are the theoretical calculations from quasiharmonic theory. •, experimental measurements from [30].

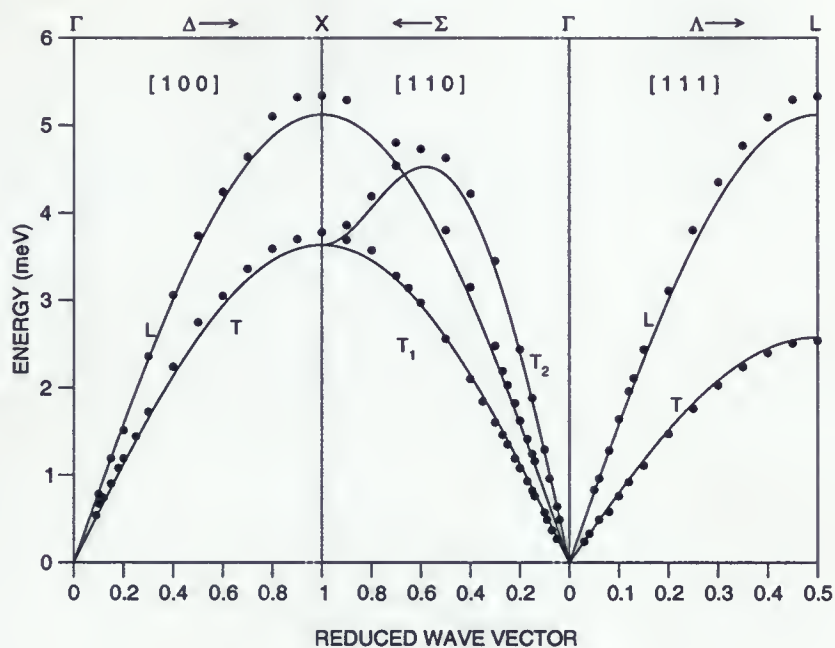


Figure 2.6: Phonon dispersion curves for Xe using the Morse potential first-shell calculations.

The solid lines are the theoretical calculations from quasiharmonic theory. •, experimental measurements from [30].

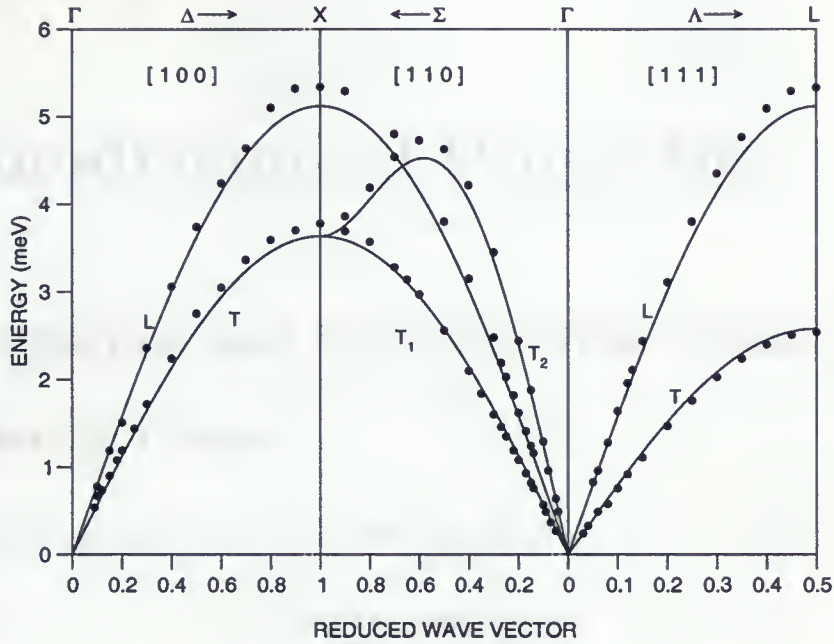


Figure 2.7: Phonon dispersion curves for Xe using the LJ potential first-shell calculations.

The solid lines are the theoretical calculations from quasi-harmonic theory. •, experimental measurements from [30].

Chapter 3

Thermodynamical Properties

3.1 Isothermal and Adiabatic Bulk Moduli, and Specific Heats

The harmonic Hamiltonian for lattice vibrations is given by

$$H_H = \sum_{\mathbf{k}s} \hbar \omega_s(\mathbf{k}) [A_{\mathbf{k}s}^+ A_{\mathbf{k}s} + 1/2]. \quad (3.1)$$

The various symbols appearing in equation 3.1 are defined as follows: \hbar is Planck's constant divided by 2π , $\omega_s(\mathbf{k})$ where $s = 1, 2, 3$ are the phonon frequencies at wave vector \mathbf{k} , $A_{\mathbf{k}s}^+$ and $A_{\mathbf{k}s}$ are the creation and annihilation operators for a phonon of wave vector \mathbf{k} and polarization s . $A_{\mathbf{k}s}^+ A_{\mathbf{k}s} = n_{\mathbf{k}s}$ is the number operator of the phonon state (\mathbf{k}, s) with eigenvalue $n_{\mathbf{k}s}$. Thus, the harmonic energy of the set of $n_{\mathbf{k}s}$ phonons in each phonon state \mathbf{k} is given by

$$E_H\{n_{\mathbf{k}s}\} = \sum_{\mathbf{k}} \sum_{s=1}^3 \left(n_{\mathbf{k}s} + \frac{1}{2} \right) \hbar \omega_s(\mathbf{k}), \quad (3.2)$$

where $n_{\mathbf{k}s} = 0, 1, 2, \dots$. The harmonic partition function is

$$Z_H = \text{Tr}\{\exp(-\beta H)\}, \quad (3.3)$$

where $\beta = 1/k_B T$.

$$\begin{aligned} Z_H &= \sum_{n_{\mathbf{k}_1 s_1}=0}^{\infty} \cdots \sum_{n_{\mathbf{k}_N s_3}=0}^{\infty} \exp \left[-\beta \sum_{\mathbf{k}s} \hbar \omega_s(\mathbf{k}) (n_{\mathbf{k}s} + 1/2) \right] \\ &= \prod_{\mathbf{k}s} \frac{\exp(-\frac{1}{2}\beta \hbar \omega_s(\mathbf{k}))}{1 - \exp(-\beta \hbar \omega_s(\mathbf{k}))} \end{aligned} \quad (3.4)$$

The corresponding free energy is given by

$$\begin{aligned}
 F_H &= -k_B T \ln Z_H \\
 &= -k_B T \sum_{\mathbf{k}s} \{ \ln e^{-\frac{1}{2}\beta \hbar \omega_s(\mathbf{k})} + \ln [1 - e^{-\beta \hbar \omega_s(\mathbf{k})}]^{-1} \} \\
 &= k_B T \sum_{\mathbf{k}s} \ln \left[2 \sinh \left(\frac{\hbar \omega_s(\mathbf{k})}{2k_B T} \right) \right].
 \end{aligned} \tag{3.5}$$

The total free energy in the quasiharmonic approximation is just

$$\begin{aligned}
 F(a, T) &= U_{static}(a) + F_H(a, T) \\
 &= \frac{1}{2} \sum_s n_s \phi_s(r) + k_B T \sum_{\mathbf{k},j} \ln \left[2 \sinh \left(\frac{\hbar \omega_j(\mathbf{k}, a)}{2k_B T} \right) \right],
 \end{aligned} \tag{3.6}$$

where $j = 1, 2, 3$, $U_{static}(a)$ is the total static energy for a given volume V , ϕ is the potential, and s denotes the shell number of the neighboring atoms n with respect to the origin $\mathbf{0}$. We calculate the equilibrium lattice parameter $a_{eq}(T)$ by fixing T , minimizing the free energy, and solving for a :

$$\left(\frac{\partial F(a, T)}{\partial a} \right)_T = \frac{\partial U(a)}{\partial a} + \left(\frac{\partial F_H(a, T)}{\partial a} \right)_T = 0. \tag{3.7}$$

We calculate the free energy per atom analytically by evaluating F_H on a $20 \times 20 \times 20$ \mathbf{k} -point mesh in the Brillouin Zone. We obtain the thermodynamic properties from the following equations:

$$C_V = -T \left(\frac{\partial^2 F}{\partial T^2} \right)_V \tag{3.8}$$

is the specific heat at constant volume,

$$B_T = V \left(\frac{\partial^2 F}{\partial V^2} \right)_T \tag{3.9}$$

is the isothermal bulk modulus at fixed T ,

$$\beta = -\frac{1}{B_T} \left(\frac{\partial^2 F}{\partial V \partial T} \right) \tag{3.10}$$

is the volume expansion,

$$C_P = C_V + TV B_T \beta^2 \tag{3.11}$$

is the specific heat at constant pressure, and

$$B_S = \frac{C_P}{C_V} B_T \quad (3.12)$$

is the adiabatic bulk modulus.

3.1.1 Results for the Thermal Expansion of the Isothermal and Adiabatic Bulk Moduli, and Specific Heats

Figures 3.1-3.20 depict the results of the thermodynamic properties for Ne, Ar, Kr, and Xe. The labels QH represent the quasiharmonic calculations. We discuss the results of these calculations in chapter 5.

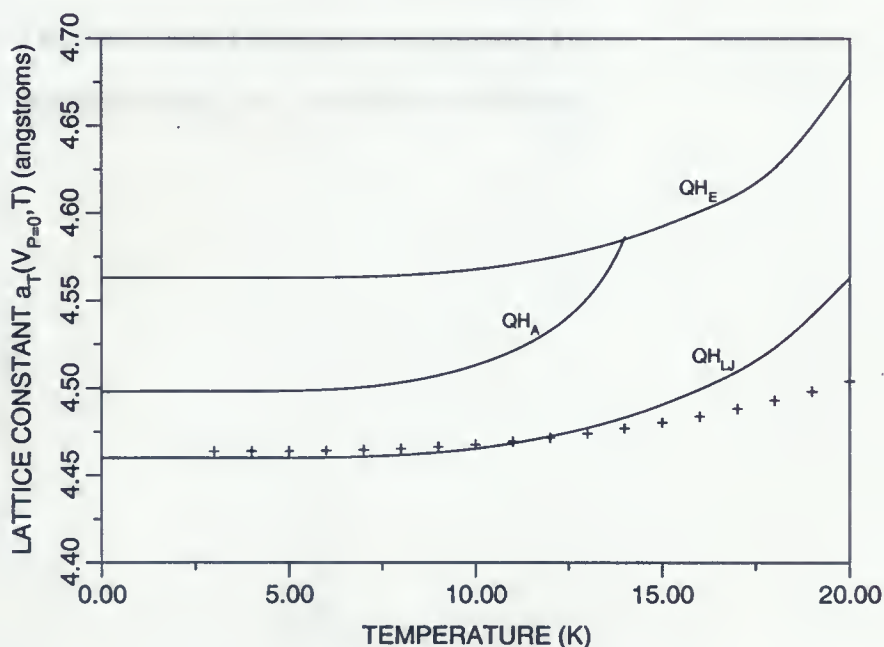


Figure 3.1: Lattice constant (a_T) at zero pressure for Ne. +, experimental points [31]; the labels for each line are defined in the text.

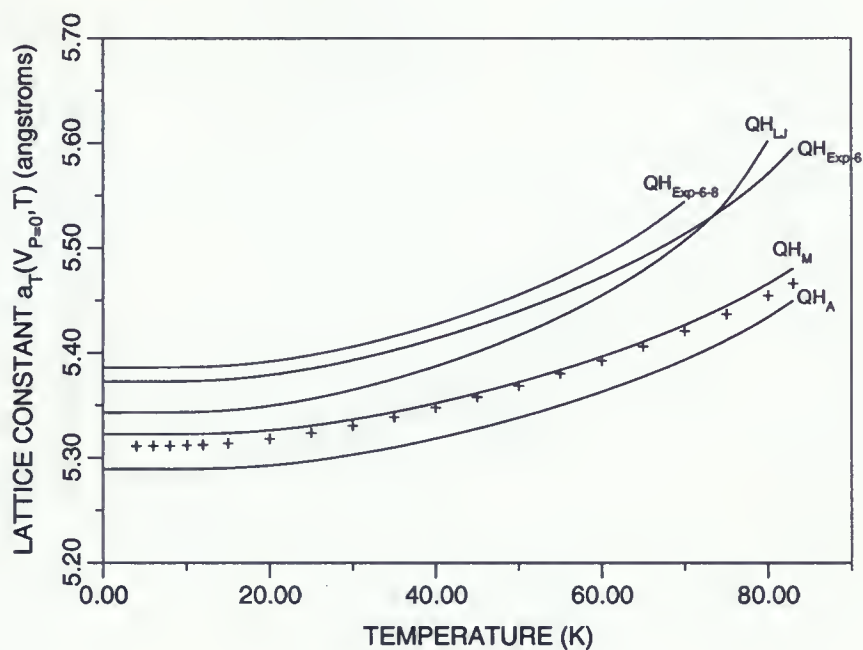


Figure 3.2: Lattice constant (a_T) at zero pressure for Ar. +, experimental points [31]; the labels for each line are defined in the text.

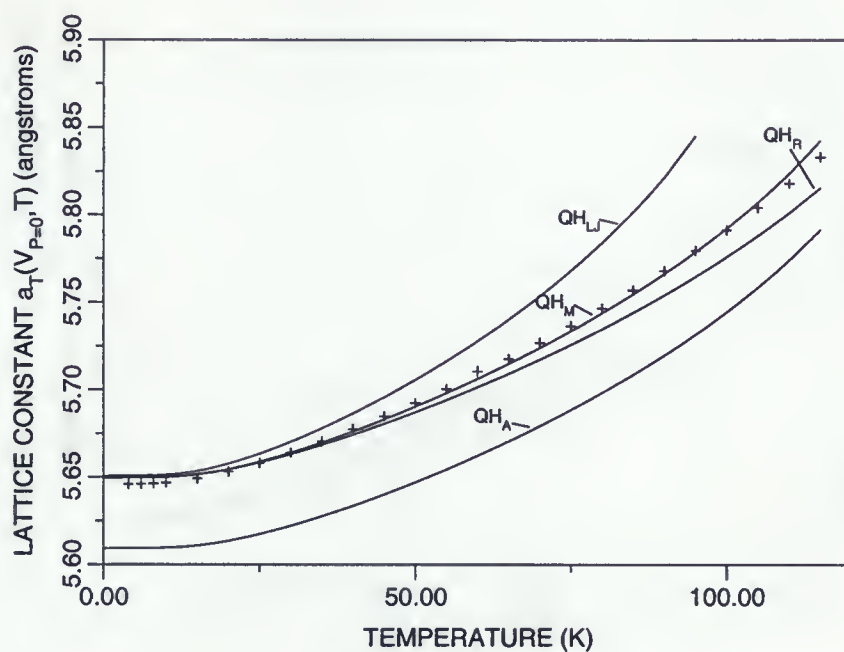


Figure 3.3: Lattice constant (a_T) at zero pressure for Kr. +, experimental points [31]; the labels for each line are defined in the text.

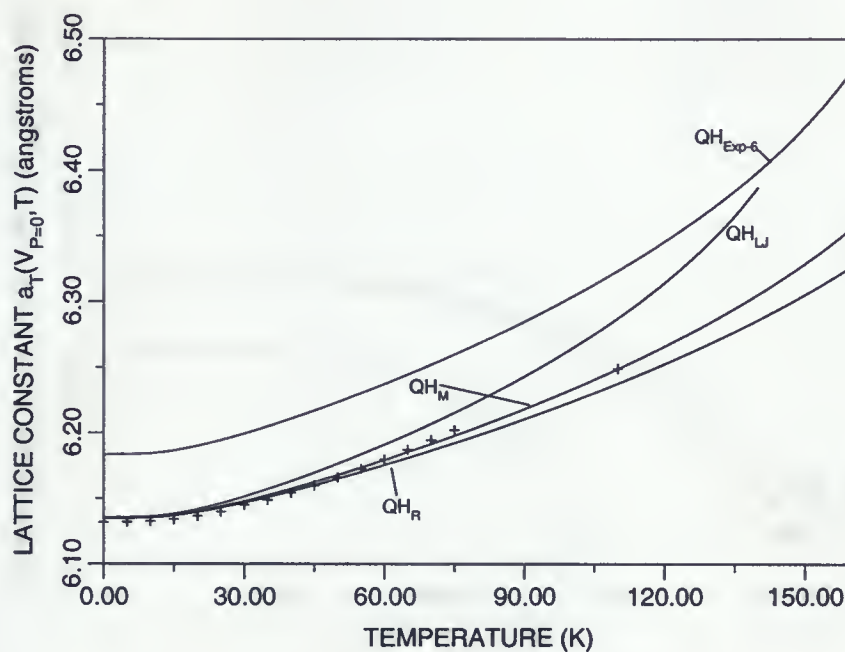


Figure 3.4: Lattice constant (a_T) at zero pressure for Xe. +, experimental points [31]; the labels for each line are defined in the text.

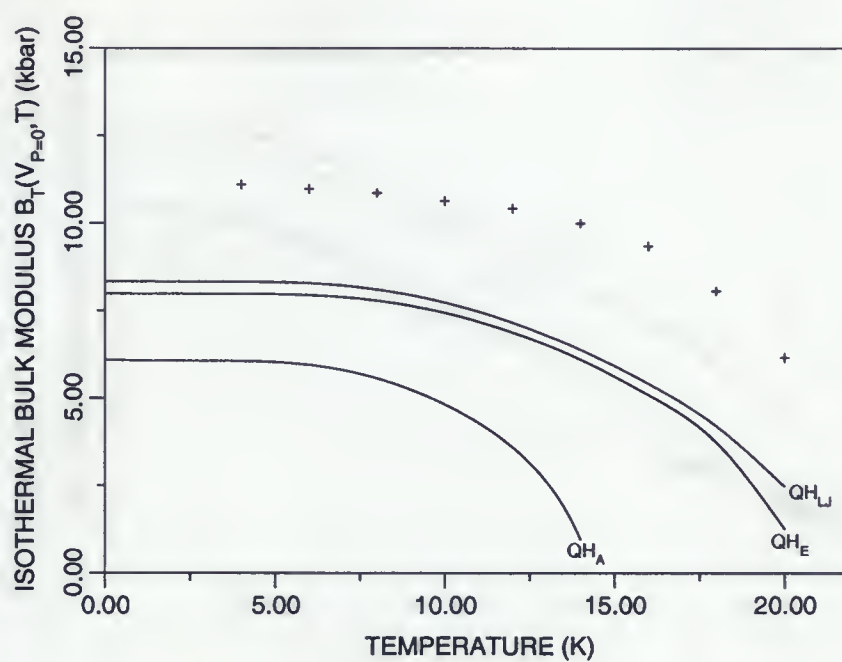


Figure 3.5: Isothermal bulk modulus (B_T) for Ne. +, experimental points [31]; the labels for each line are defined in the text.

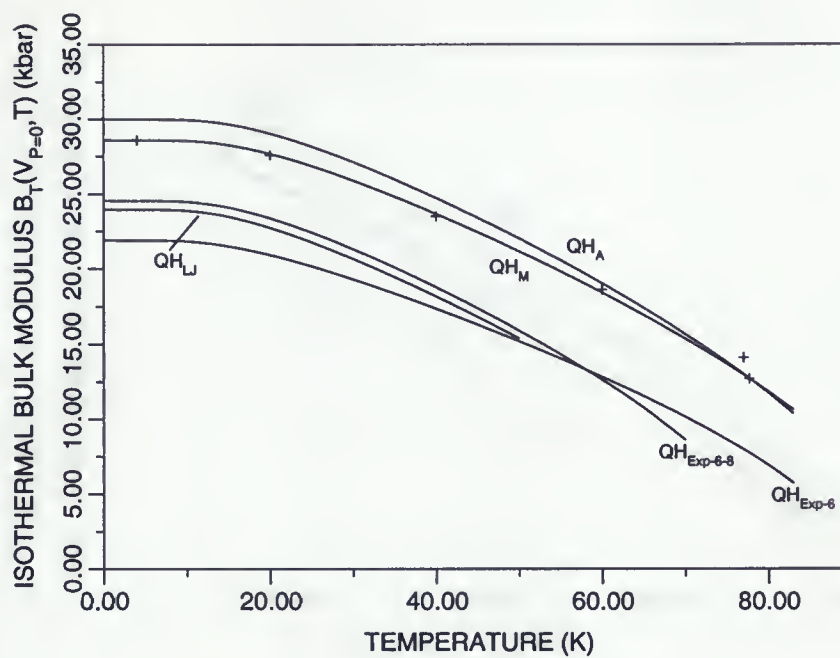


Figure 3.6: Isothermal bulk modulus (B_T) for Ar. +, experimental points [31]; the labels for each line are defined in the text.

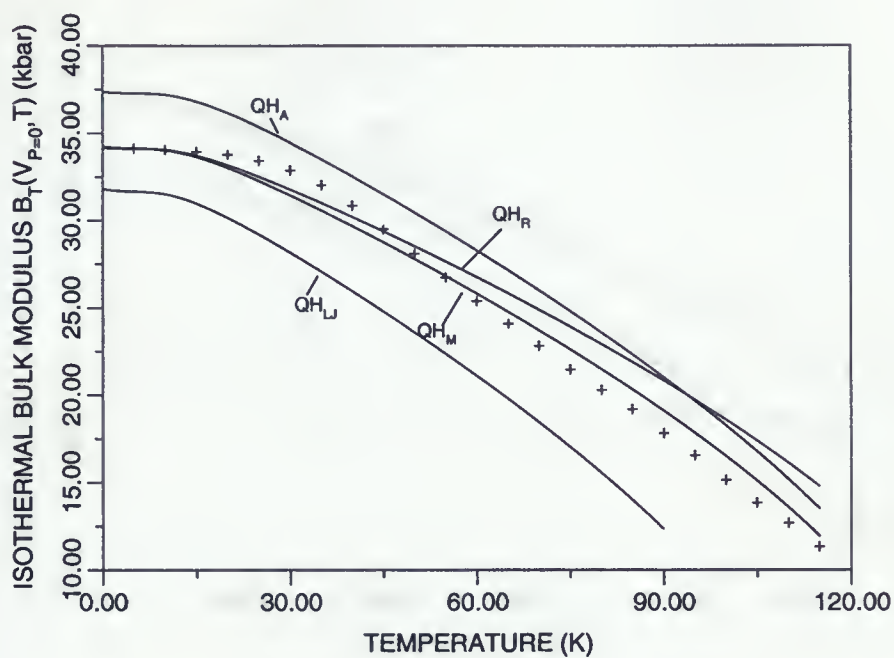


Figure 3.7: Isothermal bulk modulus (B_T) for Kr. +, experimental points [31]; the labels for each line are defined in the text.

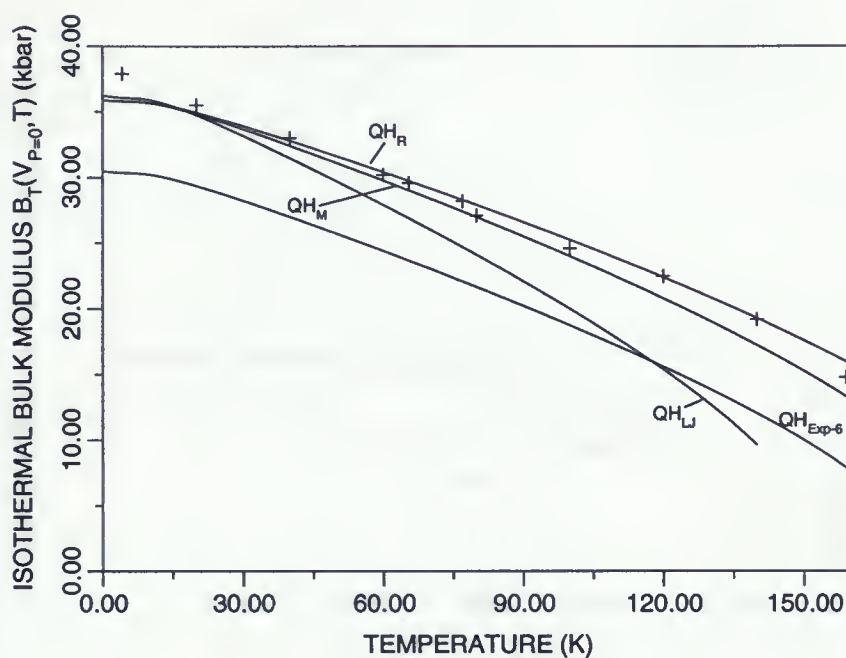


Figure 3.8: Isothermal bulk modulus (B_T) for Xe. +, experimental points [31]; the labels for each line are defined in the text.

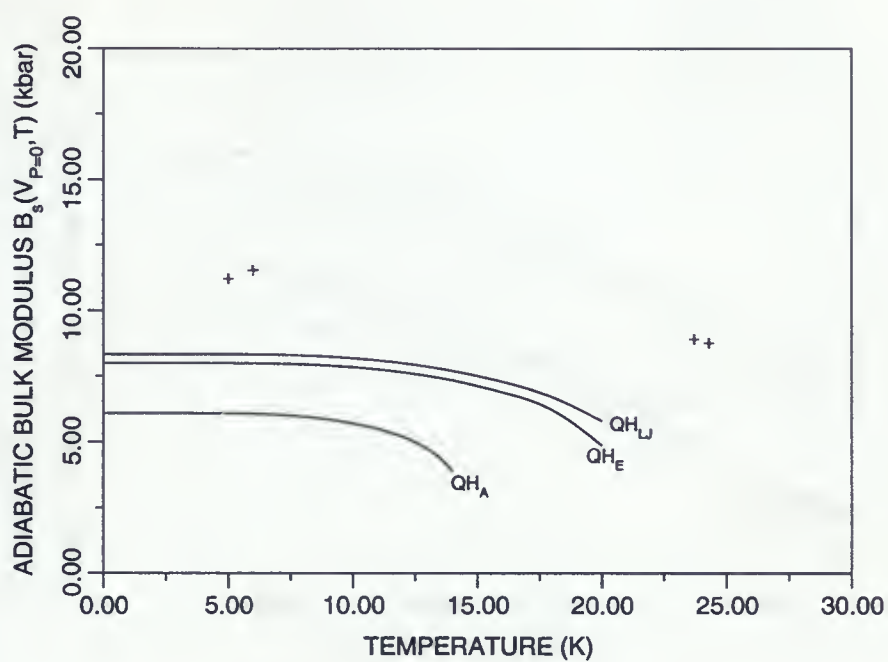


Figure 3.9: Adiabatic bulk modulus (B_s) for Ne. +, experimental points [31]; the labels for each line are defined in the text.

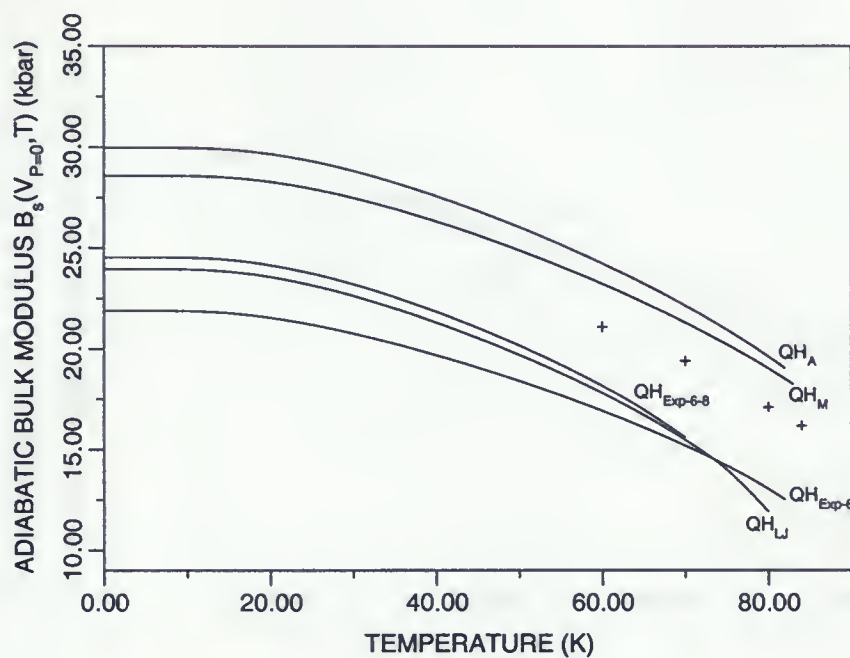


Figure 3.10: Adiabatic bulk modulus (B_s) for Ar. +, experimental points [31]; the labels for each line are defined in the text.

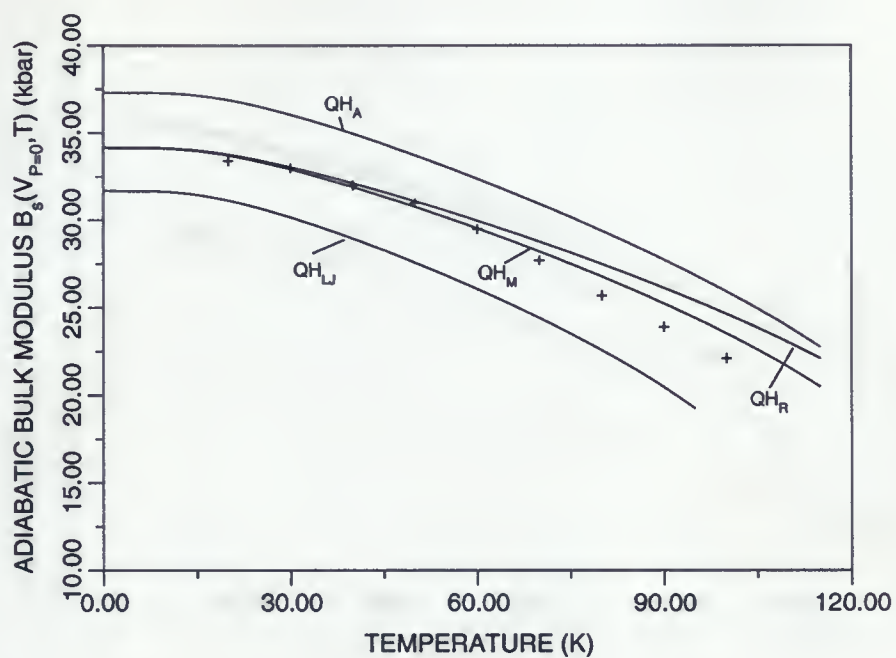


Figure 3.11: Adiabatic bulk modulus (B_s) for Kr. +, experimental points [31]; the labels for each line are defined in the text.

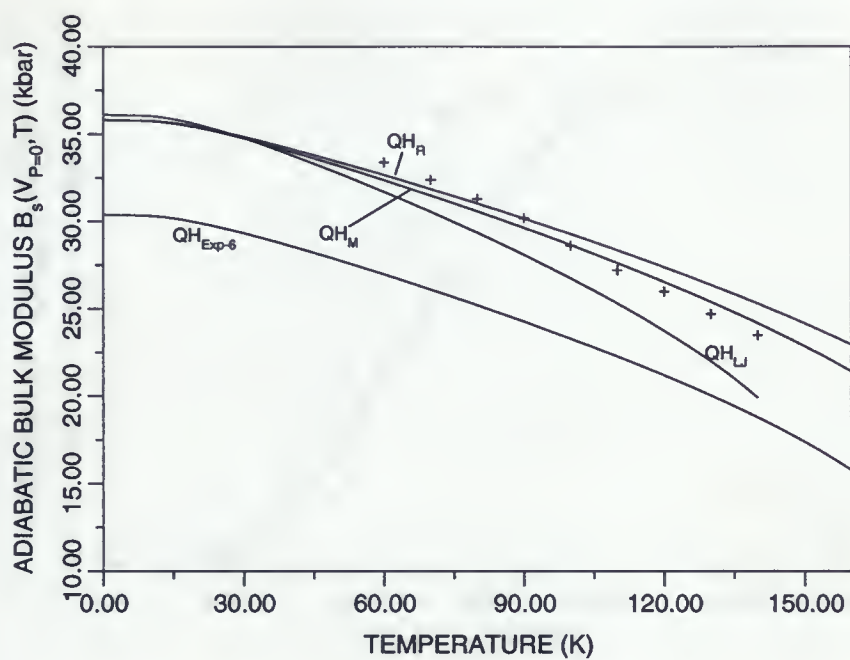


Figure 3.12: Adiabatic bulk modulus (B_s) for Xe. +, experimental points [31]; the labels for each line are defined in the text.

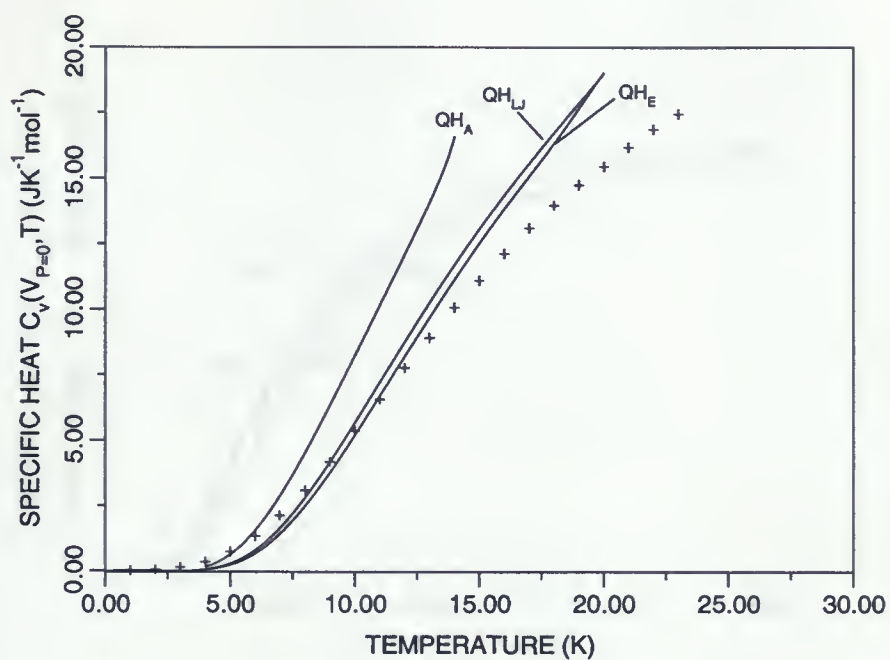


Figure 3.13: Specific heat at constant volume (C_V) for Ne. +, experimental points [31]; the labels for each line are defined in the text.

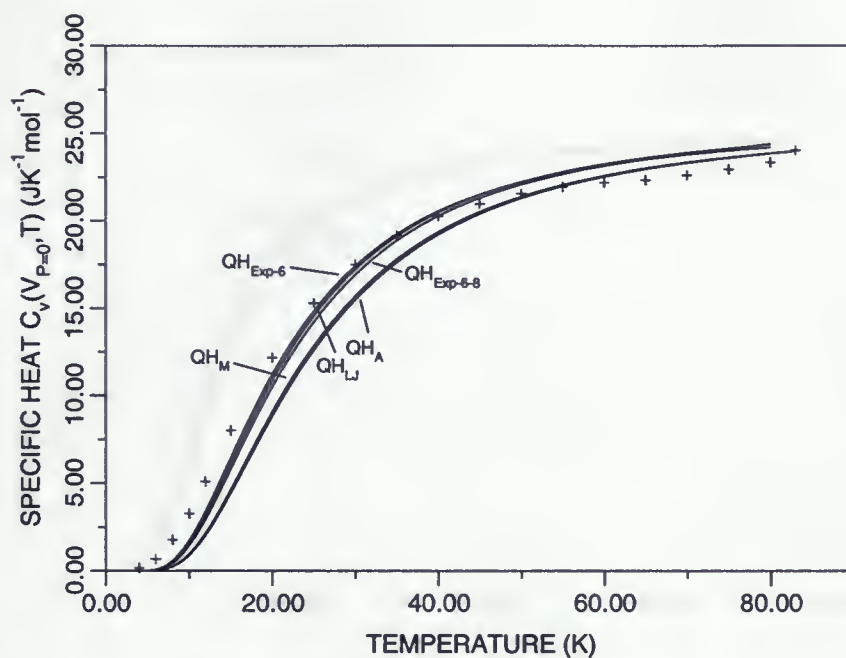


Figure 3.14: Specific heat at constant volume (C_V) for Ar. +, experimental points [32]; the labels for each line are defined in the text.

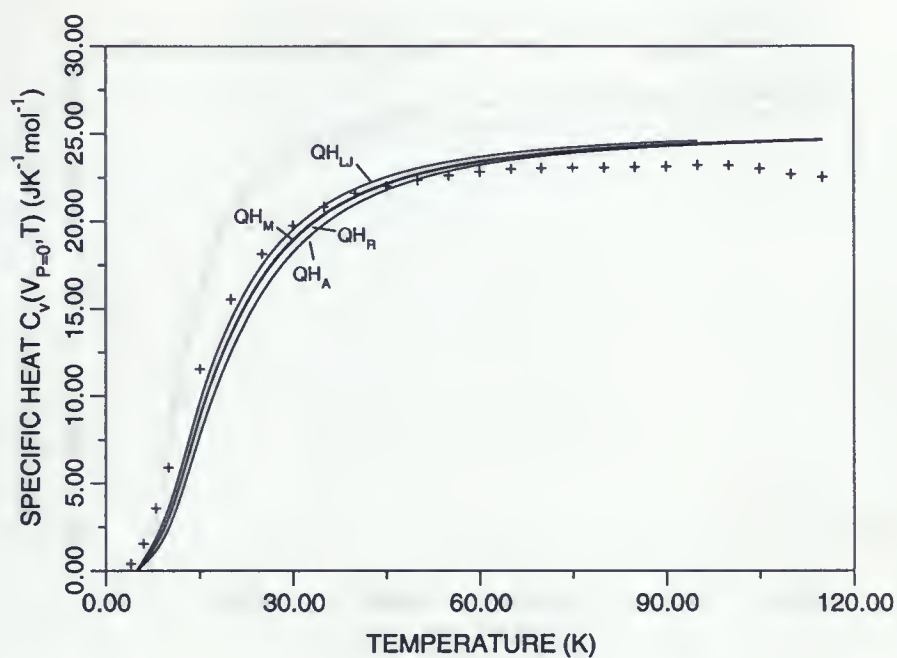


Figure 3.15: Specific heat at constant volume (C_V) for Kr. +, experimental points [33]; the labels for each line are defined in the text.

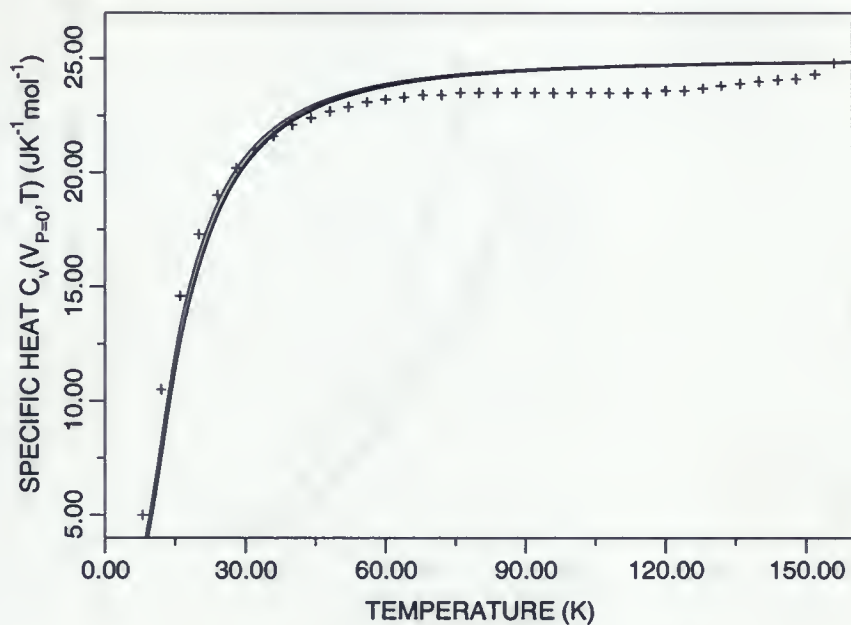


Figure 3.16: Specific heat at constant volume (C_V) for Xe. +, experimental points [34]. The labels for each line are not shown because of the proximity of each curve with respect to the others are very close.

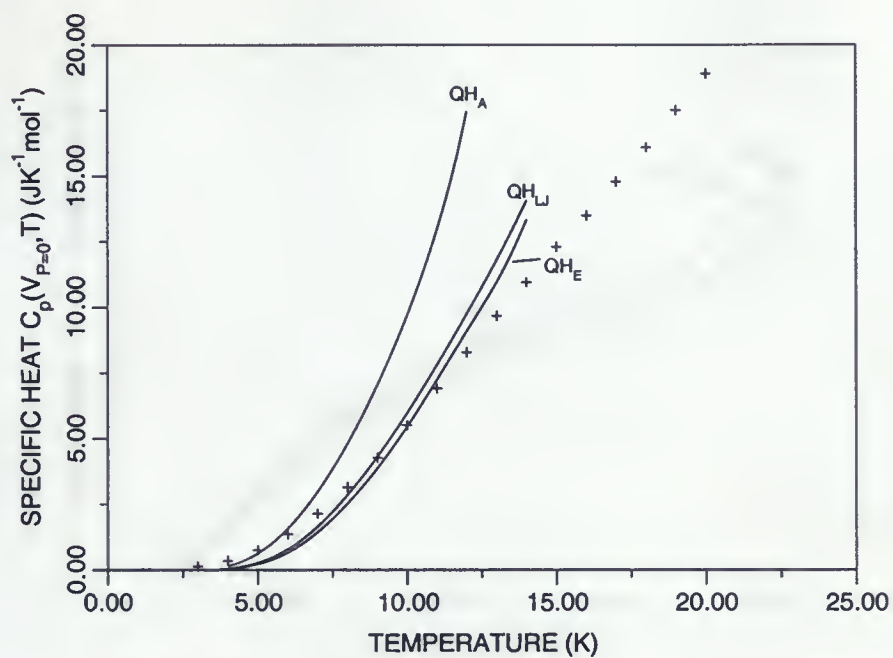


Figure 3.17: Specific heat at constant pressure (C_P) for Ne. +, experimental points [31]; the labels for each line are defined in the text.

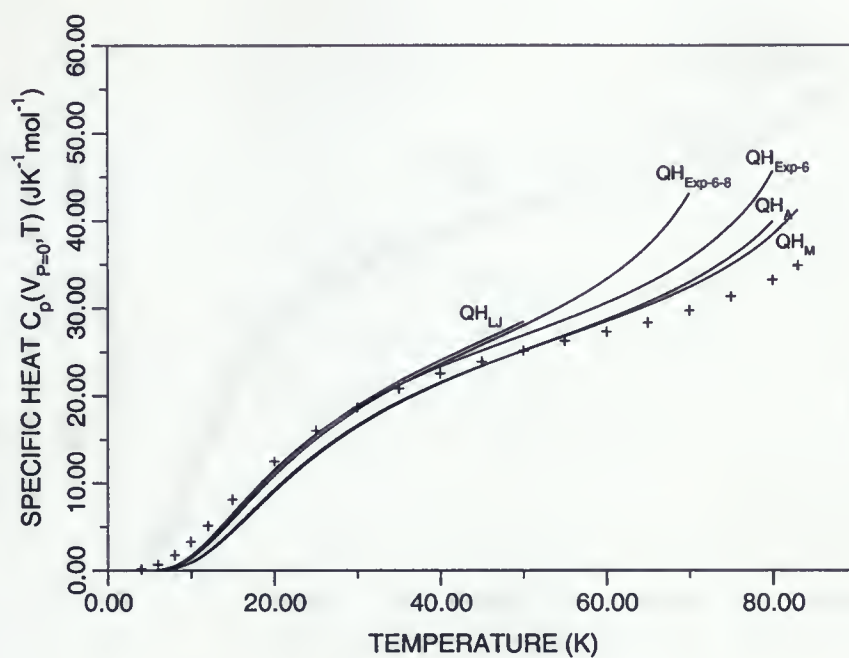


Figure 3.18: Specific heat at constant pressure (C_P) for Ar. +, experimental points [31]; the labels for each line are defined in the text.

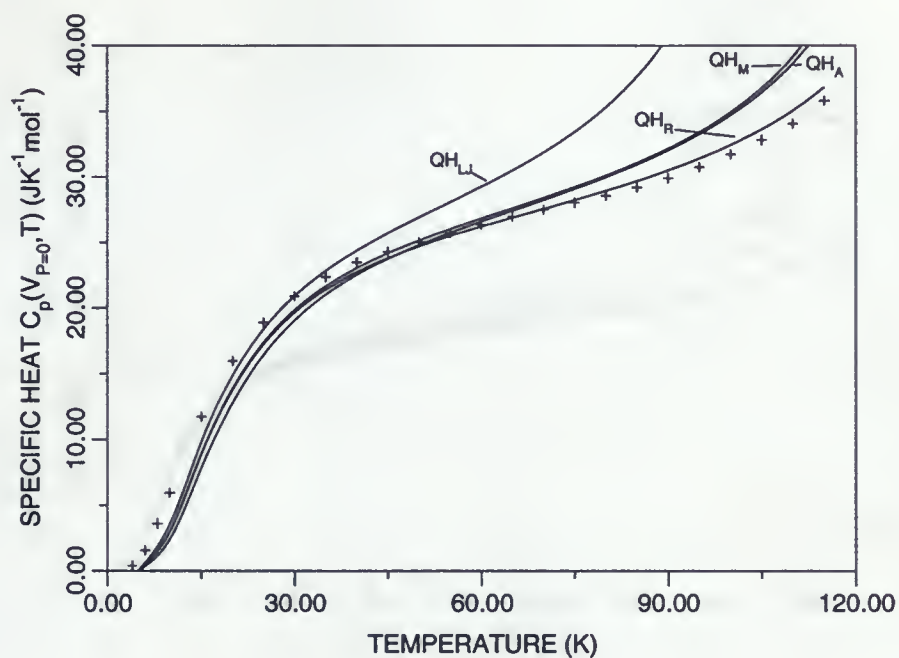


Figure 3.19: Specific heat at constant pressure (C_P) for Kr. +, experimental points [31]; the labels for each line are defined in the text.

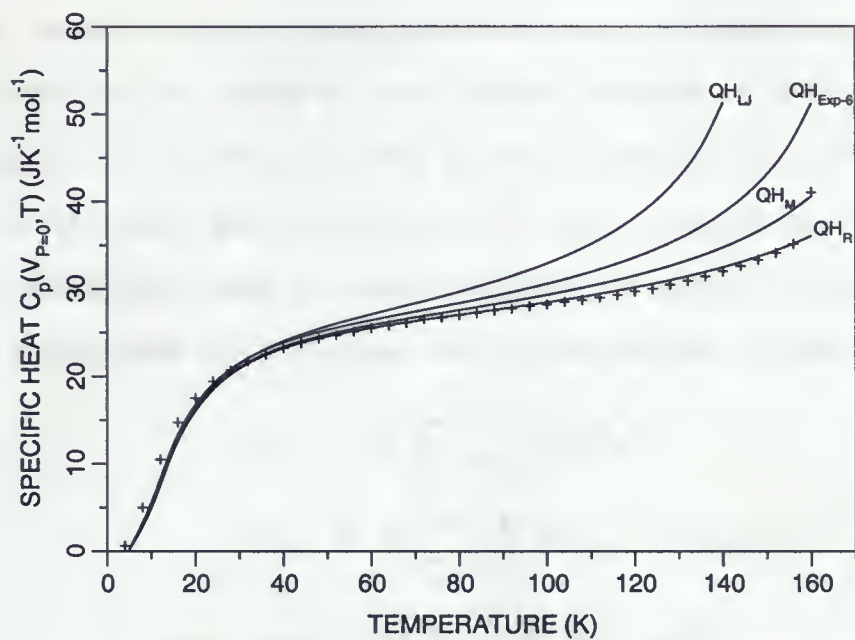


Figure 3.20: Specific heat at constant pressure (C_P) for Xe. +, experimental points [31]; the labels for each line are defined in the text.

3.2 Elastic Constants via the Long Wavelength Limit

There are a number of ways to obtain the elastic constants: either via homogeneous deformations method [35, 36], directly from the dispersion relations, or via long wave length limit method [26, 37]. In this thesis we choose the long wavelength limit method. The relations between the interatomic force constants and the elastic constants c_{11} , c_{44} , and c_{12} are obtained by allowing $|\mathbf{k}|$ to tend to zero and comparing the matrix D with the corresponding matrix for elastic waves in a continuum. For face-centered cubic crystals the relations are

$$\begin{aligned} ac_{11} &= 8 \sum_s \frac{n^s}{48} \sum_j (h_j^s)^2 \alpha_j^s \\ ac_{44} &= 4 \sum_s \frac{n^s}{48} \sum_j [(h_{j+1}^s)^2 + (h_{j+2}^s)^2] \alpha_j^s \\ a(c_{12} + c_{44}) &= 16 \sum_s \frac{n^s}{48} \sum_j h_{j+1}^s h_{j+2}^s \beta_j^s, \end{aligned} \quad (3.13)$$

where α_j^s , β_j^s , h_j^s , and n^s are defined above in chapter 2. The Cauchy equality for a cubic crystal for the nearest neighbor model is defined as $c_{12} = c_{44}$. This equality will hold for a pair potential $\phi(r)$ when the potential has a minimum at the nearest neighbor distance r_{nn} :

$$\phi'(r)|_{r=r_{nn}} = 0. \quad (3.14)$$

Differences between c_{12} and c_{44} increase with temperature because the minimum in $\phi(r)$ moves further away from $r = r_{nn}$.

3.2.1 Results for the Elastic Constants via the Long Wavelength Limit

Figures 3.21-3.32 depict the results of the calculation of the elastic constants c_{11} , c_{12} , and c_{44} as a function of temperature T , for Ne, Ar, Kr, and Xe. The labels QH represent the quasiharmonic calculations. The elastic constants were obtained via the minimization of the

Helmholtz free energy at a given temperature T , solving for the lattice parameter a , and using these results in equation 3.13. The subscripts E represent the Eggenberger potential, A the Aziz potential, LJ the Lennard-Jones potential, Exp-6 the exponential-six potential, Exp-6-8 the exponential-six-eight potential, M the Morse potential, and R the Rydberg potential. In chapter 5, we calculated the percent errors of the elastic constants c_{11} , c_{12} , and c_{44} for Ne, Ar, Kr, and Xe.

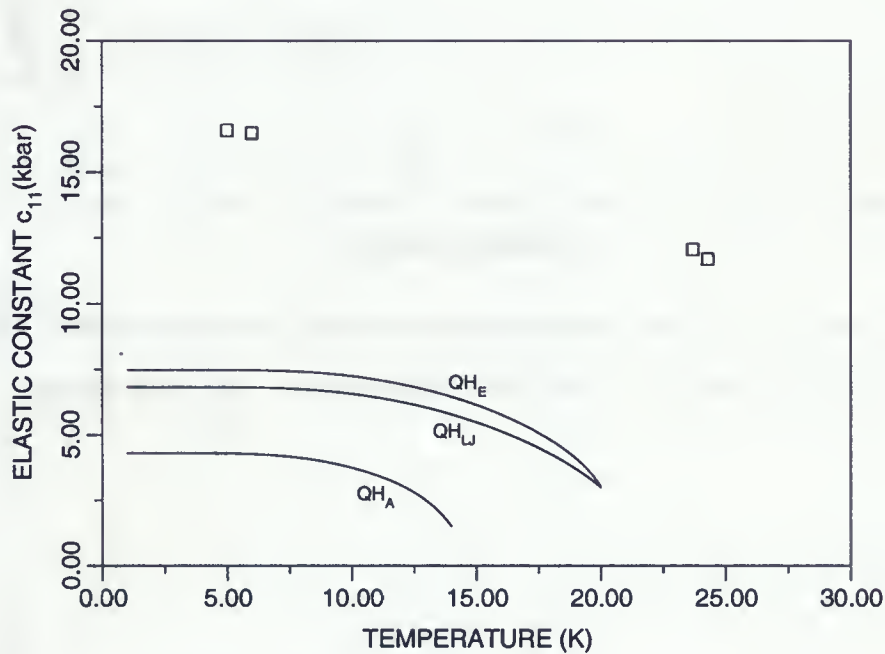


Figure 3.21: Elastic constant c_{11} via the long wavelength limit for Ne. \square are the experimental points from [31]. The labels for each line are defined in the text.

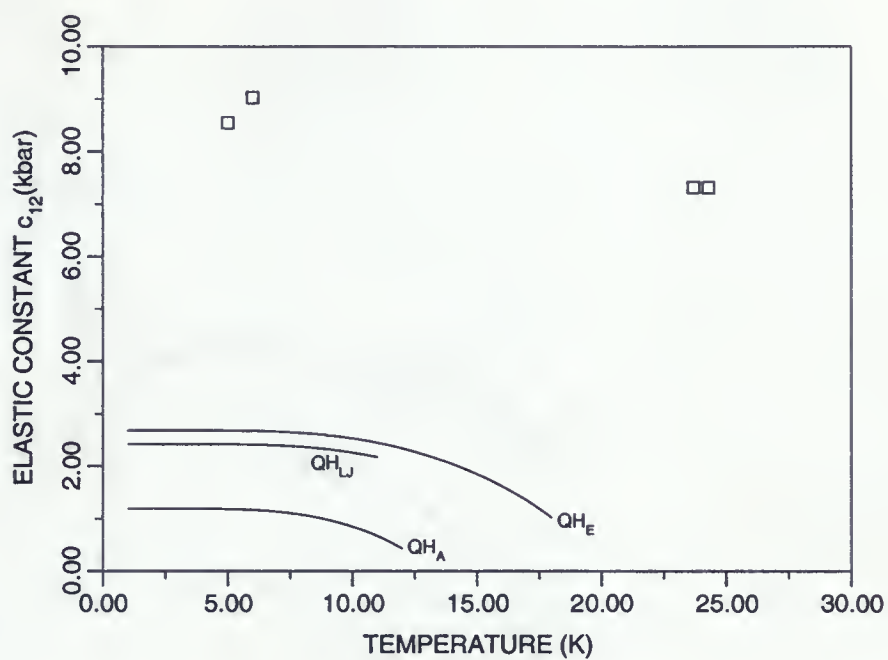


Figure 3.22: Elastic constant c_{12} via the long wavelength limit for Ne. \square are the experimental points from [31]. The labels for each line are defined in the text.

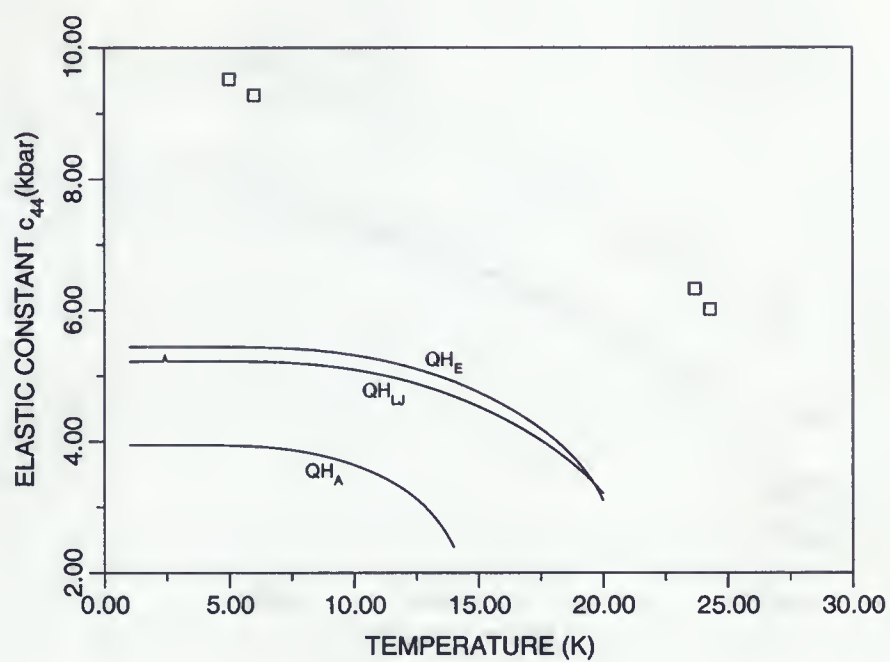


Figure 3.23: Elastic constant c_{44} via the long wavelength limit for Ne. \square are the experimental points from [31]. The labels for each line are defined in the text.

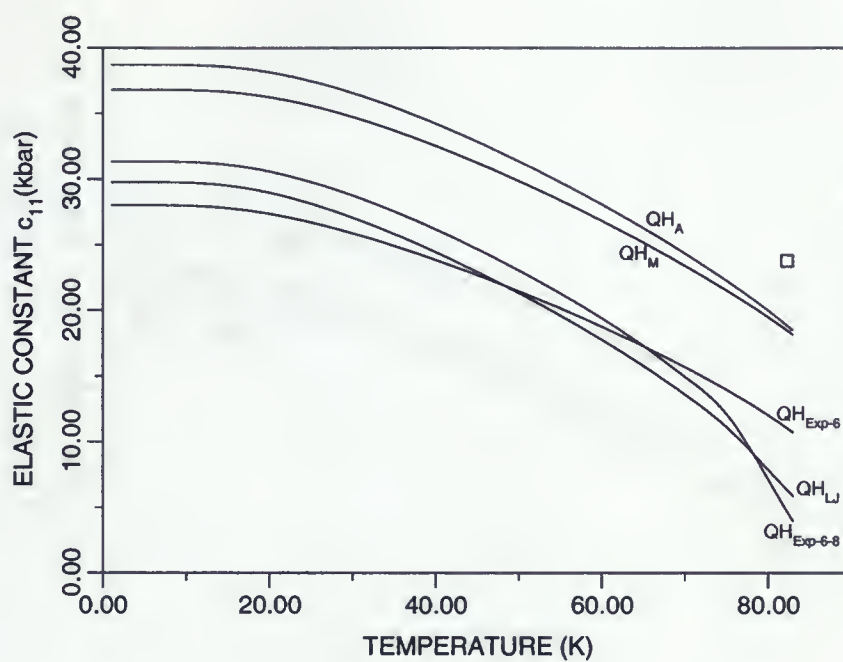


Figure 3.24: Elastic constant c_{11} via the long wavelength limit for Ar. \square are the experimental points from [31]. The labels for each line are defined in the text.

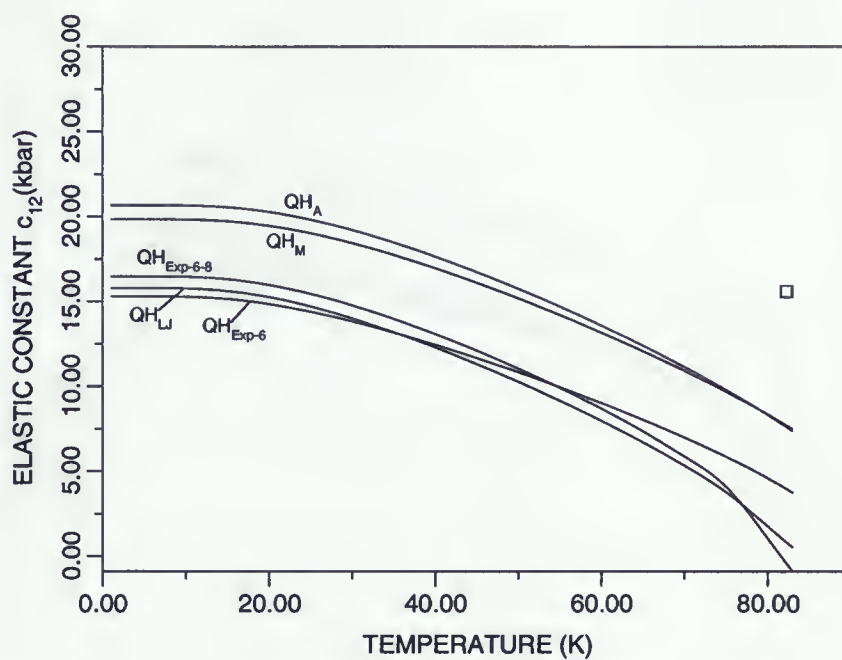


Figure 3.25: Elastic constant c_{12} via the long wavelength limit for Ar. \square are the experimental points from [31]. The labels for each line are defined in the text.

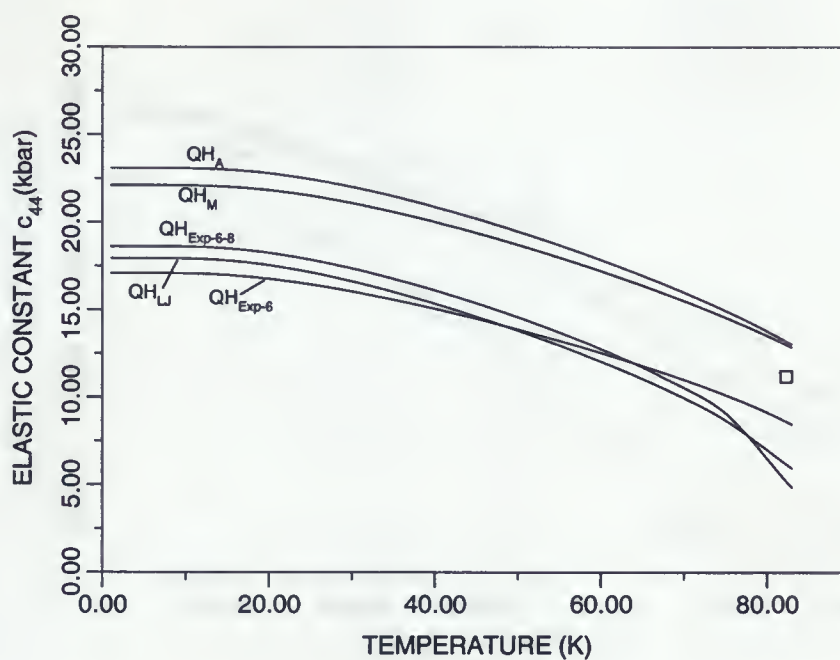


Figure 3.26: Elastic constant c_{44} via the long wavelength limit for Ar. \square are the experimental points from [31]. The labels for each line are defined in the text.

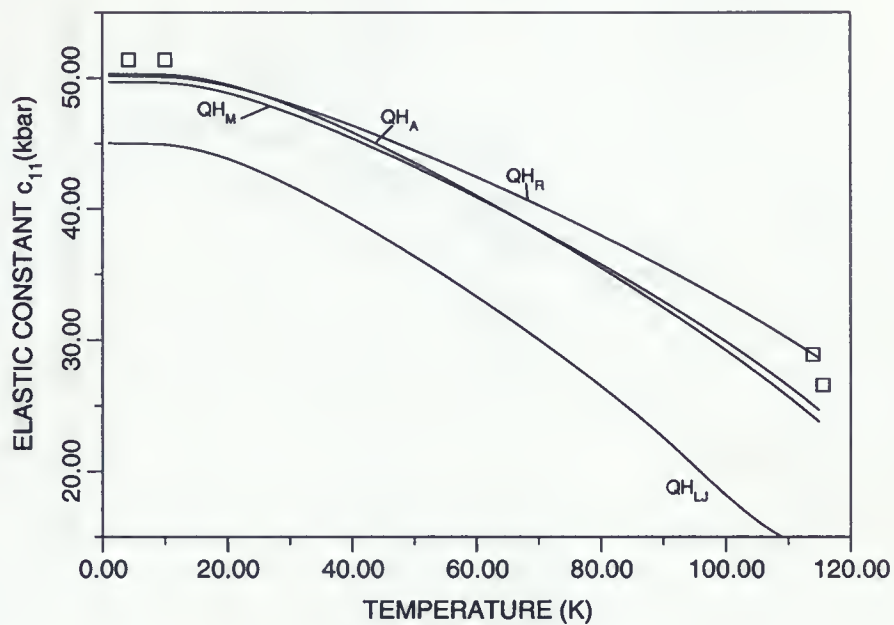


Figure 3.27: Elastic constant c_{11} via the long wavelength limit for Kr. \square are the experimental points from [31]. The labels for each line are defined in the text.

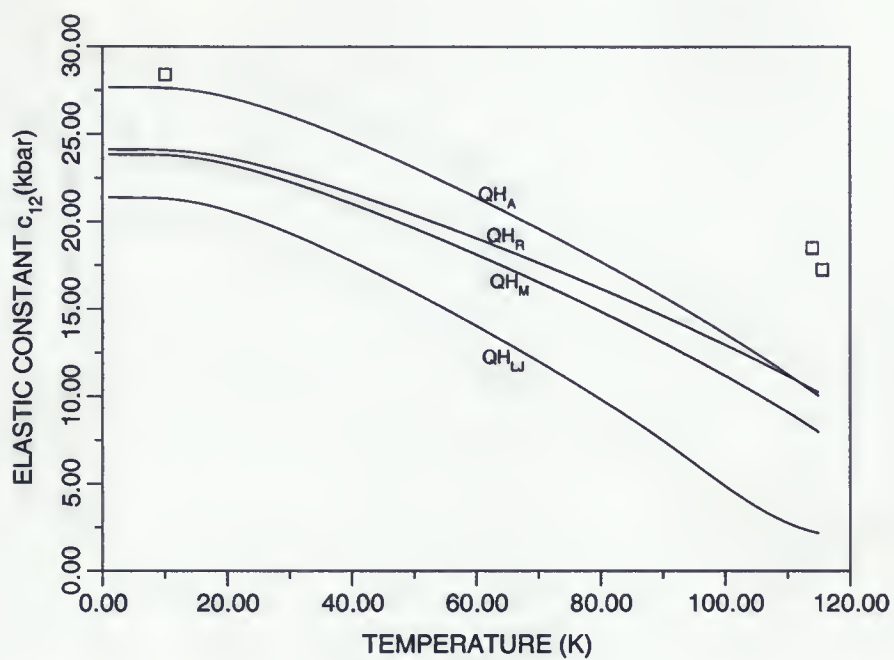


Figure 3.28: Elastic constant c_{12} via the long wavelength limit for Kr. \square are the experimental points from [31]. The labels for each line are defined in the text.

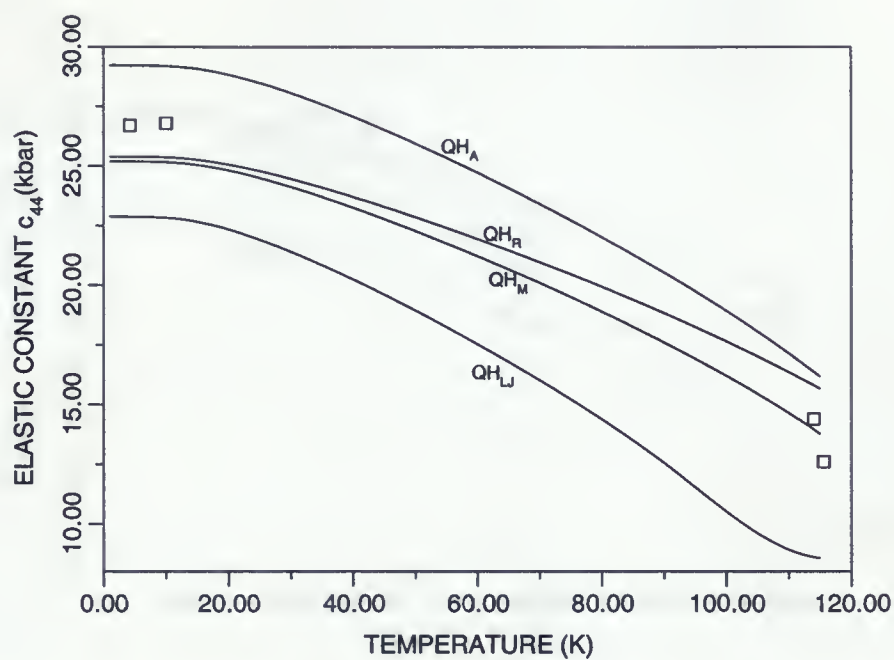


Figure 3.29: Elastic constant c_{44} via the long wavelength limit for Kr. \square are the experimental points from [31]. The labels for each line are defined in the text.

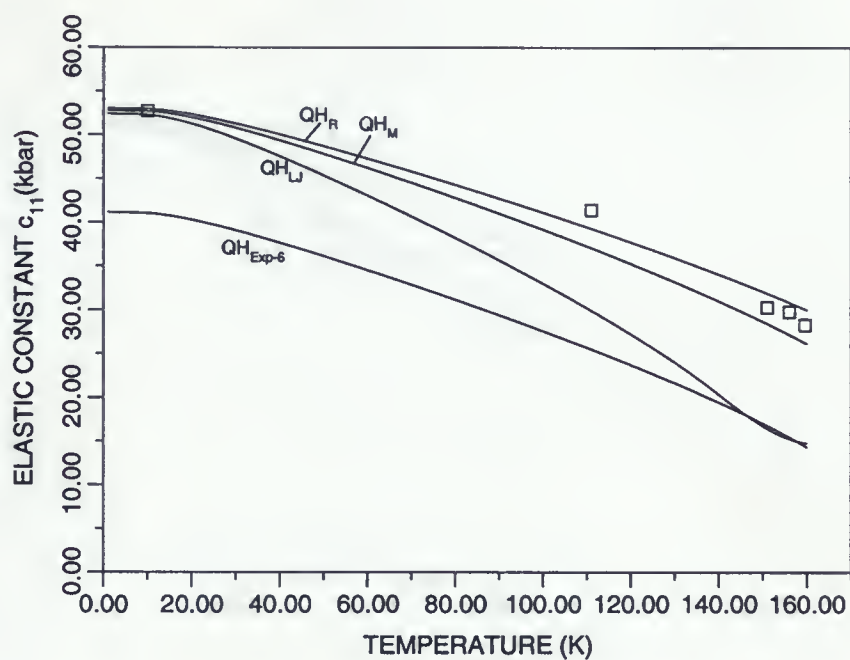


Figure 3.30: Elastic constant c_{11} via the long wavelength limit for Xe. \square are the experimental points from [31]. The labels for each line are defined in the text.

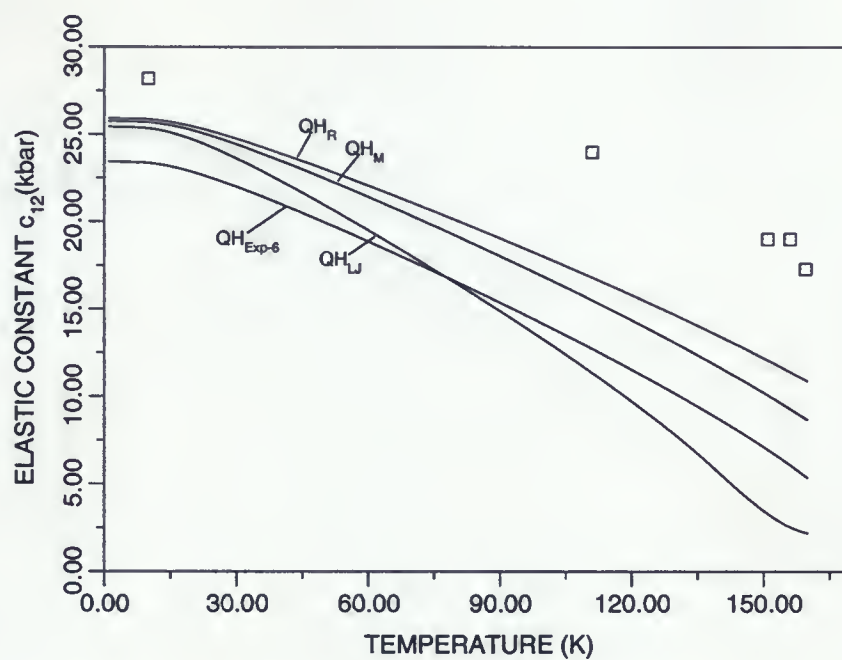


Figure 3.31: Elastic constant c_{12} via the long wavelength limit for Xe. \square are the experimental points from [31]. The labels for each line are defined in the text.

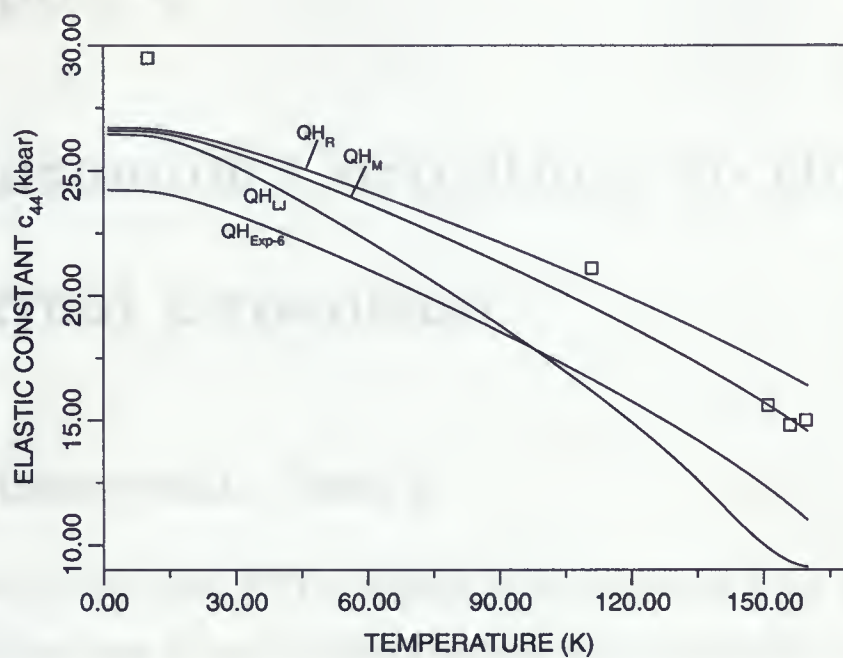


Figure 3.32: Elastic constant c_{44} via the long wavelength limit for Xe. \square are the experimental points from [31]. The labels for each line are defined in the text.

Chapter 4

Anharmonic Corrections to the Thermal Expansion

4.1 Anharmonic Theory

When perturbation theory (PT) is employed in the calculation of the Helmholtz function (F) of an anharmonic crystal, the various anharmonic contributions to F are obtained in the form of an infinite series [3]. This is due to the fact that the perturbation potential itself is in the form of an infinite series. So in the systematic application of PT in the calculation of F , whose minimization gives the thermodynamic properties, the number of terms to be retained in a given order of PT needs to be known. The Hamiltonian required for the enumeration of the various contributions to F to order λ^2 , is given by

$$H = H_0 + \lambda V_3 + \lambda^2 V_4 = H_0 + V, \quad (4.1)$$

where H_0 is the harmonic portion of H , λ is called the Van Hove perturbation expansion parameter, and this is defined as the ratio of a typical root-mean-square displacement and the nearest-neighbor distance. V_3 and V_4 are the cubic and quartic terms in the Taylor's expansion of the crystal potential energy. With the above H , F can then be evaluated from

$$F = -(1/\beta) \ln(Z), \quad (4.2)$$

where $\beta = 1/k_B T$ and

$$Z = \text{Tr}[\exp(-\beta H)]. \quad (4.3)$$

The Tr represents the trace of the operator $\exp(-\beta H)$. Since the operators H_0 and V in the above H do not commute with each other, the expansion of $\exp(-\beta H)$ can be carried out in the form of

$$\exp(-\beta H)S(\beta), \quad (4.4)$$

where $S(\beta)$ is an infinite series involving the various powers of V , the total perturbing potential in equation 4.1. These terms can be evaluated by the diagrammatic method. When the diagrammatic method is employed in the evaluation of F , the contributions can be grouped according to the powers of λ . For example, one finds two contributions of $O(\lambda^2)$.

In this work we incorporate the anharmonic corrections to $O(\lambda^2)$ using only the nearest neighbor contributions to the potential energy based on the work done by Shukla and MacDonald [4]. The anharmonic corrections are valid for the nearest neighbor interactions only, and for temperatures greater than θ_D .

The contributions to the free energy, F_0 , F_3 , and F_4 can be expressed in terms of derivatives of $\phi(r)$ and dimensionless Brillouin Zone (BZ) sums which are functions of a parameter a_1 and is defined by

$$a_1 = \frac{\phi'/r}{\phi'' - \phi'/r}. \quad (4.5)$$

There are two contributions to F_0 , given by $F_0^{(1)}$ and $F_0^{(2)}$, and two contributions to F_4 given by $F_4^{(1)}$ and $F_4^{(2)}$. The total free energy of the lattice is

$$F(r, T) = F_0^{(1)} + F_0^{(2)} + F_4^{(1)} + F_4^{(2)} + F_3 + U. \quad (4.6)$$

For the sake of clarity, both in calculation and in comparing with previous calculations, the total free energy containing N atoms is

$$\begin{aligned} F(r, T) = & 3N\{(k_B T)^{-1}F(1) + F(2) + k_B T F(3) + (k_B T)^2[F(4) + F(5)] \\ & - k_B T[\ln(k_B T) + 0.4288]\} + U. \end{aligned} \quad (4.7)$$

The various contributions to $F(r, T)$ defined as follows:

$$F_0^{(1)} = 3Nk_B T [F(3) - \ln(k_B T) - 0.4288] \quad (4.8)$$

and

$$F(3) = \frac{1}{2} \left[\ln \left(\frac{8\hbar^2 B}{M} \right) + f(a_1) \right]; \quad (4.9)$$

$$F_0^{(2)} = 3N(k_B T)^{-1} F(1) \quad (4.10)$$

and

$$F(1) = \frac{\hbar^2}{6M} B(1 + 3a_1); \quad (4.11)$$

$$F_4^{(1)} = 3N F(2) \quad (4.12)$$

and

$$F(2) = \frac{\hbar^2}{24MB} \left[DS_{2A}(a_1) + \frac{2C}{r} S_{2B}(a_1) + \frac{4B}{r^2} S_{2C}(a_1) \right]; \quad (4.13)$$

$$F_4^{(2)} = 3N(k_B T)^2 F(4) \quad (4.14)$$

and

$$F(4) = \frac{1}{192B^2} \left[DS_{4A}(a_1) + \frac{2C}{r} S_{4B}(a_1) + \frac{4B}{r^2} S_{4C}(a_1) \right]; \quad (4.15)$$

$$F_3 = 3N(k_B T)^2 F(5) \quad (4.16)$$

and

$$F(5) = -\frac{C^2}{9216B^3} \left[S_{3A}(a_1) + \frac{12B}{rC} S_{3B}(a_1) + \frac{4B^2}{r^2 C^2} S_{3C}(a_1) \right]; \quad (4.17)$$

and

$$U = \frac{N}{2} \sum_{i,j}^N \phi(r_{ij}), \quad (4.18)$$

where the sum is taken over $i \neq j$. For the nncf model,

$$U = 6N\phi(r). \quad (4.19)$$

The various symbols appearing in equations 4.7 to 4.18 are defined as follows: k_B is Boltzmann's constant, \hbar is Planck's constant divided by 2π , M is the atomic mass, r is the nearest-neighbor distance, and the operator D is given by

$$D = \frac{1}{r} \frac{d}{dr}. \quad (4.20)$$

$B(r)$, $C(r)$, and $D(r)$ are defined as

$$B(r) = r^2 D^2 \phi(r), \quad (4.21)$$

$$C(r) = r^3 D^3 \phi(r), \quad (4.22)$$

and

$$D(r) = r^4 D^4 \phi(r). \quad (4.23)$$

The functions $f(a_1)$, $S_{2A}(a_1)$, $S_{2B}(a_1)$, $S_{2C}(a_1)$, $S_{4A}(a_1)$, $S_{4B}(a_1)$, $S_{4C}(a_1)$, $S_{3A}(a_1)$, $S_{3B}(a_1)$, and $S_{3C}(a_1)$ are the BZ sums which depend on a_1 . The parameter a_1 itself enters the problem in the expression for the dynamical matrix in equation 2.29 which give the elements of the dynamical matrix and these determine the phonon frequencies ω . Shukla and MacDonald [4] computed the BZ sums in F_3 and $F_4^{(2)}$ for values of a_1 in the range $-0.1 \leq a_1 \leq 0.1$ in steps of 0.02. Table 4.1 give the least squares coefficients that reproduce the numerical values of the BZ sums to better than 1 part in 10^3 for the range defined above. The functions in table 4.1 are defined as

$$f(a_1) = \sum_{n=0}^6 b_n(a_1)^n, \quad (4.24)$$

and $S_{2A}(a_1)$ to $S_{3C}(a_1)$ are defined by

$$S_{\alpha\beta}(a_1) = \exp \left[\sum_{n=0}^6 b_n(a_1)^n \right]. \quad (4.25)$$

Table 4.1: Coefficients of the least-squares fit for the calculations of the BZ sums used in the study of anharmonic effects [4].

Function	b_0	b_1	b_2	b_3	b_4	b_5	b_6
$f(a_1)$	0.0000	3.5892	-6.6768	16.8293	-48.9623	197.3788	-689.6764
$S_{2A}(a_1)$	0.0000	-3.5929	8.5369	-27.6926	108.6641	-1219.9278	7250.4428
$S_{2B}(a_1)$	1.6667	-3.7867	9.2900	-30.4436	120.0002	-1390.1624	8342.2428
$S_{2C}(a_1)$	1.5010	-4.1647	10.6480	-35.2060	138.9856	-1660.1682	10058.5591
$S_{4A}(a_1)$	2.4849	-7.1856	17.0777	-55.4237	216.2252	-2437.4300	14571.7692
$S_{4B}(a_1)$	4.2057	-7.5530	18.4681	-60.4178	237.8025	-2743.1526	16445.6889
$S_{4C}(a_1)$	4.1707	-8.3623	21.4617	-71.0621	280.8543	-3373.1748	20463.4373
$S_{3A}(a_1)$	5.1507	-10.9028	26.4829	-87.0026	343.6693	-3870.2265	23007.1720
$S_{3B}(a_1)$	4.5251	-10.6448	25.5145	-83.9222	322.2881	-3553.1758	20747.0075
$S_{3C}(a_1)$	6.6127	-10.8787	26.6242	-87.0519	343.0085	-4357.7099	26894.3897

4.1.1 Results for the Anharmonic Corrections to the Thermal Expansion of the Isothermal and Adiabatic Bulk Moduli, and Specific Heats

Figures 4.1-4.10 depict the results of the thermodynamic properties for Kr, and Xe employing λ^2 anharmonic corrections to $F(a, T)$ defined by equation 3.6 for $T > \theta_D$. The labels λ^2 represent the anharmonic corrections to $F(a, T)$:

$$F_{\lambda^2}(a, T) = U_{static}(a) + F_H(a, T) + F_4^{(1)} + F_4^{(2)} + F_3. \quad (4.26)$$

The results for the Morse, Rydberg, and LJ calculations were already obtained by Shukla and Shanes [2] and are included in this work for the purpose of comparison with the other

potentials. The labels QH represent the quasi-harmonic calculations, and the labels λ^2 represent the anharmonic corrections to F . We notice that all the λ^2 results for a_T in figures 4.1 and 4.2 are lowered with respect to the QH results. This trend was also observed in the work by Shukla and Shanes [2]. It is interesting to note that the λ^4 results in the work by Shukla and Shanes tend to increase the results from λ^2 . From figures 4.3-4.10 the λ^2 results for B_T and B_S are increased, and the C_V and C_P results are decreased with respect to the QH results. Again, this trend was observed by Shukla and Shanes [2]. Furthermore, the λ^4 results for B_T and B_S tend to lower the λ^2 results, and increase the C_V and C_P results in the work by Shukla and Shanes [2].

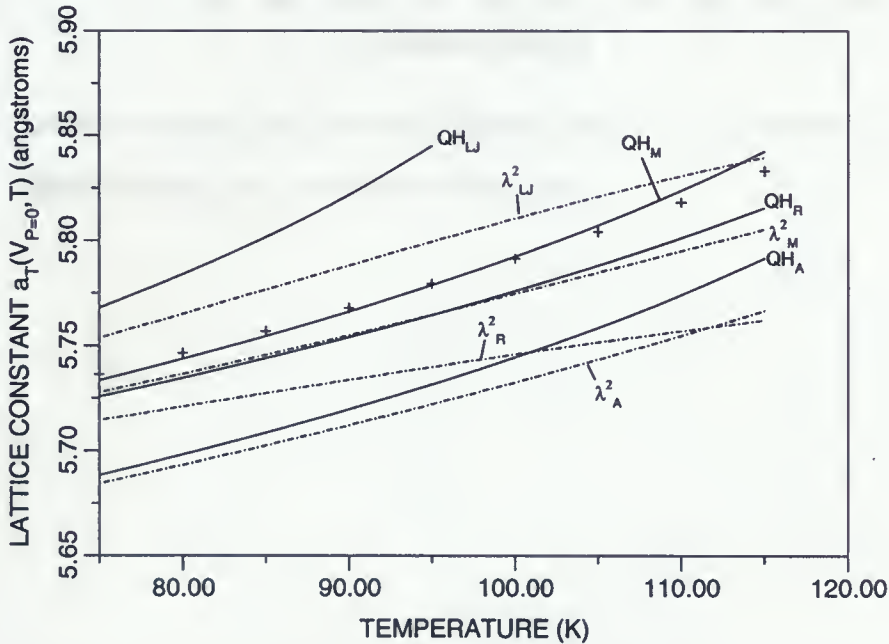


Figure 4.1: Lattice constant (a_T) at zero pressure for Kr. +, experimental points [31]; the labels for each line are defined in the text.

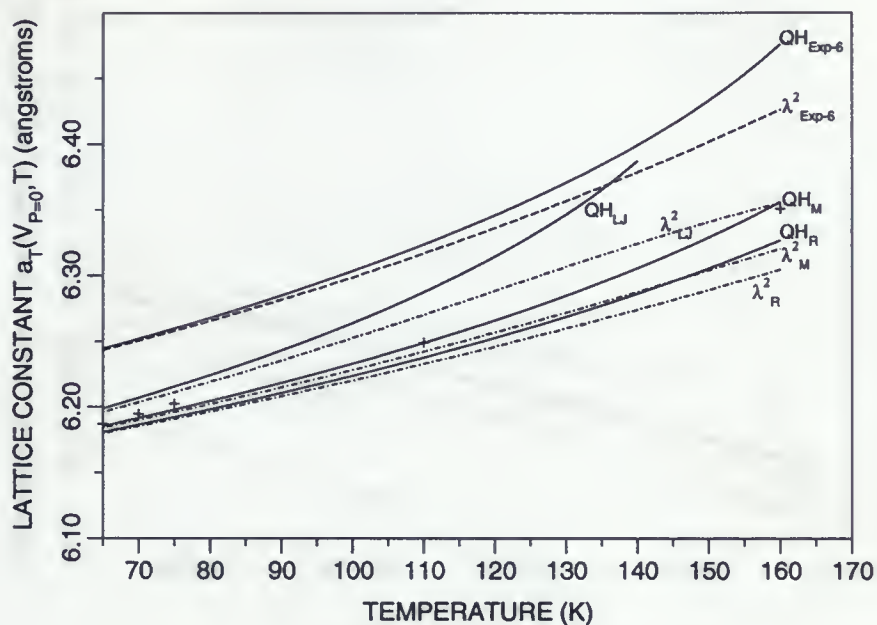


Figure 4.2: Lattice constant (a_T) at zero pressure for Xe. +, experimental points [31]; the labels for each line are defined in the text.

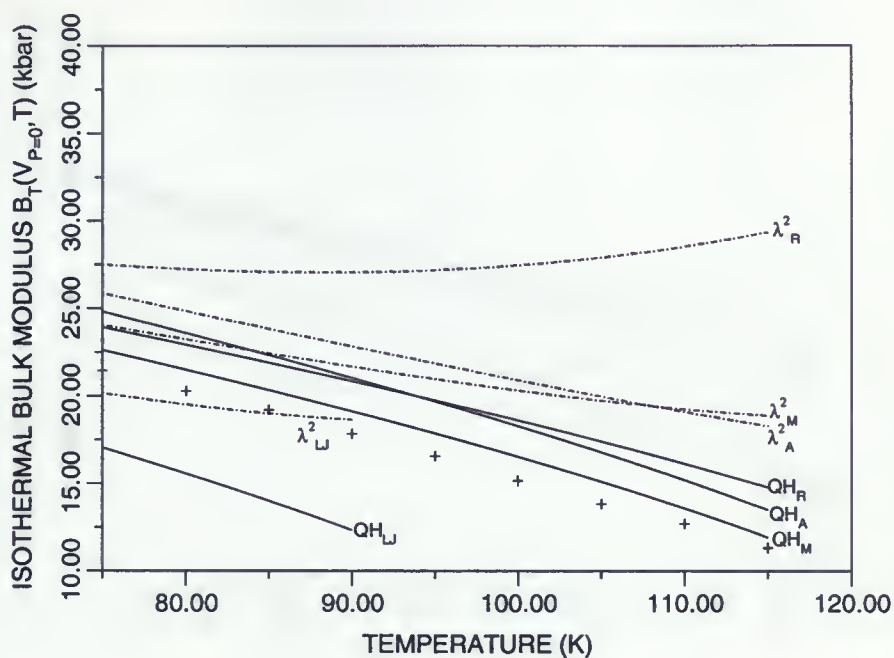


Figure 4.3: Isothermal bulk modulus (B_T) for Kr. +, experimental points [31]; the labels for each line are defined in the text.

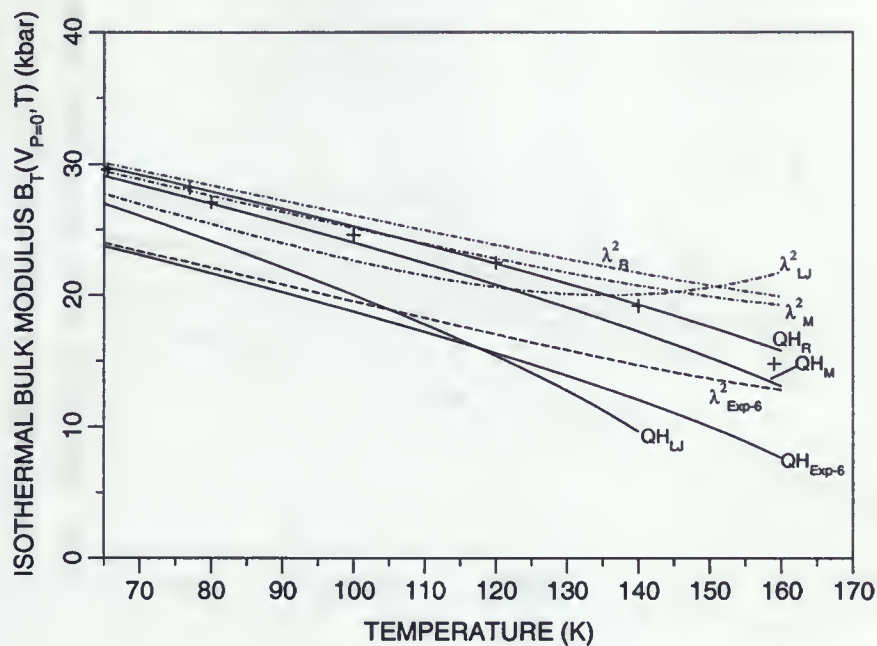


Figure 4.4: Isothermal bulk modulus (B_T) for Xe. +, experimental points [31]; the labels for each line are defined in the text.

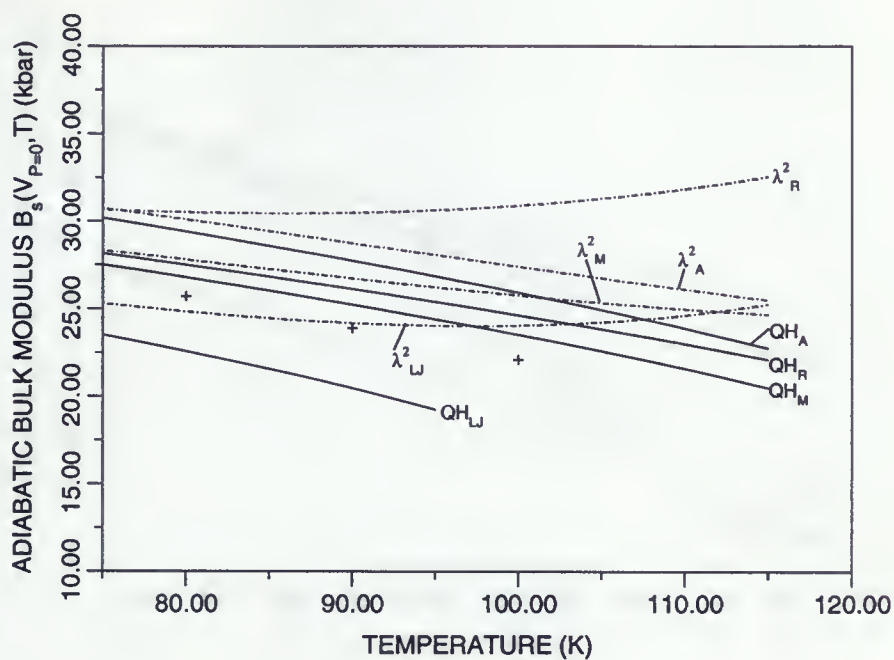


Figure 4.5: Adiabatic bulk modulus (B_s) for Kr. +, experimental points [31]; the labels for each line are defined in the text.

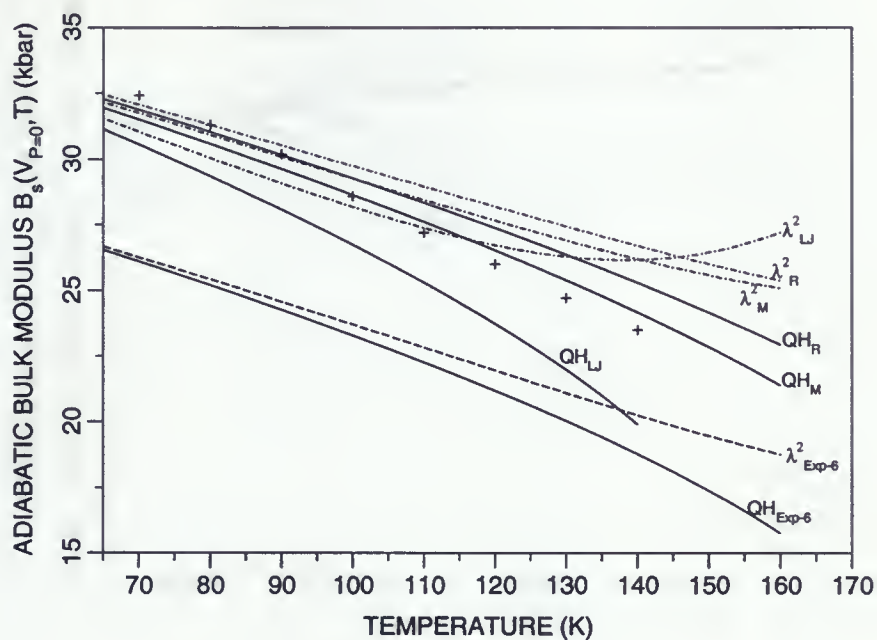


Figure 4.6: Adiabatic bulk modulus (B_s) for Xe. +, experimental points [31]; the labels for each line are defined in the text.

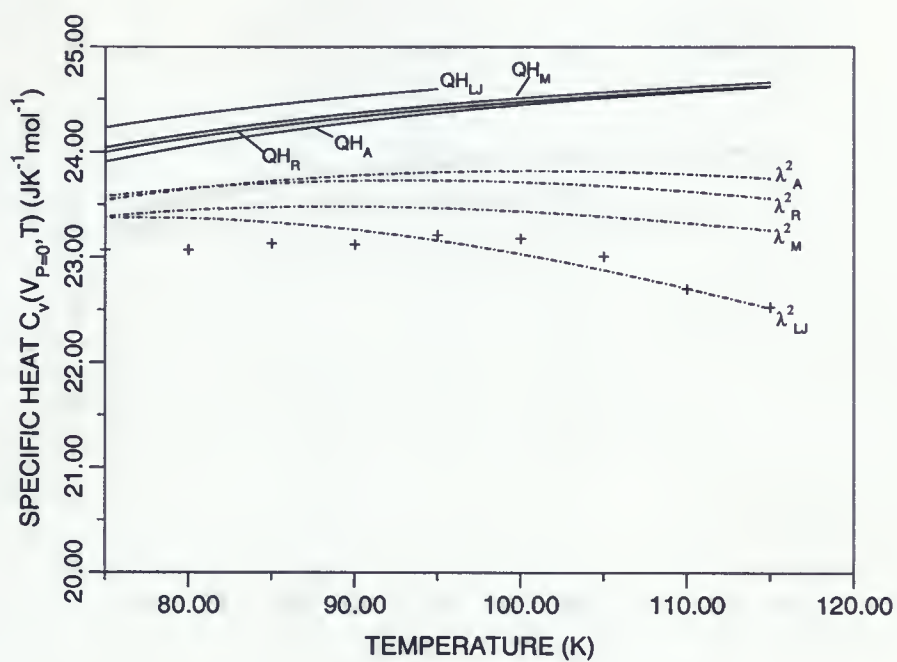


Figure 4.7: Specific heat at constant volume (C_V) for Kr. +, experimental points [33]; the labels for each line are defined in the text.

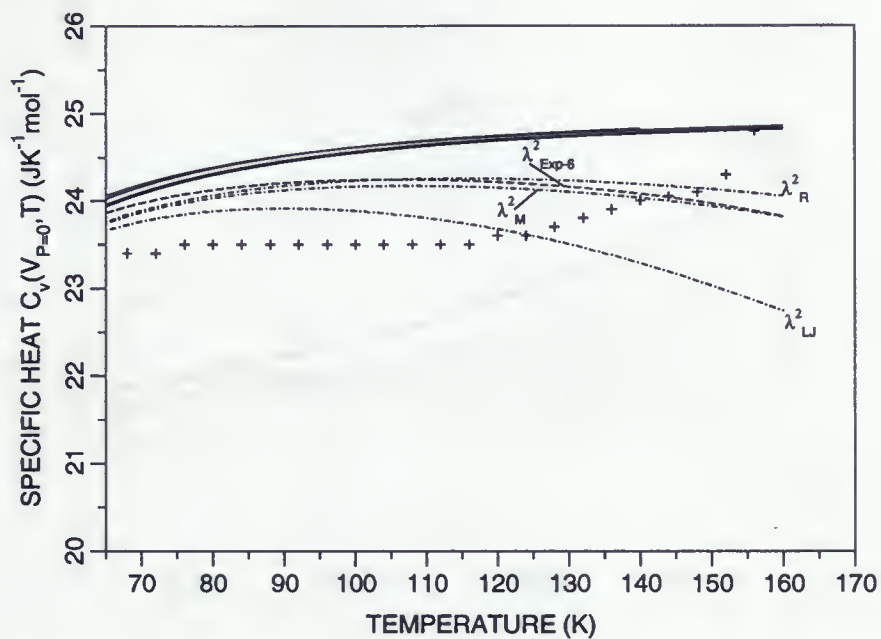


Figure 4.8: Specific heat at constant volume (C_V) for Xe. +, experimental points [34]; the labels for each line are defined in the text.

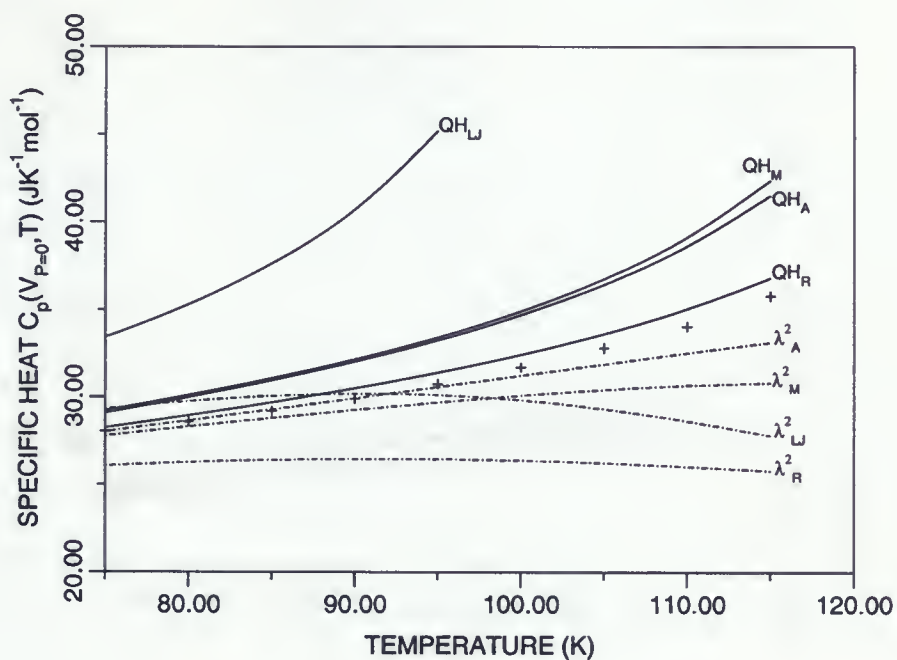


Figure 4.9: Specific heat at constant pressure (C_P) for Kr. +, experimental points [31]; the labels for each line are defined in the text.

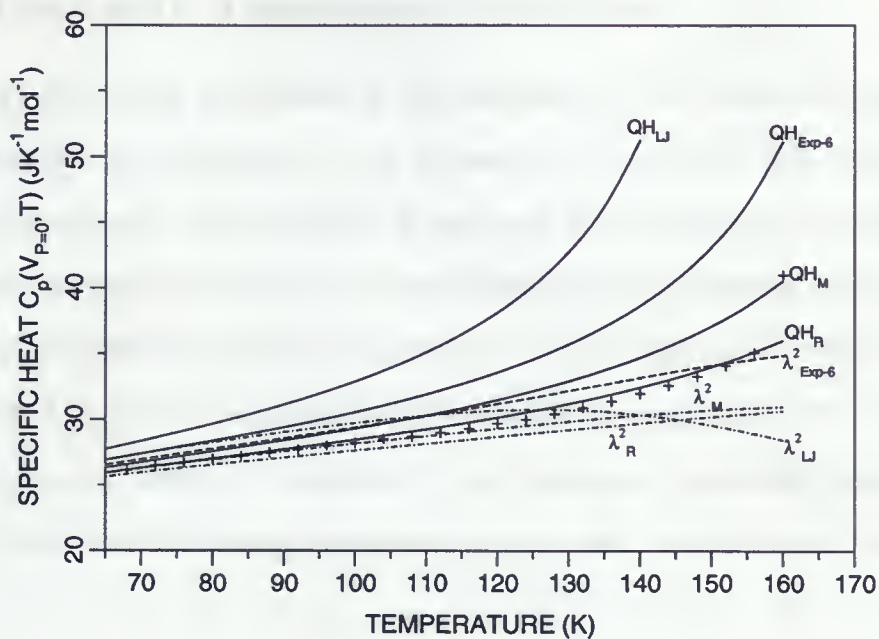


Figure 4.10: Specific heat at constant pressure (C_P) for Xe. +, experimental points [31]; the labels for each line are defined in the text.

4.1.2 Results for the Elastic Constants via the Long Wavelength Limit with Anharmonic Corrections

Figures 4.11-4.16 depict the results of the calculation of the elastic constants c_{11} , c_{12} , and c_{44} as a function of temperature T for Kr, and Xe. The labels QH represent the quasi-harmonic calculations, and the labels λ^2 represent the anharmonic corrections to F . The elastic constants were obtained via the minimization of the Helmholtz free energy at a given temperature T , solving for the lattice parameter a , and using these results in equation 3.13. From figures 4.11-4.16 we note that the λ^2 anharmonic corrections tend to increase the QH results for c_{11} , c_{12} , and c_{44} . In chapter 5, we calculated the percent errors of the elastic constants, with the anharmonic corrections, c_{11} , c_{12} , and c_{44} for Kr, and Xe.

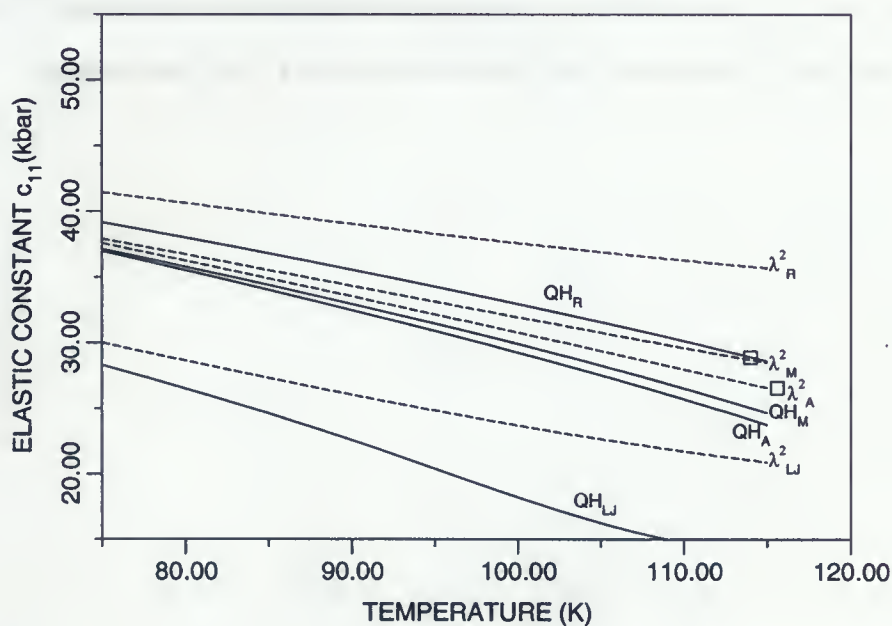


Figure 4.11: Elastic constant c_{11} via the long wavelength limit for Kr. \square are the experimental points from [31]. The labels for each line are defined in the text.

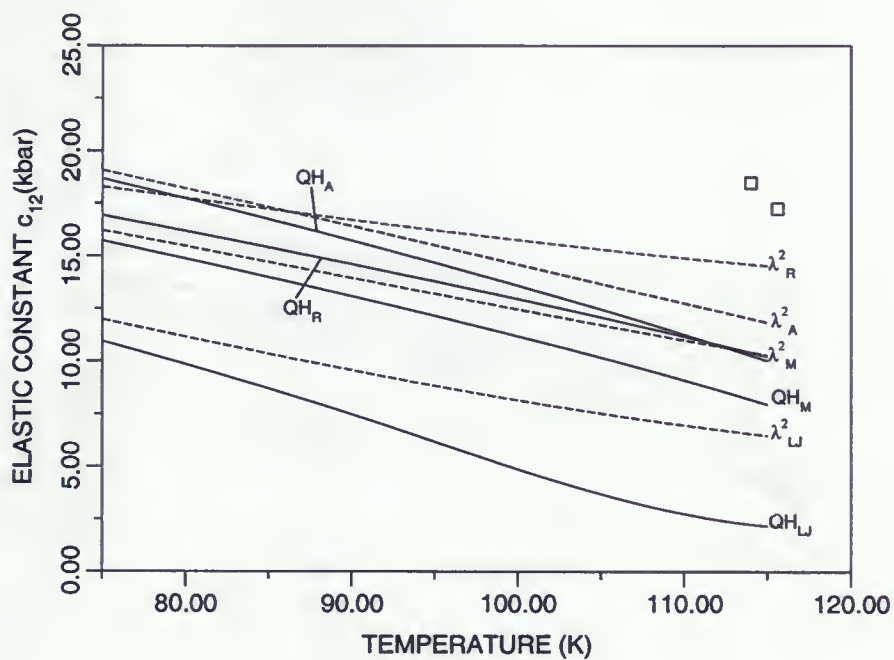


Figure 4.12: Elastic constant c_{12} via the long wavelength limit for Kr. \square are the experimental points from [31]. The labels for each line are defined in the text.

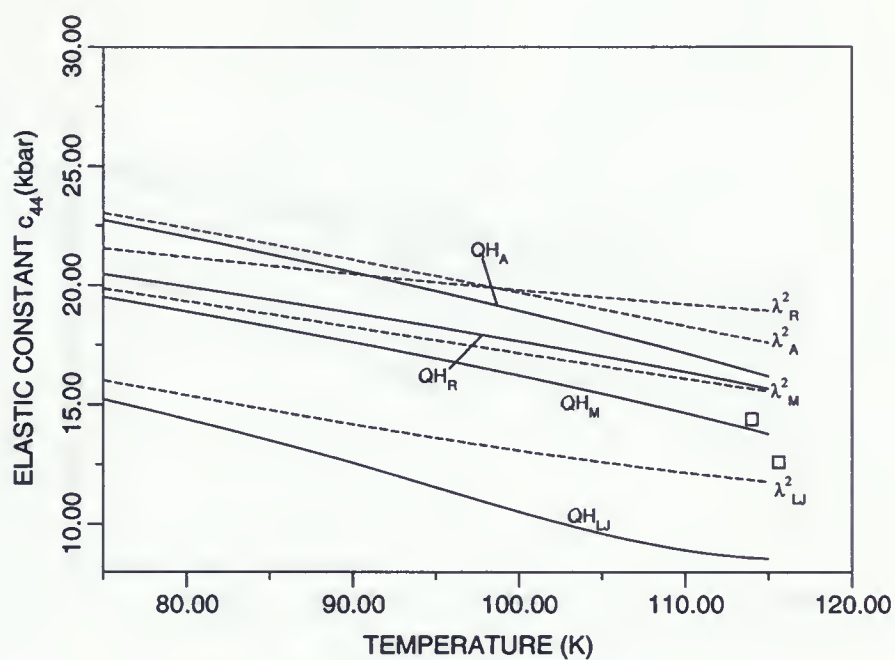


Figure 4.13: Elastic constant c_{44} via the long wavelength limit for Kr. \square are the experimental points from [31]. The labels for each line are defined in the text.

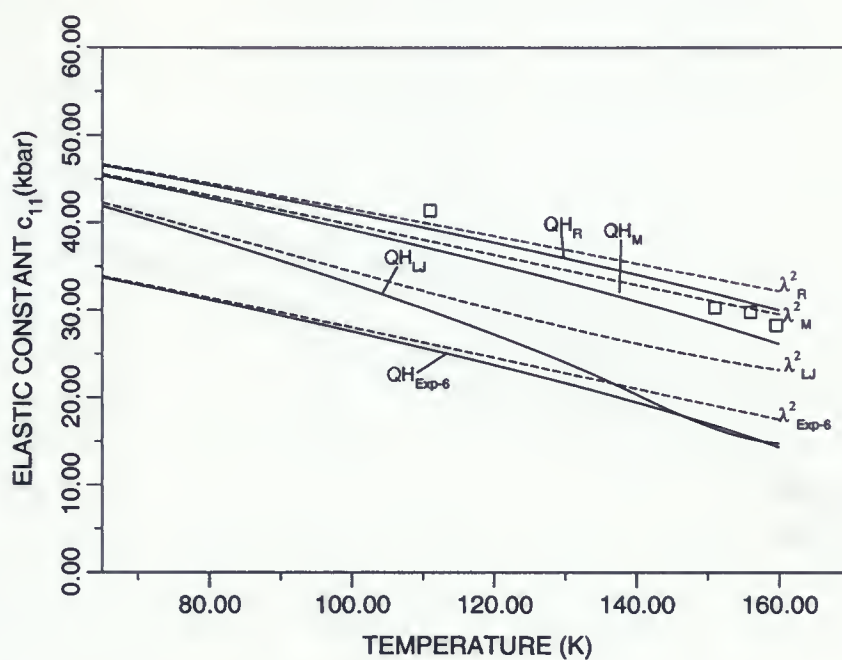


Figure 4.14: Elastic constant c_{11} via the long wavelength limit for Xe. \square are the experimental points from [31]. The labels for each line are defined in the text.

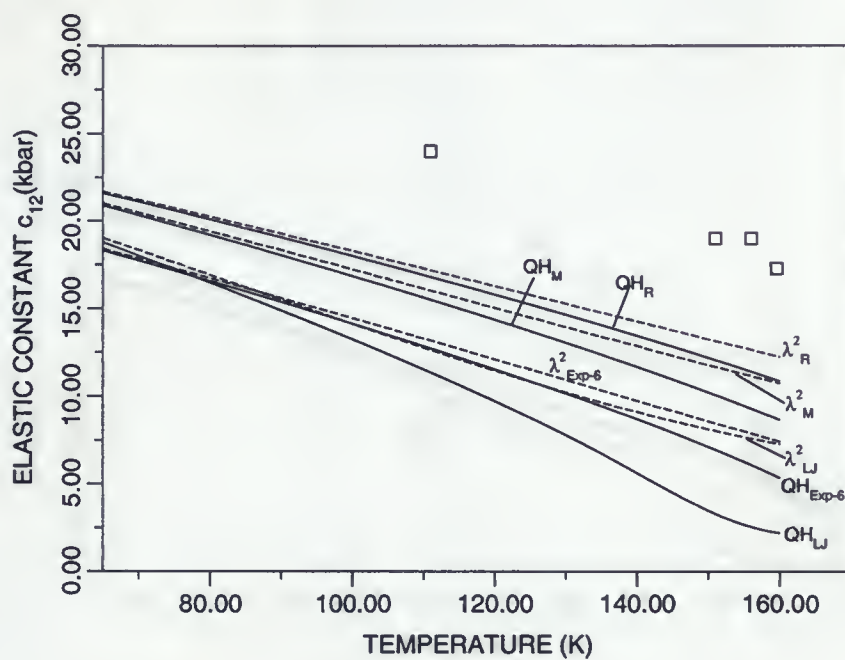


Figure 4.15: Elastic constant c_{12} via the long wavelength limit for Xe. \square are the experimental points from [31]. The labels for each line are defined in the text.

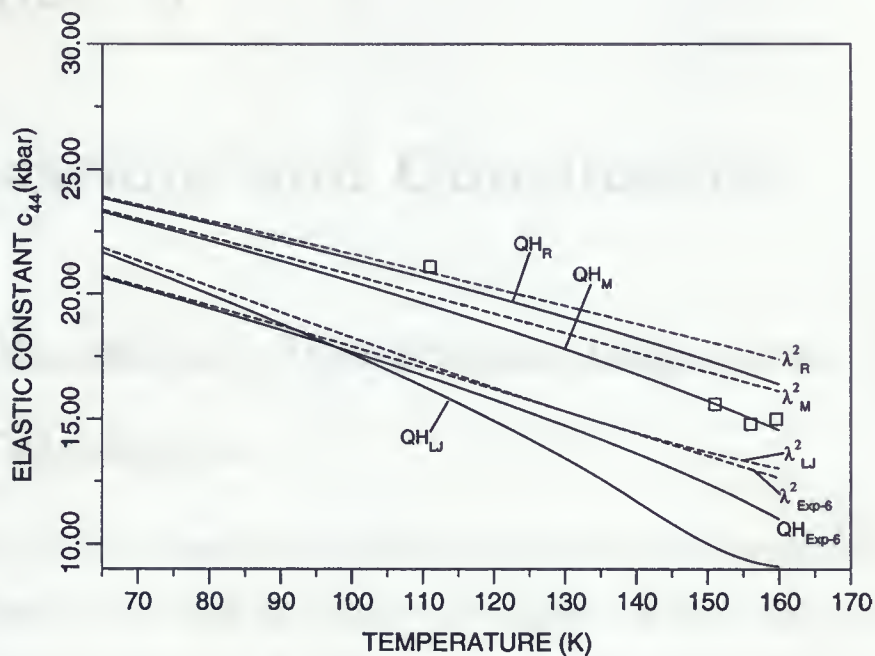


Figure 4.16: Elastic constant c_{44} via the long wavelength limit for Xe. \square are the experimental points from [31]. The labels for each line are defined in the text.

Chapter 5

Discussions and Conclusions

5.1 Discussions of the Phonon Dispersion Calculations

The results of phonon dispersion calculations as compared to the experimental values at the zone boundaries in the [100], and [111] in the principal symmetry directions for Ne, Ar, Kr, and Xe are given in table 5.1. We calculate the percentage error by taking the absolute value of the calculated value minus the experimental value, divided by the calculated value times 100.

Dispersion Results for Ne

From the calculated values in table 5.1 for Ne, we find that the ϕ_E potential, where the potential is based on combining *ab initio* quantum chemical calculations and molecular dynamics simulations, produced the best results in the [100]T, and [111]T principal symmetry directions at the zone boundaries, followed by the ϕ_{LJ} , where the potential parameters were obtained from fitting to the gas phase data, and the ϕ_A potential, where the parameters of the potential energy function were determined by fitting the function to the second virial coefficient data.

Dispersion Results for Ar

For the dispersion calculations of ^{36}Ar in the [100]L and [111]L symmetry directions, the ϕ_M potential, which is based on Møller-Plesset perturbation theory to fourth order (MP4) *ab initio* calculations, produced the best results at the zone boundary, followed by the ϕ_A potential, which is based on a combination of *ab initio* calculations and gas phase data, the ϕ_{Exp-6} , which is based on high-density fluid-perturbation theory and the $\phi_{Exp-6-8}$ potential, which is based on the self-consistent augmented-plane-wave statistical exchange (APW-X α) method. The ϕ_A potential produced the best results in the [100]T direction followed by, the ϕ_M , ϕ_{Exp-6} , ϕ_{LJ} , and $\phi_{Exp-6-8}$ pair potentials at the zone boundary respectively. The ϕ_A potential produced the best results in the [111]T direction followed by, the $\phi_{Exp-6-8}$, ϕ , ϕ_{LJ} , and $\phi_{Exp-6-8}$ pair potentials at the zone boundary respectively.

Dispersion Results for Kr

For the dispersion calculations of Kr in the [100]L, [100]T and [111]L symmetry directions, the ϕ_A potential, which is based on a combination of *ab initio* calculations and gas phase data, produced the best results at the zone boundary, followed by the ϕ_R potential, where the potential is based on fitting to the crystal properties, the ϕ_M potential, where the potential is based on fitting to the crystal properties, and the ϕ_{LJ} potential, where the potential is based on fitting to the crystal properties. The ϕ_{LJ} potential produced the best results in the [111]T direction followed by, the ϕ_M , ϕ_R , and ϕ_A pair potentials at the zone boundary respectively.

Dispersion Results for Xe

For the dispersion calculations of Xe in the [100]L, and [111]L symmetry directions, the ϕ_{Exp-6} potential, which is based on high-density fluid-perturbation theory, produced the best

results at the zone boundary, followed by the ϕ_R , which is based on fitting to the crystal properties, the ϕ_M potential, which is based on fitting to the crystal properties, and the ϕ_{LJ} potential, which is based on fitting to the crystal properties. The ϕ_R potential produced the best results in the [100]T direction at the zone boundary. The ϕ_M , and the ϕ_{LJ} produced identical results, and ϕ_{Exp-6} produced the worst results at the [100]T zone boundary. The ϕ_R , ϕ_M , and ϕ_{LJ} produced similar results followed by the ϕ_{Exp-6} pair potential at the [111]T zone boundary.

Table 5.1: Calculated percent errors for Ne, Ar, Kr, and Xe dispersion calculations at the zone boundaries in the [100], and [111] principal symmetry directions.

Element	Potential	% Error [100]L	% Error [100]T	% Error [111]L	% Error [111]T
Ne	$\phi_E^{(i)}$	no data	8.57	no data	17.3
	$\phi_{LJ}^{(ii)}$	no data	30.1	no data	40.4
	$\phi_A^{(iii)}$	no data	32.9	no data	45.8
Ar	$\phi_M^{(i)}$	0.601	5.22	1.44	13.9
	$\phi_A^{(iii)}$	2.28	4.55	3.95	5.79
	$\phi_{Exp-6}^{(iv)}$	4.21	11.6	5.51	22.7
	$\phi_{LJ}^{(v)}$	5.77	12.1	7.07	21.2
	$\phi_{Exp-6-8}^{(v)}$	26.2	14.1	28.1	9.32
Kr	$\phi_A^{(iii)}$	0.968	1.38	3.35	3.40
	$\phi_R^{(vi)}$	3.39	1.84	4.63	3.06
	$\phi_M^{(vi)}$	3.71	2.30	4.94	2.72
	$\phi_{LJ}^{(vi)}$	8.06	6.45	9.25	1.70
Xe	$\phi_{Exp-6}^{(iv)}$	1.87	8.73	2.44	20.5
	$\phi_R^{(vi)}$	3.93	3.70	3.75	1.57
	$\phi_M^{(vi)}$	4.12	3.97	3.94	1.57
	$\phi_{LJ}^{(vi)}$	4.12	3.97	4.13	1.57

⁽ⁱ⁾ Potential parameters obtained purely from *ab initio* calculations for dimers based on Møller-Plesset perturbation theory, ⁽ⁱⁱ⁾ Potential parameters obtained from fitting to the gas phase data, ⁽ⁱⁱⁱ⁾ Potential parameters obtained from *ab initio* (HF) calculations and from gas-phase data, ^(iv) Potential parameters obtained from high-density fluid-perturbation theory, ^(v) Potential parameters obtained from augmented-plane-wave (APW) calculations, and ^(vi) Potential parameters obtained from fitting to crystal properties.

5.2 Discussions of the Thermodynamic Properties of Ne, Ar, Kr, and Xe

We have studied the various thermodynamic properties for Ne, Ar, Kr, and Xe. The curves for the various equations-of-state calculations are presented in figures 3.1-4.10. To simplify the discussion of the thermodynamic results, we will discuss them in the order of the elements Ne, Ar, Kr, and Xe.

Thermodynamic Properties of Ne

From figure 3.1 we note that the a_T results for the QH_E calculations were too high as compared to the experimental results. The a_T results for the QH_A calculations did better than the QH_E results, but again, the calculations were too high as compared to the experimental results. The a_T results for the QH_{LJ} produced the best results and agreed very well with the experimental values up to around 14 K. From figures 3.5 and 3.9 the B_T and B_s results were too low for all three QH calculations; however, the QH_{LJ} results produced the closest results as compared to the experimental values. We find that from figures 3.13 and 3.17 the QH_A calculations produced the worst results for C_V and C_P followed by the QH_{LJ} and QH_E calculations respectively. All three QH calculations produced results that were too high at high temperatures as compared to the experimental values; however, the QH_{LJ} and QH_E results were close to experimental values for the temperatures between 8-12K. Generally, all three potentials did very poorly at reproducing the thermodynamic properties of Ne. The LJ potential, where the potential parameters were obtained from fitting to gas phase data, did a better job than the other two potentials.

Thermodynamic Properties of Ar

From figure 3.2 it is evident that the QH_M results for the Morse-type potential produced the best results overall, followed by the QH_A calculations, the QH_{LJ} calculations, the QH_{Exp-6} calculations, and the $QH_{Exp-6-8}$ calculations as compared to the experimental values. We find that from figure 3.6 that the QH_M results for the Morse-type potential produced the best results overall for B_T , followed by the QH_A calculations. At temperatures between 0-50K the $QH_{Exp-6-8}$, QH_{LJ} , and QH_{Exp-6} B_T calculations produced values that were too low compared to the experimental results. From figure 3.10 the QH_M results for the Morse-type potential produced best results overall for B_s but were still too high, followed by the QH_A calculations. At temperatures between 60-83K the $QH_{Exp-6-8}$, QH_{LJ} , and QH_{Exp-6} B_s calculations produced values that were too low compared to the experimental results. We find that from figures 3.14 and 3.18 all the QH calculations in the temperature range of 4-20K produced values that were too low for C_V and C_P . In the temperature range of 45-83K the QH calculations for the LJ, Exp-6-8, and the Exp-6 potentials produced values that were too high. The QH calculations of C_V and C_P for the Aziz and Morse-type potentials in the temperature range of 60-80K produced results that were too high. Overall, the Morse-type potential, where the potential parameters were obtained purely via *ab initio* calculations using Møller-Plesset perturbation theory to fourth order (MP4), did a better job than the other potentials.

Thermodynamic Properties of Kr

From figures 3.3 and 4.1 it is clear that the QH_M results for the Morse potential produced values that were closest to the experimentally determined lattice constant a_T followed by the QH_R results. The QH_{LJ} results were too high and the QH_A results were too low. At low T the QH_M , QH_R , and QH_{LJ} results all converged to the zero temperature lattice parameter.

All of the λ^2 calculations for a_T produced results that were lower than the QH results. The λ^2 results of a_T for $\theta_D < T < T_m$ (T_m is the melting temperature) were improved but were still too high as compared to the experimental values. The λ^2 results for the Morse, Rydberg, and Aziz potential were all lower than the experimental a_T values. From figures 3.7, 3.11, 4.3, and 4.5, it is clear that the QH_M results were closest to the experimental B_T and B_S values followed by the QH_R results. The B_T and B_S results for QH_A results were too high and the QH_{LJ} were too low for all T . From figures 4.3 and 4.5 we see that all of the λ^2 calculations for B_T and B_S were increased and bent upwards as T approached the melting temperature T_m . This was also observed in the study by Shukla and Shanes [2] and the study by Shukla and Hübschle [38]. We find that from figure 3.15 all the QH calculations in the temperature range of 4-25K produced values that were too low for C_V and too high in the temperature range 55-115K. From figure 4.7 we find that the λ^2 results of C_V for $\theta_D < T < T_m$ were improved but all of the curves bent down as T approached T_m . The λ_{LJ}^2 results were in good agreement with the experimental results. From figure 3.19, the QH_R results in the temperature range 50-115K produced values that were closest to the experimentally determined C_P values. Above 50K all the QH results were too high and below 25K the results were too low. From figure 4.9 we find that all of the λ^2 curves bent down as T approached T_m . The λ_A^2 results were in good agreement with the experimental values in the temperature range 75-100K. Overall, the Morse and Rydberg potentials, where the potential parameters were obtained by fitting to the crystal properties, did the best job of reproducing the thermodynamic properties of Kr.

Thermodynamic Properties of Xe

From figures 3.4 and 4.2 it is clear that the QH_M results for the Morse potential produced values that were closest to the experimentally determined lattice constant a_T followed by the QH_R results. The QH_{LJ} results were too high and the QH_A results were too low. At low T

the QH_M , QH_R , and QH_{LJ} results all converged to the zero temperature lattice parameter. All of the λ^2 calculations for a_T produced results that were lower than the QH results. The λ_{Exp-6}^2 and λ_{LJ}^2 results of a_T for $\theta_D < T < T_m$ (T_m is the melting temperature) were improved but were still too high as compared to the experimental values. The λ^2 results for the Morse, and Rydberg potential were all lower than the experimental a_T values. From figures 3.8, and 4.4, it is clear that the QH_R results were closest to the experimental B_T values followed by the QH_M results. From figures 3.12, and 4.6, it is clear that the QH_M results were closest to the experimental B_s values followed by the QH_R results. The B_T and B_s results for QH_{Exp-6} and QH_{LJ} were too low for all T . From figures 4.4 and 4.6 we see that all of the λ^2 calculations for B_T and B_s were increased and started bending upwards as T approached the melting temperature T_m . This was also observed in the study by Shukla and Shanes [2] and the study by Shukla and Hübschle [38]. We find that from figure 3.16 all the QH calculations in the temperature range of 4-20K produced values that were too low and too high in the temperature range 40-156K for C_V . From figures 4.8 we find that the λ^2 results of C_V for $\theta_D < T < T_m$ were improved slightly but all of the curves bent down as T approached T_m . From figure 3.20 the QH_R results in the temperature range 28-160K produced values that were closest to the experimentally determined C_P values. Above 40K all the QH_{LJ} and QH_{Exp-6} results were too high and below 24K the results were too low. The QH_M results were too high above 84K. From figures 4.10 we find that all of the λ^2 curves were lower than the QH curves and bent down as T approached T_m . The λ_M^2 results were in good agreement with the experimental values in the temperature range 65-120K. Again, overall the Morse and Rydberg potentials, where the potential parameters were obtained by fitting to the crystal properties, did the best job of reproducing the thermodynamic properties of Xe.

5.3 Elastic Constants Calculation Discussions via the Long Wavelength Limit

We have studied the temperature dependence of the elastic constants by employing the long wavelength limit relations for face-centered cubic crystals [26]. We first obtain the temperature dependant lattice constants from figures 3.1-3.4 and figures 4.1-4.2, and used these results in equation 3.13 to calculate the elastic constants c_{11} , c_{12} , and c_{44} for Ne, Ar, Kr, and Xe. The results of the calculated elastic constants as compared to the experimental values are given in table 5.2-5.16. At low T all three potentials did a very poor job at reproducing the elastic constants c_{11} , c_{12} and c_{44} for Ne. However, the Eggenberger potential produced the most favourable results. This result was also observed in the dispersion relations for Ne. This result is not surprising because the slopes of the dispersion curves for small \mathbf{k} are related to the elastic constants via the following relations. In the [100] direction,

$$\omega^2 \rho = c_{11} k^2, \quad (\text{longitudinal branch}) \quad (5.1)$$

and

$$\omega^2 \rho = c_{44} k^2, \quad (\text{transverse branch}) \quad (5.2)$$

where k is the wavevector, ω is the angular frequency, and ρ is the density. The elastic constant c_{11} is related to the slope of the longitudinal branch in the [100] direction, and c_{44} to the transverse branch of the dispersion curves. The elastic constant c_{12} can be obtained from the [110] direction. At high T all potentials did a very poor job at reproducing the elastic constants c_{11} , c_{12} and c_{44} for Ar. However, the Morse-type and Aziz potential produced the most favourable results. At low T the Rydberg and Aziz potential produced the best results. From figures 3.27 and 3.28 and tables 5.5-5.7 and 5.11-5.13 the QH_A for Kr produced the best results overall for c_{11} and c_{12} . From figure 3.29 the QH_M followed by the QH_R calculations produced the best results overall. At low T the QH_R , QH_M , and QH_{LJ} for Xe produced the

best results for c_{11} , c_{12} and c_{44} . At high T the QH_R and QH_M produced the best results for c_{11} , c_{12} and c_{44} . All the anharmonic corrections increased the QH values for Kr and Xe in figures 4.11-4.16 and tables 5.11-5.16.

Table 5.2: Calculated elastic constant c_{11} in the quasiharmonic (QH) approximation for Ne, and Ar. The labels are defined in the text.

Element	Potential	T(K)	c_{11} (kbar)	c_{11}^a (kbar)	% Error
Ne	$\phi_E^{(i)}$	5	7.48	16.6 ± 0.17	54.9
		6	7.47		54.7
	$\phi_{LJ}^{(ii)}$	5	6.82		58.9
		6	6.81		58.7
	$\phi_A^{(iii)}$	5	4.30		74.1
		6	4.27		74.1
Ar	$\phi_M^{(i)}$	82.3	18.5	23.8 ± 1.0	22.3
	$\phi_A^{(iii)}$	82.3	18.9		20.6
	$\phi_{Exp-6}^{(iv)}$	82.3	11.0		53.8
	$\phi_{LJ}^{(v)}$	82.3	6.32		73.4
	$\phi_{Exp-6-8}^{(v)}$	82.3	4.67		80.4

^a The experimental values from [31].

- (i) Potential parameters obtained purely from *ab initio* calculations for dimers based on Møller-Plesset perturbation theory.
- (ii) Potential parameters obtained from fitting to the gas phase data.
- (iii) Potential parameters obtained from *ab initio* (HF) calculations and from gas-phase data.
- (iv) Potential parameters obtained from high-density fluid-perturbation theory.
- (v) Potential parameters obtained from augmented-plane-wave (APW) calculations.

Table 5.3: Calculated elastic constant c_{12} in the QH approximation for Ne, and Ar. The labels are defined in the text.

Element	Potential	T(K)	c_{12} (kbar)	c_{12}^a (kbar)	% Error
Ne	$\phi_E^{(i)}$	5	2.68	8.55 ± 0.21	68.7
		6	2.68		70.3
	$\phi_{LJ}^{(ii)}$	5	2.42		71.7
		6	2.41		73.3
	$\phi_A^{(iii)}$	5	1.19		86.1
		6	1.17		87.0
Ar	$\phi_M^{(i)}$	82.3	7.71	15.6 ± 0.3	50.6
	$\phi_A^{(iii)}$	82.3	7.60		51.3
	$\phi_{Exp-6}^{(iv)}$	82.3	3.95		74.7
	$\phi_{LJ}^{(v)}$	82.3	0.81		94.8
	$\phi_{Exp-6-8}^{(v)}$	82.3	0.00		100

^a The experimental values from [31].

(i) Potential parameters obtained purely from *ab initio* calculations for dimers based on Møller-Plesset perturbation theory.

(ii) Potential parameters obtained from fitting to the gas phase data.

(iii) Potential parameters obtained from *ab initio* (HF) calculations and from gas-phase data.

(iv) Potential parameters obtained from high-density fluid-perturbation theory.

(v) Potential parameters obtained from augmented-plane-wave (APW) calculations.

Table 5.4: Calculated elastic constant c_{44} in the QH approximation for Ne, and Ar. The labels are defined in the text.

Element	Potential	T(K)	c_{44} (kbar)	c_{44}^a (kbar)	% Error
Ne	$\phi_E^{(i)}$	5	5.44	9.52 ± 0.05	42.9
		6	5.44		41.4
	$\phi_{LJ}^{(ii)}$	5	5.22		45.2
		6	5.22		43.8
	$\phi_A^{(iii)}$	5	3.94		58.6
		6	3.93		57.7
Ar	$\phi_M^{(i)}$	82.3	13.0	11.2 ± 0.3	16.1
	$\phi_A^{(iii)}$	82.3	13.2		17.9
	$\phi_{Exp-6}^{(iv)}$	82.3	8.62		23.0
	$\phi_{LJ}^{(v)}$	82.3	6.18		44.8
	$\phi_{Exp-6-8}^{(v)}$	82.3	5.20		53.6

^a The experimental values from [31].

(i) Potential parameters obtained purely from *ab initio* calculations for dimers based on Møller-Plesset perturbation theory.

(ii) Potential parameters obtained from fitting to the gas phase data.

(iii) Potential parameters obtained from *ab initio* (HF) calculations and from gas-phase data.

(iv) Potential parameters obtained from high-density fluid-perturbation theory.

(v) Potential parameters obtained from augmented-plane-wave (APW) calculations.

Table 5.5: Calculated elastic constant c_{11} in the QH approximation for Kr. The labels are defined in the text.

Element	Potential	T(K)	c_{11} (kbar)	c_{11}^a (kbar)	% Error
Kr	$\phi_A^{(i)}$	4.2	50.3	51.4 ± 3	2.14
		10	50.3	51.4 ± 0.5	2.14
		114	24.2	28.9 ± 0.4	16.3
		115.6	23.5	26.57 ± 0.28	11.6
	$\phi_M^{(ii)}$	4.2	49.7		3.31
		10	49.6		3.50
		114	25.0		13.5
		115.6	24.4		8.17
	$\phi_R^{(ii)}$	4.2	50.1		2.53
		10	50.1		2.53
		114	28.9		0.00
		115.6	28.4		6.89
	$\phi_{LJ}^{(ii)}$	4.2	45.0		12.5
		10	44.9		12.6
		114	14.0		51.6
		115.6	13.9		47.7

^a The experimental values from [31].

⁽ⁱ⁾ Potential parameters obtained from *ab initio* (HF) calculations and from gas-phase data.

⁽ⁱⁱ⁾ Potential parameters obtained from fitting to crystal properties.

Table 5.6: Calculated elastic constant c_{12} in the QH approximation for Kr. The labels are defined in the text.

Element	Potential	T(K)	c_{12} (kbar)	c_{12}^a (kbar)	% Error
Kr	$\phi_A^{(i)}$	4.2	27.7	no data	
		10	27.6	28.4 ± 0.6	2.82
		114	10.3	18.5 ± 0.4	44.3
		115.6	9.88	17.25 ± 0.20	42.7
	$\phi_M^{(ii)}$	4.2	23.8		
		10	23.8		16.2
		114	8.20		55.7
		115.6	7.81		54.7
	$\phi_R^{(ii)}$	4.2	24.1		
		10	24.1		15.1
		114	10.4		43.8
		115.6	10.1		41.4
	$\phi_{LJ}^{(ii)}$	4.2	21.4		
		10	21.3		25.0
		114	2.25		87.8
		115.6	2.13		87.7

^a The experimental values from [31].

(i) Potential parameters obtained from *ab initio* (HF) calculations and from gas-phase data.

(ii) Potential parameters obtained from fitting to crystal properties.

Table 5.7: Calculated elastic constant c_{44} in the QH approximation for Kr. The labels are defined in the text.

Element	Potential	T(K)	c_{44} (kbar)	c_{44}^a (kbar)	% Error
Kr	$\phi_A^{(i)}$	4.2	29.2	26.7 ± 2	9.36
		10	29.2	26.8 ± 0.3	8.96
		114	16.4	14.4 ± 0.1	13.9
		115.6	16.1	12.61 ± 0.15	27.7
	$\phi_M^{(ii)}$	4.2	25.2		5.62
		10	25.2		5.97
		114	14.0		2.78
		115.6	13.7		8.64
	$\phi_R^{(ii)}$	4.2	25.4		4.87
		10	25.4		5.22
		114	15.8		9.72
		115.6	15.6		23.7
	$\phi_{LJ}^{(ii)}$	4.2	22.9		14.2
		10	22.8		14.9
		114	8.61		40.2
		115.6	8.55		32.2

^a The experimental values from [31].

⁽ⁱ⁾ Potential parameters obtained from *ab initio* (HF) calculations and from gas-phase data.

⁽ⁱⁱ⁾ Potential parameters obtained from fitting to crystal properties.

Table 5.8: Calculated elastic constant c_{11} in the QH approximation for Xe. The labels are defined in the text.

Element	Potential	T(K)	c_{11} (kbar)	c_{11}^a (kbar)	% Error
Xe	$\phi_{Exp-6}^{(i)}$	10	41.0	52.7 ± 0.9	22.2
		111	25.5	41.4 ± 0.6	38.4
		151	16.8	30.3 ± 0.5	44.6
		156	15.5	29.8 ± 0.5	48.0
		159.6	14.5	28.3 ± 0.5	48.8
	$\phi_M^{(ii)}$	10	52.7		0.00
		111	37.1		10.4
		151	28.5		5.94
		156	27.2		8.72
		159.6	26.3		7.07
	$\phi_R^{(ii)}$	10	52.9		0.38
		111	39.3		5.07
		151	31.9		5.28
		156	30.9		3.69
		159.6	30.1		6.36
	$\phi_{LJ}^{(ii)}$	10	52.3		0.76
		111	29.9		27.8
		151	16.5		45.5
		156	15.3		48.7
		159.6	14.8		47.7

^a The experimental values from [31].

⁽ⁱ⁾ Potential parameters obtained from high-density fluid-perturbation theory.

⁽ⁱⁱ⁾ Potential parameters obtained from fitting to crystal properties.

Table 5.9: Calculated elastic constant c_{12} in the QH approximation for Xe. The labels are defined in the text.

Element	Potential	T(K)	c_{12} (kbar)	c_{12}^a (kbar)	% Error
Xe	$\phi_{Exp-6}^{(i)}$	10	23.3	28.2 ± 0.8	17.4
		111	12.7	24.0 ± 0.6	47.1
		151	6.96	19.0 ± 0.4	63.4
		156	6.09	19.0 ± 0.4	67.9
		159.6	5.43	17.3 ± 0.5	68.6
	$\phi_M^{(ii)}$	10	25.7		8.87
		111	15.5		35.4
		151	10.1		46.8
		156	9.31		51.0
		159.6	8.73		49.5
	$\phi_R^{(ii)}$	10	25.9		8.16
		111	16.8		30.0
		151	12.1		36.3
		156	11.4		40.0
		159.6	10.9		37.0
	$\phi_{LJ}^{(ii)}$	10	25.3		10.3
		111	11.4		52.5
		151	3.30		82.6
		156	2.55		86.6
		159.6	2.23		87.1

^a The experimental values from [31].

(i) Potential parameters obtained from high-density fluid-perturbation theory.

(ii) Potential parameters obtained from fitting to crystal properties.

Table 5.10: Calculated elastic constant c_{44} in the QH approximation for Xe. The labels are defined in the text.

Element	Potential	T(K)	c_{44} (kbar)	c_{44}^a (kbar)	% Error
Xe	$\phi_{Exp-6}^{(i)}$	10	24.2	29.5 ± 0.4	18.0
		111	16.6	21.1 ± 0.4	21.3
		151	12.3	15.6 ± 0.4	21.2
		156	11.6	14.8 ± 0.4	21.6
		159.6	11.1	15.0 ± 0.2	26.0
	$\phi_M^{(ii)}$	10	26.6		9.83
		111	19.5		7.58
		151	15.6		0.00
		156	15.0		1.35
		159.6	14.6		2.67
	$\phi_R^{(ii)}$	10	26.7		9.49
		111	20.6		2.37
		151	17.2		10.3
		156	16.8		13.5
		159.6	16.4		9.33
	$\phi_{LJ}^{(ii)}$	10	26.4		10.5
		111	16.2		23.2
		151	9.88		36.7
		156	9.33		37.0
		159.6	9.13		39.1

^a The experimental values from [31].

(i) Potential parameters obtained from high-density fluid-perturbation theory.

(ii) Potential parameters obtained from fitting to crystal properties.

Table 5.11: Calculated elastic constant c_{11} with the λ^2 anharmonic corrections for Kr. The labels are defined in the text.

Element	Potential	T(K)	c_{11} (kbar)	c_{11}^a (kbar)	% Error
Kr	$\phi_A^{(i)}$	114	26.9	28.9 ± 0.4	6.92
		115.6	26.4		0.64
	$\phi_M^{(ii)}$	114	28.7	26.57 ± 0.28	0.69
		115.6	28.4		6.89
	$\phi_R^{(ii)}$	114	35.8	26.57 ± 0.28	23.9
		115.6	35.6		34.0
	$\phi_{LJ}^{(ii)}$	114	21.1	26.57 ± 0.28	27.0
		115.6	20.8		21.7

^a The experimental values from [31].

(i) Potential parameters obtained from *ab initio* (HF) calculations and from gas-phase data.

(ii) Potential parameters obtained from fitting to crystal properties.

Table 5.12: Calculated elastic constant c_{12} with the λ^2 anharmonic corrections for Kr. The labels are defined in the text.

Element	Potential	T(K)	c_{12} (kbar)	c_{12}^a (kbar)	% Error
Kr	$\phi_A^{(i)}$	114	12.0	18.5 ± 0.4	35.1
		115.6	11.7		32.2
	$\phi_M^{(ii)}$	114	10.4	17.25 ± 0.20	43.8
		115.6	10.2		40.9
	$\phi_R^{(ii)}$	114	14.6	17.25 ± 0.20	21.1
		115.6	14.5		15.9
	$\phi_{LJ}^{(ii)}$	114	6.57	17.25 ± 0.20	64.5
		115.6	6.42		62.8

^a The experimental values from [31].

⁽ⁱ⁾ Potential parameters obtained from *ab initio* (HF) calculations and from gas-phase data.

⁽ⁱⁱ⁾ Potential parameters obtained from fitting to crystal properties.

Table 5.13: Calculated elastic constant c_{44} with the λ^2 anharmonic corrections for Kr. The labels are defined in the text.

Element	Potential	T(K)	c_{44} (kbar)	c_{44}^a (kbar)	% Error
Kr	$\phi_A^{(i)}$	114	17.7	14.4 ± 0.1	22.9
		115.6	17.5	12.61 ± 0.15	38.8
	$\phi_M^{(ii)}$	114	15.7		9.03
		115.6	15.5		22.9
	$\phi_R^{(ii)}$	114	19.0		31.9
		115.6	18.9		49.9
	$\phi_{LJ}^{(ii)}$	114	11.9		17.4
		115.6	11.7		7.22

^a The experimental values from [31].

⁽ⁱ⁾ Potential parameters obtained from *ab initio* (HF) calculations and from gas-phase data.

⁽ⁱⁱ⁾ Potential parameters obtained from fitting to crystal properties.

Table 5.14: Calculated elastic constant c_{11} with the λ^2 anharmonic corrections for Xe. The labels are defined in the text.

Element	Potential	T(K)	c_{11} (kbar)	c_{11}^a (kbar)	% Error
Xe	$\phi_{Exp-6}^{(i)}$	111	26.2	41.4 ± 0.6	36.7
		151	19.1	30.3 ± 0.5	37.0
		156	18.2	29.8 ± 0.5	38.9
		159.6	17.6	28.3 ± 0.5	37.8
	$\phi_M^{(ii)}$	111	37.9		8.45
		151	31.0		2.31
		156	30.2		1.34
		159.6	29.6		4.59
	$\phi_R^{(ii)}$	111	39.9		3.62
		151	33.6		10.9
		156	32.8		10.1
		159.6	32.3		14.1
	$\phi_{LJ}^{(ii)}$	111	32.0		22.7
		151	24.4		19.5
		156	23.7		20.5
		159.6	23.2		18.0

^a The experimental values from [31].

⁽ⁱ⁾ Potential parameters obtained from high-density fluid-perturbation theory.

⁽ⁱⁱ⁾ Potential parameters obtained from fitting to crystal properties.

Table 5.15: Calculated elastic constant c_{12} with the λ^2 anharmonic corrections for Xe. The labels are defined in the text.

Element	Potential	T(K)	c_{12} (kbar)	c_{12}^a (kbar)	% Error
Xe	$\phi_{Exp-6}^{(i)}$	111	13.2	24.0 ± 0.6	45.0
		151	8.46	19.0 ± 0.4	55.5
		156	7.88	19.0 ± 0.4	58.5
		159.6	7.47	17.3 ± 0.5	56.8
	$\phi_M^{(ii)}$	111	16.0		33.3
		151	11.7		38.4
		156	11.2		41.1
		159.6	10.8		37.6
	$\phi_R^{(ii)}$	111	17.2		28.3
		151	13.2		30.5
		156	12.7		33.2
		159.6	12.3		28.9
	$\phi_{LJ}^{(ii)}$	111	12.6		47.5
		151	8.03		57.7
		156	7.60		60.0
		159.6	7.31		57.7

^a The experimental values from [31].

(i) Potential parameters obtained from high-density fluid-perturbation theory.

(ii) Potential parameters obtained from fitting to crystal properties.

Table 5.16: Calculated elastic constant c_{44} with the λ^2 anharmonic corrections for Xe. The labels are defined in the text.

Element	Potential	T(K)	c_{44} (kbar)	c_{44}^a (kbar)	% Error
Xe	$\phi_{Exp-6}^{(i)}$	111	17.0	21.1 ± 0.4	19.4
		151	13.4	15.6 ± 0.4	14.1
		156	13.0	14.8 ± 0.4	12.2
		159.6	12.7	15.0 ± 0.2	15.3
	$\phi_M^{(ii)}$	111	19.9		5.69
		151	16.8		7.69
		156	16.4		10.8
		159.6	16.1		7.33
	$\phi_R^{(ii)}$	111	20.9		0.95
		151	18.0		15.4
		156	17.7		19.6
		159.6	17.4		16.0
	$\phi_{LJ}^{(ii)}$	111	17.1		19.0
		151	13.6		12.8
		156	13.3		10.1
		159.6	13.0		13.3

^a The experimental values from [31].

(i) Potential parameters obtained from high-density fluid-perturbation theory.

(ii) Potential parameters obtained from fitting to crystal properties.

No single type of potential is found to fare better than the rest for all the properties studied and for all the rare gas solids. For the heavier solids, namely Kr and Xe, potentials based on fitting to the crystal properties (the 0-K sublimation energy, the 0-K equilibrium lattice constant, and the 0-K isothermal bulk modulus) yield better results for the thermodynamic properties and the elastic (shear) constants, but not for the phonon dispersion curves. For these two solids, the Aziz potential for Kr, which is based on a combination of an *ab initio* calculations and fitting to gas phase data, and the Exponential-6 potential for Xe, which is based on high-density fluid-perturbation theory, provide better agreement with the inelastic neutron scattering experiments. For Ar, the Morse-type potential which is based on Møller-Plesset perturbation theory to fourth order (MP4) *ab initio* calculations, yielded the best results for the thermodynamic properties, elastic (shear) constants, and the phonon dispersion curves. For Ne, the LJ potential which is based on fitting to the gas phase data yielded the best results for the thermodynamic properties. The Eggenberger potential for Ne, where the potential is based on combining *ab initio* quantum chemical calculations and molecular dynamics simulations, produced the best results for the elastic (shear) constants, and the phonon dispersion curves.

In short, potentials based on fitting to the crystal properties may have some advantage, particularly for Kr and Xe, in terms of reproducing the thermodynamic properties over an extended range of temperatures, but agreement with the phonon frequencies with the measured values is not guaranteed.

Bibliography

- [1] G. K. Horton. *American Journal of Physics*, **36**, 2, 93-119 (1968).
- [2] R. C. Shukla and F. Shanes. *Phys. Rev. B*, **32**, 4, (1984).
- [3] R. C. Shukla, S. K. Bose, and R. F. Delogu. *Phys. Rev. B*, **45**, 22, (1991).
- [4] R. C. Shukla and R. A. MacDonald. *High Temperatures - High Pressures*, **12**, 12, (1980).
- [5] Richard J. Sadus. *Molecular Simulation of Fluids*. Elsevier, Amsterdam-New York, 1999.
- [6] M. V. Bobetic and J. A. Barker. *Phys. Rev. B*, **2**, 10 (1970).
- [7] M. V. Bobetic, J. A. Barker, and M. L. Klein. *Phys. Rev. B*, **5**, 8, (1972).
- [8] J. A. Barker, M. L. Klein, and M. V. Bobetic. *IBM J. Res. Develop.*, **20**, 222, (1976).
- [9] B. M. Axilrod and E. Teller. *J. Chem. Phys.*, **11**, 299-300, (1943).
- [10] Micheal P. Marder. *Condensed Matter Physics*. Wiley-Interscience, New York, 2000.
- [11] C. Kittel. *Introduction to Solid State Physics*. John Wiley and Sons, Inc., New York, 1996.
- [12] Neil W. Ashcroft and N. David Mermin. *Solid state physics*. Brooks/Cole, Stamford, CT, 1976.

-
- [13] R. E. Eggenberger, Stefan Gerber, Hanspeter Huber, and Marc Welker. *Mol. Phys.*, **82**, 4, (1994).
- [14] R. A. Aziz, William J. Meath, and A. R. Allnatt. *Chem. Phys.*, **78**, 295-309 (1983).
- [15] *Annual Reviews of Computational Physics IX*. Edited by Dietrich Stauffer. World Scientific, Singapore-New Jersey-London-Hong Kong, 2001.
- [16] R. A. Aziz and H. H. Chen. *J. Chem. Phys.*, **67**, 12 (1977).
- [17] David E. Woon. *Chem. Phys. Lett.*, **204**, 1,2 (1993).
- [18] M. Ross, W. Nellis, and A. Mitchell. *Chem. Phys. Lett.*, **68**, 2,3, (1979).
- [19] Marvin Ross. *J. Chem. Phys.*, **71**, 4, (1979).
- [20] S. B. Trickey and Frank. W. Averill. *Phys. Rev. B*, **8**, 10, (1973).
- [21] Ronald A. Aziz. *Mol. Phys.*, **38**, 1 (1979).
- [22] M. Ross and A. K. McMahan. *Phys. Rev. B*, **21**, 4, (1980).
- [23] E. W. Montroll A. A. Maradudin and G. H. Weiss. *Theory of lattice dynamics in the harmonic approximation, Solid state physics, Supplement 3*. Academic Press, New York, 1963.
- [24] Max Born and Kun Huang. *Dynamical theory of crystal lattices*. Oxford: Clarendon Press, Oxford, 1962.
- [25] Ramesh Chandra Shukla. *J. Chem. Phys.*, **45**, 11, (1966).
- [26] G. L. Squires. *Arkiv för Fysik*, **25**, 3, (1962).
- [27] Y. Fujii, N. A. Lurie, R. Pynn, and G. Shirane. *Phys. Rev. B*, **10**, 8 (1974).

-
- [28] J. Skalyo, Jr., V. J. Minkiewicz, G. Shirane, and W. B. Daniels. *Phys. Rev. B*, **6**, 12, (1972).
- [29] J. Skalyo, Jr., Y. Endoh, and G. Shirane. *Phys. Rev. B*, **9**, 4, (1974).
- [30] N. A. Lurie, G. Shirane, and J. Skalyo Jr. *Phys. Rev. B*, **9**, 12, (1974).
- [31] P. Korpiun and E. Lüscher. *Rare gas solids, Vol. II. Edited by M. L. Klein and J. A. Venables*. Academic Press Inc., New York, 1976.
- [32] O. G. Peterson, D. N. Batchelder, and R. O. Simmons. *Phys. Rev.*, **150**, 2 (1966).
- [33] D. L. Losee and R. O. Simmons. *Phys. Rev.*, **172**, 3 (1968).
- [34] J. U. Trefny and B. Serin. *J. Low Temp. Phys.*, **1**, 3, (1969).
- [35] R. A. Johnson. *Phys. Rev. B*, **6**, 6, (1972).
- [36] R. A. Johnson. *Phys. Rev. B*, **37**, 8, (1988).
- [37] Y. P. Varshni and R. C. Shukla. *J. Chem. Phys.*, **43**, 11, (1965).
- [38] Ramesh. C. Shukla and Herman Hübschle. *Can. J. Phys*, **70**, 31 (1992).

